2017

Atomic-scale simulation of physical and chemical processes during space weathering and planet formation

Abrar Quadery
University of Central Florida

ATOMIC-SCALE SIMULATION OF PHYSICAL AND CHEMICAL PROCESSES DURING SPACE WEATHERING AND PLANET FORMATION

by

ABRAR HOSSAIN QUADERY
B.Sc. (Honours) Physics, University of Delhi, 1995
M.Sc. Physics, University of Delhi, 1997

A dissertation submitted in partial fulfilment of the requirements
for the degree of Doctor of Philosophy
in the Department of Physics
in the College of Sciences
at the University of Central Florida
Orlando, FL

Fall Term
2017

Major Professor: Patrick K. Schelling

ABSTRACT

We investigate the mechanisms of space weathering and dust grain collisions, two topics of interests from planetary sciences, using atomic-scale simulations. Space weathering is the change in chemical and physical properties of minerals exposed to solar radiation and micrometeorite bombardment on surfaces of airless planetary bodies like the Moon and asteroids. An understanding of the connection between the surface evolution of the minerals and the underlying thermodynamic and kinetic factors is still missing. We address this issue and determine the time evolution of Frenkel defects in the silicate minerals olivine ($(Mg,Fe)_2SiO_4$) and orthopyroxene ($(Mg,Fe)SiO_3$) using molecular dynamics with a pair potential. Defect diffusion and clustering are observed in both the minerals. Cation diffusion occurs more readily in olivine than in orthopyroxene and leads to faster annealing in the former. In orthopyroxene, diffusion of anion defects, especially oxygen interstitials, occurs more rapidly and also exhibits anisotropy, which hinders the annealing process. This difference in defect evolution may explain the experimental observation that surface modifications due to irradiation is more pronounced in orthopyroxene than in olivine. Dust grain collision is the dominant process in the initial stage of planet formation, however, the mechanisms by which dust grains grow to larger aggregates and eventually to kilometer sized planetesimal is still not understood. We explore the role of surface chemistry in energy dissipation and grain adhesion during collision of amorphous silica (SiO_2) nanograins using molecular dynamics with a reactive potential, namely ReaxFF. We found nonhydroxylated amorphous silica nanoparticles stick with higher probability than their hydroxylated counterpart. This difference is attributed to the preponderance of unsatisfied dangling bonds on the dry silicate surface which facilitate bond formation during collision, and thereby provide a mechanism for energy dissipation. The speed below which sticking occurs in the dry nanograins is much higher than that found in Earth-based experiments, which suggests any experimental study of dust grain collision should take into account of the chemical environment. We probe into the nanograin collisions further and carry out atomistic simulatons of

collisions of molten silica nanograins. We observed in the molten state, amorphous silica is more sticky than it is in the solid phase. This happens due to increased viscoelastic energy dissipation. The result may explain how rocky planets originated from the inner rings of the protoplanetay disks where temperatures were as high as $\sim$ 2000 K. In order to increase the range of materials that could be simulated with ReaxFF potential, and also to examine the different oxidation states of iron associated with nanophase iron formation during space weathering, we made attempt to develop ReaxFF potential for fayalite (Fe_2SiO_4). We found out fundamental limitations of ReaxFF model to describe three-component minerals. However, during the fitting process we developed a model for iron silicide (FeSi), and made attempt to improve the silica model to obtain better elastic properties. We report here the fitting processes and the observed limitations of ReaxFF model.

To

Mom Rehana Begum

Dad Tozammel Hossain

Wife Rumana Zahir

ACKNOWLEDGMENTS

The pursuit of PhD had been a long journey for me, and I owe to a great many people for their undiminished support, without which I could not have completed the journey. The first and the foremost, I am proud of my advisor Dr. Patrick K. Schelling, apart from being a fine scientist, he is a compassionate human being. With utmost patience, he taught me the art of molecular dynamics, among other things. I am grateful to my committee members Prof. Daniel T. Britt, Prof. Robert E. Peale, Dr. Abdelkader Kara, and Prof. Yongho Sohn for their encouragement and guidance.

I feel a great sense of owe to the people of UCF whose support is vital for our working. I would like to express my thanks to Elizabeth, Esperanza, Felix, Monica and Jessica at Physics office, Angelina and Sandy at AMPAC, Dr. Paul Wiegand at Stokes ARCC, Jennifer, Wendy and Nathalia at College of Graduate Studies.

On a personal level, I am indebted to Prof. Saiful Khondaker who helped me join the PhD program at UCF. Dr. Elena Flitsiyan in physics department has always been supportive. I am grateful to my friend Dr. Bhavtosh Bansal at IISER Kolkata, my uncle Mahmud Osmani and aunt Hamida Osmani.

I always felt a deep sense of gratitude to the numerous people who contributed or are contributing to the world in the spirit of open source: Knuth's LaTeX, gnuplot, VMD to name a few. In particular, I would like to thank Torbjörn Björkman for his wonderful tool *cif2cell*, which has saved me many hours.

Customary it may be, I put their names last, but they know I would not have existed without them: my wife Rumana Zahir, and sons Zuhair Ishraque and Zaeem Israr. The journey towards PhD was not a lonely one for me, rather in every step I was supported and encouraged by my beautiful family. I love you all.

TABLE OF CONTENTS

LIST OF FIGURES

LIST OF TABLES

CHAPTER 1: INTRODUCTION

This thesis presents the results from the atomic-scale simulations of radiation damage in olivine ($(Mg,Fe)_2SiO_4$) and orthopyroxene ($(Mg,Fe)SiO_3$), and collisions of nanometer-sized amorphous silica (SiO_2) grains under different physical and chemical conditions. Radiation damage of minerals take place during space weathering of surfaces of airless planetary bodies like the Moon or Mars [1], and dust grain collision is the cardinal process in planet formation [2]. Both are topics of interests from planetary sciences, and in this thesis we investigate these phenomena from the perspective of materials science. Specifically, we use molecular dynamics to first investigate the thermodynamic evolution of Frenkel defects resulting from radiation damage in the silicates olivine and orthopyroxene. Later, we move on to explore how physical and chemical states of silica naongrains affect the outcome of their collisions, i.e., sticking, bouncing or fragmentation of the nanograins. The study was motivated by the fact that even after decades of research, some fundamental questions pertaining to space weathering and planet formation remain answered. The study has been interdisciplinary in nature, and sheds some new lights on some long standing planetary science questions which are elaborated below by making use of computational tools from materials science. To be able to carry out molecular dynamics, in the study of defects in silicates, we had to develop our own force field, i.e., empirical potential that defined the interactions among the elemental species present in the minerals. We studied collisions of silica nanograins using a reactive potential from literature [3], however, we made attempt to develop a new model to describe the silica elastic properties better. In this thesis, along with the observations from the atomistic simulations, we also report our work on potential development.

Space weathering causes surface modifications of minerals [1], and in our simulation we investigated how differences in the mineral composition and structure affect the weathering process. In the simulations of nanograin collisions, we first focused on the role of surface chemistry, which is the chemical interaction of atoms and ions at interfaces, in energy dissipation and grain

adhesion during collisions. As a test case of surface chemistry, we found out how surface hydroxylation can influence the collisional outcome. In the second part of our work with silica nanograin collisions, we probed into the relation of thermodynamic state to collision outcome, and carried out simulations at different temperatures where the silica nanograins were either solid, partially melted, or completely melted.

An overarching theme of the above sudies was that surface chemistry should be an important considerations in any study of the processes taking place in space environment. The events that we studied here involved either surface processing of minerals or dust grains, or surface interactions of dust grains. Mineral surfaces on airless planetary bodies evolve due to space weathering, dust grains in a protoplanetary disk may be dry or hydroxylated, or remain in a molten state, which could have a bearing on the outcome of dust grain collisions.

In computational study of dust grain collision, often coarse-grained continuum models are used where each grain is treated as an entity with material properties like surface energy and elasticity determined from experiments [4–6]. However, such an approach is fraught with limitations, as the coarse-grain models do not have have mechanism in them to incorporate surface chemistry or thermodynamic factors. Experiments and computational studies based on continuum models have so far failed to provide an complete understanding of the mechanisms of planet formation, and it appears new ideas are required for making progress [7]. In his pioneering paper [8], Safronov commented that the problem of origin of earth and planet 'is one that can be solved only by recourse to many disciplines'. We thus need to make the first steps and seek an atomic-level understanding of adhesion in dust grain collisions. Use of atomic-scale simulations to elucidate the mechanisms of phenomena in planetary sciences is a novel approach, and can lead to insights otherwise not possible with existing theories.

In the following sections, we provide an overview of space weathering and dust grain collisions and explain in further details the relevant science questions that motivated this study.

1.1 Space Weathering

The surfaces of airless planetary bodies, including the Moon, asteroids, and Mercury, are exposed to solar wind, micrometeorites, cosmic rays, and solar radiation (Fig. 1.1). This results in pulverization, melting, mixing, thermal dissociation, sputtering, and ion implantation at the surface, leading to changes in the physical, chemical, optical and mineralogical properties. These surface modification processes and their resulting effects are collectively termed as space weathering. Fundamentally, space weathering can be viewed as the evolution of material properties and chemistry at the surface in a non-equilibrium environment.

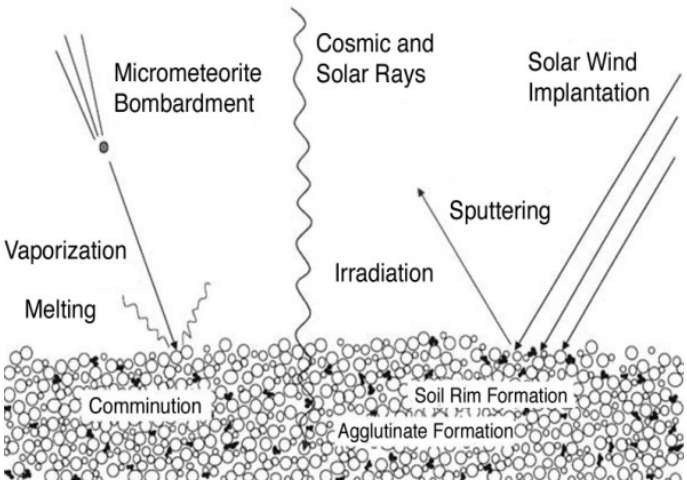

Figure 1.1: Various components of space weathering

Space weathering was first recognized to have taken place on the surface of the moon. From the observation that crater rays appeared brighter than their surrounding materials, in the early sixties Gold [9] and others conjectured that some kind of darkening process was taking place on the surface of the moon. Analysis of near infrared-visible (NIR-vis) reflectance spectra of samples collected during the Apollo lunar missions later revealed that space weathered materials have lower albedo which makes them appear darker (*darkening*), have weaker spectral features (*shallower absorption bands*), and have a characteristic reflectance spectra which increases towards longer

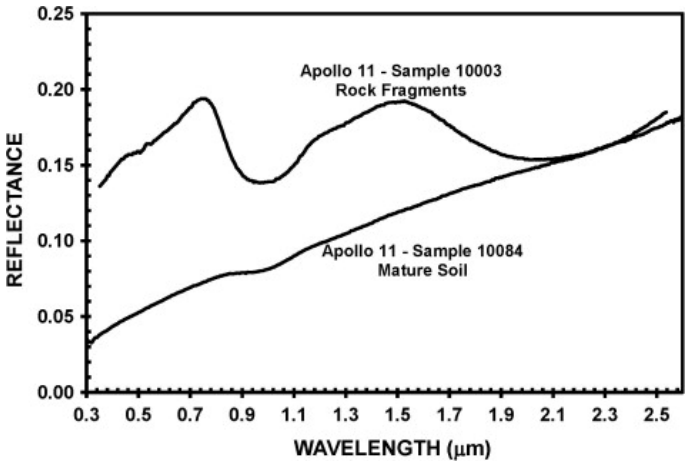

Figure 1.2: Reflectivity spectra of bedrock fragments and mature soil on lunar surface. The mature soil is the result of space weathering of bedrock fragments, and consequently possesses lower albedo, shallower absorption band and steeper overall curve (after Adams and Jones [10]).

wavelengths (*reddening*)(Fig. 1.2)[10].

Findings from the space weathering of the moon have the immediate implication that space weathering masks the true mineralogy and compositional attributes of a body from its remotely-sensed data as remote sensing samples the space weathered surface. This has a bearing on the interpretation of the spectral information of other airless bodies, e.g., Mercury and the asteroids. A long existing scientific conundrum in this regard is the association between the ordinary chondrite meteorites and S-type (siliceous) asteroids. Spectra from these two sources are different, but a 'variety of circumstantial evidence' suggest that spectra of ordinary chondrites can assume the overall spectral shape and slope of S-type asteroids upon space weathering [11].

Much is still unknown about the exact mechanisms, rates and compositional dependence of various processes of space weathering. For example, in case of the moon, only after decades of research and debate, it is now generally accepted that the threefold optical effects of space weathering described above are caused mainly by the submicroscopic Fe particles (SMFe), also called nanophase iron particles ($npFe^0$), which form on the patina and rim of lunar regolith (Fig. 1.3) dur-

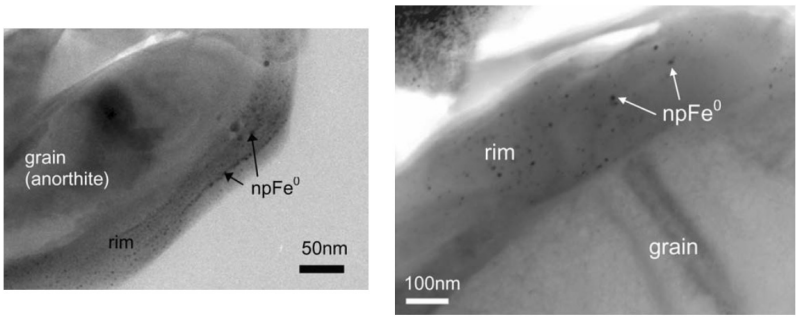

Figure 1.3: TEM images of nanophase iron-bearing rims on lunar soil grains (Credit: Sarah Noble et al., Meteoritics & Planetary Sci., 40(18):397–408, 2005)

ing solar-wind sputtering and micrometeorite impact vaporization. The generally accepted view is that the $npFe^0$ primarily is produced as reduced impact vapors condense on grain surfaces [1, 12–14]. However, recent analysis of samples returned from asteroid Itokawa shows that $npFe^0$ could be produced in other ways. In Itokawa samples, beneath a layer of material deposited from vaporized material, there exists a layer which shows evidence of partial amorphization and reduction from radiation damage [15, 16]. Nanophase iron has been observed in both layers, which suggests that $npFe^0$ can be produced by radiation damage along with condesation of reduced impact vapor, and we need to understand the mechanisms by which radiation damage can lead to amorphization and $npFe^0$ inclusions. Also, it is not clear under what conditions solar wind irradiation might compete with impact vapor deposition as a mechanism to generate $npFe^0$.

Experimental simulations of space weathering through pulsed laser irradition has shown that space weathering rate of a mineral depends on its composition. For example, it has been found that spectral alterations take place more readily in olivine than in orthopyroxene [17, 18]. Again, an understanding is lacking, and in this study we made attempt to determine the underlying reasons. A systematic study of defects evolution in different minerals might help establish a correspondence between the spectra of space-weathered surfaces to their true composition. With this motivation, in the first part of our work, we carried out atomic-scale simulations of time evolution of point

defects in the silicate minerals olivine and orthopyroxene.

To carry out the molecular dynamics study, we first developed a pair-potential for olivine and orthopyroxene. However, a pair-potential is unable to model chemical bond breaking and formation, and consequently cannot simulate the reduction process that leads to nanophase iron during space weathering. As a result, we made attempt to develop a reaxFF potential for fayalite, the iron-rich member of olivine.

1.2 Dust Grain Collision and Planet Formation

Silicate dust grain is ubiquitous in the universe. It permeates interstellar and interplanetary medium and coexists with gases in the protoplanetary disk that surrounds a newborn star and planetary rings. Dust collision, also called dust coagulation, takes place in these environments. Collision of dust grains is central to planet formation – it is the process through which particles grow all the way to kilometer-sized planetesimals, when gravitational force takes over. Dust grains collide to form aggregates, and aggregates collide to form planetesimals [19]. Study of dust grain collision has application in other fields as well, e.g., in tribology which is the study of friction, aerosol industries, surface deformation, materials elastic and plastic response characteristics, and atomic scale manipulation of surface structures.

In this thesis, we study silica nanograin collision from the context of planet formation. The first attempt to put planet formation in a scientific footing, called the nebular hypothesis, was pioneered and advanced about three centuries ago by Emanuel Swedenborg (1734), Immanuel Kant (1755) and Pierre-Simon Laplace (1796). Safronov [8] put forward the idea of planetesimal. According to these theories, the formation of planetary systems is a natural outcome of star formation. Stars form from the gravitational collapse of massive and dense clouds of molecular hydrogen and sub-micron sized dust, termed as giant molecular clouds (GMC), in the interstellar medium. To conserve angular momentum, the remnant gas and dust form a protoplanetary disk that surrounds

the newborn star [20]. From the protoplanetary disk, planets form in three key stages [21]. In the first stage, micrometer-sized dust grain near the midplane of the protoplanetary disk accrete one another via collisions, eventually forming 1-10 km sized planetesimals. In the second stage, the larger of the planetesimals attract and scoop more materials due to gravity and orbits with low eccentricity and inclinations and grow to $\sim$ 3000 km diameter planetary embryos. In the third stage, collisions of planetary embryos result in formation of planets on widely separated orbits.

Starting from dust grain, the formation of planets spans a spatial range of the order 10^{13}, and many of the steps are not completely understood. Here we focus on the first stage where dust grain collisions dominate and form planetesimals. By simulating dust grain collisions under different chemical and physical conditions, we seek an atomic-scale understanding of dust grain collisions.

Experiments as well as numerical modeling have been carried out to understand dust grain collision. Numerical modeling of collision of dust grains have been done using coarse-grain models. Chokshi et al. [4] considered the collision of two smooth, elastic, spherical grains and derived critical velocities above which dust grain collision will lead to bouncing instead of sticking. Dominik and Tielens [5] simulated collisions between two grain aggregates each consisting of tens of grains (monomers) in two-dimensional space and considered the effect of pull-off, rolling, sliding and twisting. These simulations were based on grain-grain contact physics where the adhesive interaction was described by Johnson-Kendall-Robert (JKR) theory [22]. In this theory, the interaction force is determined by elastic properties of materials, e.g., Poisson's ratio and Young's modulus, surface energy and the adhesion is caused by the molecular van der Waals forces. N-body simulations of collisions of large three-dimensional aggregates were carried out by a group of researcher who examined the dependence of collisional outcome on the collision velocity [23, 24].

The above studies were limited by several factors. The sticking velocity determined by Chokshi [4] came out to be smaller by a factor of 10 from the experiments done by Poppe et al. [25] who determined it to be $\sim$100 cm s^{-1} for micron-sized quartz grains. The simulation

by Dominik was carried out in a two-dimensional space. The N-body simulations cannot predict sticking for collisions happening at a speed beyond 10 m s^{-1}. The most important limitation of all was that the energy dissipation took place only via elastic waves. However, recent simulations have incorporated dissipation via viscoelasticity as well as plastic deformation [26]. The limitation that for spherical silicates a typical growth limit occurs at around mm in size for velocities of the order of cm s^{-1} as observed in experiments and numerical simulations has been termed as 'bouncing barrier' [27].

In this study, we focus on the dust aggregate formation process. In our computational approach, we employ a realistic interaction described by ReaxFF potential that can depend on charges as well. We examine the effect of surface chemistry in the outcome of dust colllision by studying collision between hydroxylated and nonhydroxylated nanoparticles. Later, we simulate collisions between molten silica nanograins and study the effect of viscous dissipation.

We emphasize that given the huge parameter space that one encounter in the study of planet formation, our approach can help. For example, since we are using a more realistic potential, we can take up different materials, like olivine, pyroxene, ice, etc. Also, with the availability of increasing computational power, atomic-scale simulations could be extended to the regime where grains form planetesimal.

1.3 Organization of the thesis

The thesis is structured in the following manner. In the current chapter (Ch. 1), we present an overview and motivations of our research goals. In Chapter 2, we explain the compuational techniques used in this thesis and also describe the development of a pair-potential. In Chapter 3, we present the molecular dynamics study of time evolution of Frenkel defects in olivine and orthopyroxene. In Chapter 4, we discuss the role of surface chemistry in dust collision as revealed by the molecular dynamics study of silica nanograin collisions using a many-body reactive poten-

tial, namely ReaxFF. Chapter 5 contains the molecular dynamics study of molten silica nanograin collisions. Finally, in Chapter 6 we describe the ReaxFF potential fitting process.

CHAPTER 2: MATERIAL SYSTEMS AND METHODOLOGY

In this work, we first studied time evolution of Frenkel defects in olivine and orthopyroxene using molecular dynamics (MD). We modified a pair potential developed by Pedone et al. [28] to describe better the structural and elastic properties of the mineral systems and used the modified potential in MD simulations. In other computational work, we studied collisions of amorphous silica (SiO_2) nanoparticles in different chemical and thermodynamic conditions using MD. For MD simulations of collisions, we used a reactive empirical potential, called 'ReaxFF' potential, in order to be able to investigate role of surface chemistry. In particular, we used the ReaxFF potential for silica developed by Kulkarni et al. [3]. In an effort to extend the range of materials that could be simulated using reactive potentials, and also to study chemical reduction that lead to nanophase iron formation, we then put our efforts in developing a ReaxFF potential for fayalite (Fe_2SiO_4). Also, we made attempts to obtain a ReaxFF silica model that would describe silica elastic properties better.

In this chapter, we familiarize the readers first with the different mineral systems we investigated here. Then we explain various concepts and ideas associated with the computing machinery that we made use of here. Finally, we describe how we developed the new pair potential for olivine and orthopyroxene. We leave the details of ReaxFF potential development for silica and fayalite for Chapter 6.

2.1 Silica (SiO_2 and silicates

Silica is another name for the chemical compound SiO_2, or silicon dioxide. It exists in many crystalline forms, collectively called silica polymorphs, and also in amorphous form. We will describe the crystalline polymorphs in Chapter 6. Silica can combine with metals and their oxides and form silicates.

In all forms of silica, whether crystalline or amorphous, the basic building block is silica tetrahedra SiO_4. This is a tetrahedral arrangement where one silicon atom is covalently bonded to four oxygen atoms (Fig. 2.1). The unit is overall neutral, however, it has a residual charge of four negative charges. This residual charge allows the tetrahedron to form compounds with metallic cations. The Si and O are bonded by very strong covalent bonds with bond energy of about 4.69 eV that provides the characteristic thermal stability and chemical resistance of silicates. The Si–O bond length is $\sim$ 1.64 Å and the O–O bond length is $\sim$ 2.65 Å. The unit is very stable and the geometry virtually remains unchanged with Si being fourfold coordinated in any environment except in extreme conditions.

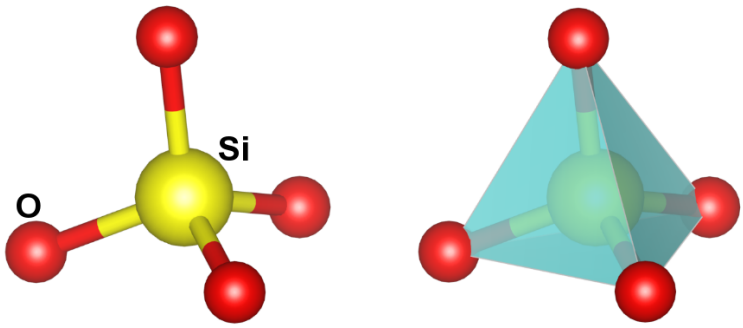

Figure 2.1: Silica tetrahedron, which almost has the structure of a uniform tetrahedron.

In a network of SiO_4 tetrahedra, an oxygen atom can be bonded to two silicon ions, so that two tetrahedra are joined at a corner by a bridging oxygen atom. SiO_4 tetrahedra can arrange in numerous ways. In crystalline silica (SiO_2), e.g., in quartz, all oxygen atoms are bridging (Fig. 2.2). In amorphous silica, the orientation is random, and some oxygen atoms will be bonded to only one silicon ion.

General definition of silicates are that they are compounds containing SiO_4^{4-} anions and one or more metallic cation. Fore example, Mg_2SiO_4, Fe_2SiO_4, $ZrSiO_4$ etc. Silicates are classified into nesosilicate (isolated tetrahedra), phyllosilicates (layered silicates) on the basis of degree of

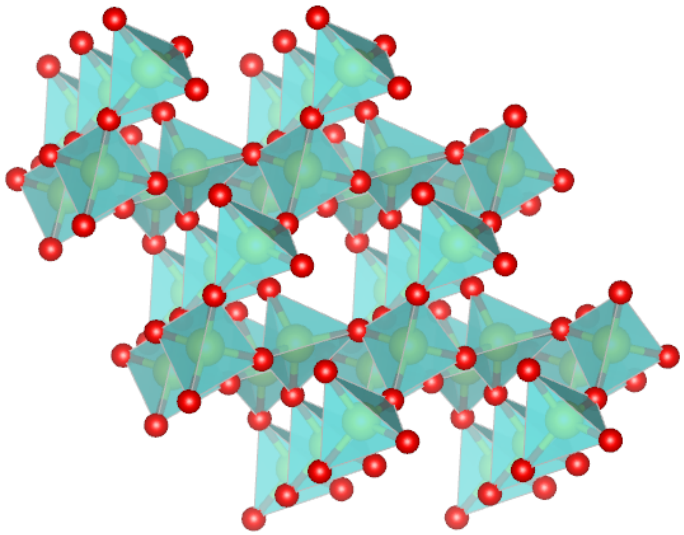

Figure 2.2: Structure of quartz, a crystalline polymorph of silica.

polymerization of the SiO_4^{4-} tetrahedra.

2.2 Olivine and orthopyroxene

In this work, we undertake the study of radiation damage in olivine and orthopyroxene and make attempt to explain the observed differences in their space weathering rate [17, 18]. The choice of these minerals also stems from the fact that they are important mineral constituents of planetary surface and S-type (siliceous) asteroids and are present in a wide range of environments including protoplanetary disks and interstellar dust [29].

Olivines are orthorhombic nesosilicate with lattice parameters a $\sim$ 4.78 Å, b $\sim$ 10.25 Å and c $\sim$ 6.3 Å, where isolated SiO_4 tetrahedra bound to each other through ionic bonds with cations [30, 31]. The metal cations are surrounded by six oxygens in an octahedral arrangement, i.e., octahedrally coordinated. The cations occupy half of the octahedral sites, the silicon ions occupy one-eighth of the tetrahedral sites, and the oxygen ions form essentially a hexagonal, closest-packed network (Fig. 2.3). The mineral composition generally includes both Mg and Fe, along with other

elements at lower concentrations, resulting in many different compositions. The composition of olivine can vary continuously between forsterite Mg_2SiO_4 and fayalite Fe_2SiO_4. The reason that Mg and Fe can replace each other is that Mg^{2+} and Fe^{2+} have similar size, having a radius of 0.72 Å and 0.77 Å respectively. The conventional unit cell of olivine contains 28 ions.

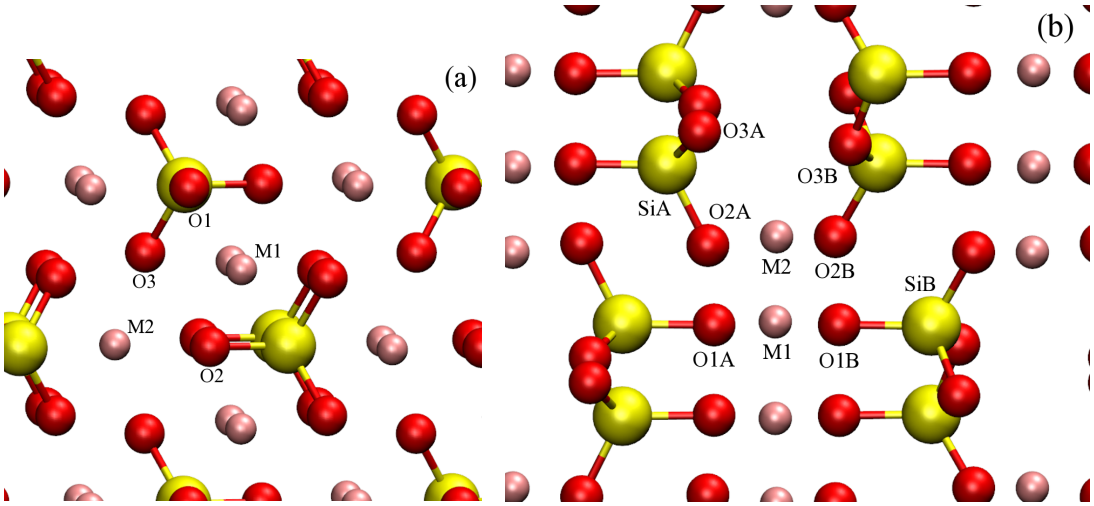

Figure 2.3: Crystal structure of (a) olivine and (b) orthopyroxene. Here, grey, yellow and red spheres represent Mg/Fe sites, Si sites, and O sites respectively. In olivine, the SiO_4 tetrahedra are isolated, whereas in pyroxene each tetrahedron shares two of its oxygen with two neighboring tetrahedra to form a silicate chain along c axis of the crystal.

There are two symmetrically nonequivalent distorted octahedral sites, M1 and M2 (Fig. 2.4). M1 site is smaller, more distorted in angles, and less distorted in distances; M2 site is larger, less distorted in angles, and more distorted in distances. The average M1-O bond lengths are shorter (2.16 Å) than the average M2-O bonds (2.19 Å) [31]. Like the cations, there are also three distinct sites for the oxygen ions (labeled O1, O2 and O3 in Fig. 2.3(a)). M1 site is coordinated with two oxygen ions from each of the three O-sites, whereas M2 site is coordinated with four oxygen ions from O3 sites, and one oxygen ion each from O1 and O2 sites. Orthopyroxenes are a class of pyroxene that has orthorhombic structure, and has lattice parameters a $\sim$ 18.23 Å, b $\sim$ 8.84 Å, and c $\sim$ 5.19 Å [32]. Unlike olivine, they are inosilicate, where the SiO_4 tetrahedra form

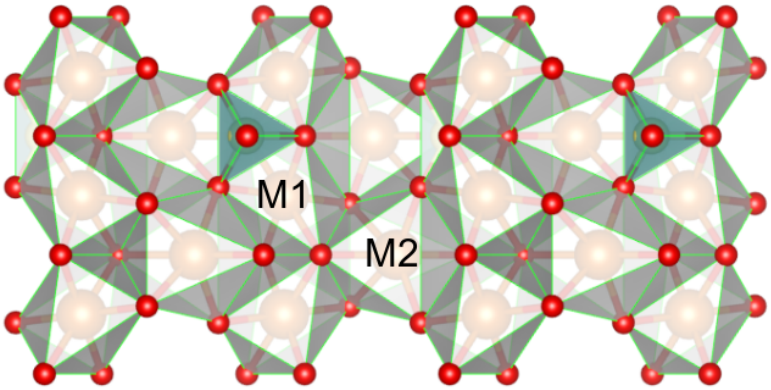

Figure 2.4: The cations in olivine are octahedrally coordinated, i.e., coordinated by six oxygens. M2 octahedron is larger and more distorted than M1.

a continuous chain, with a repeat distance of about 5.3 Å, parallel to the c crystallographic axis by sharing two of the four corners with neighboring SiO_4 tetrahedra (henceforth termed 'corner sharing of oxygen'). This sharing leads to the formation of a chain with composition $(SiO_3)_n$. The conventional unit cell of orthopyroxene contains 80 ions.

In Fig. 2.3(b), the crystal structure of orthopyroxene is shown. In the orthopyroxene structure, as with the olivine, there are two distinct Mg/Fe sites labeled M1 and M2 [32]. In addition, the orthopyroxene structure has two distinct Si sites SiA and SiB. There are six distinct oxygen sites. In each SiA tetrahedra, two of the neighbors are O3A sites, one is an O1A site, and another is an O2A site. The O3A sites connect neighboring SiA tetrahedra along the c-direction. The other three distinct oxygen sites are associated with the tetrahedra formed with the SiB sites. In each SiB tetrahedra, two of the neighbors are O3B sites, one is an O1B site, and one is an O2B site. The O3B sites are neighbors with two SiB sites, and hence connect neighboring tetrahedra along the c-direction. The octahedron associated with the M2 site includes one of each type of oxygen site. By contrast, the M1 sites have as neighbors two O1A and O1B sites, one O2A site, and one O2B site. The six distinct oxygen sites each have different cation coordination. The O3A and O3B sites

have two Si sites and one M2 site as neighbors. The O1A, O2A, O1B, and O2B sites each have just one Si site as a neighbor. However, the O1A and O1B sites each have two M1 sites and one M2 site as neighbors, while the O2A and O2B sites have one M1 site and one M2 site as neighbors.

2.3 Classical molecular dynamics

Classical molecular dynamics is a computer simulation method where one numerically integrate Newton's equation of motion for an ensemble of atoms using a empirical potential that defines the atom interactions. For a system with N particles with potential energy U, the equation of motions are given by the following:

$$m_i \frac{d^2 \mathbf{r}_i}{dt^2} = -\nabla_{\mathbf{r}_i} U(\mathbf{r_i}, \ldots, \mathbf{r_N}), i = 1, ..., N. \tag{2.1}$$

In molecular dynamics, one can approximate the real dynamics of every atom in the system, and thus gain insights into processes taking place at the atomic and molecular level by solving numerically the 3N equations of motion [33]. The idea is simple, however, there are several considerations that need to be addressed, e.g., boundary conditions, choice of integrators, thermostat, method of evaluating Coulomb interaction etc. There exist elaborate schemes which enable one to calculate different equilibrium and nonequilibrium properties, e.g., T or P, of canonical (NVT), microcanonical (NVE) and other ensembles using the positions and velocity obtained from the solutions. For instance, the instantaneous temperature of a system is given by, $T_{ins} = \frac{2}{3}\frac{E_{kin}}{k_B}$, with $E_{kin} = \frac{1}{2}\sum_i m_i [v_i(t)]^2$, and the ensemble average is given by, $\langle T \rangle = \frac{1}{n}\sum_n T_{inst}(n)$, where the sum extends over all time steps of the simulation, n.

The validity of molecular dynamics in terms of thermodynamic averaging relies on the ergodic hypothesis, which states that the average of a process parameter over time and the average over the statistical ensemble are the same. To achieve this, ensemble and integrator are grouped together to create a special dynamics whose trajectory over time forms a cloud in phase space

that has the desired distribution density [34, 35]. In short, for equilibrium MD simulation, the time average of a thermodynamic quantity can be used to approximately determine the ensemble average.

2.4 Empirical potential

The critical component in classical MD simulation is the interatomic potential. Interatomic potential is a mathematical function which gives the potential energy of a system of atoms with given spatial coordinates. The potential is empirical in the sense that it does not describe the true quantum mechanical interaction of atoms and rather reproduce empirical data, including materials properties, or even quantum mechanical calculations. Empirical potentials are developed by fitting to results from experimental observations and/or quantum mechanical (density functional theory) calculations. There are different classes of empirical potentials geared for different physical problems. They can be broadly grouped as pair-potentials and many-body potentials. Many-body potentials come in many different forms, e.g., bond-order potential (e.g., Tersoff potential), reactive potential (e.g., ReaxFF, COMB), embedded atom model (EAM) potential etc. In this work, we made use of empirical potentials of both kind.

As its name suggests, a pair-potential defines the interaction bwtween two atoms, which could be from the same or different elemental species. In this work, we study the defects evolution in two ionic materials, namely olivine and orthopyroxene. For oxide materials, long-range Coulomb interactions are important, and as a result interactions are typically described using a pair-potential of the following form:

$$u_{ij}(r_{ij}) = \frac{q_i q_j}{r_{ij}} + D_{ij}\left[e^{-2\alpha_{ij}(r_{ij}-r_0)} - 2e^{-\alpha_{ij}(r_{ij}-r_0)}\right] + \frac{C_{ij}}{r_{ij}^{12}}\,, \tag{2.2}$$

where u_{ij} is the pairwise potential energy of two atoms labeled by i and j separated by a distance r_{ij}. The Coulombic charges q_i and q_j are typically constant. Along with the charges, the param-

eters D_{ij}, C_{ij} and α_{ij} are fitted so that the potential can reproduce equilibrium properties of the perfect crystal, including lattice parameters, elastic constants, and lattice thermal expansion, and also results from first principles calculations. In this thesis, we first reparameterize an existing pair potential and use it for studying evolution of point defects in the silicates olivine and orthopyroxene.

Many-body potential include energy terms that depend on three or more nearby atom positions. Thus in addition pairwise interaction energy, it can describe how the potential energy changes with bond angle and torsion. This feature is essential for modeling covalent bonds among others. ReaxFF is a many-body potential formalism developed by van Duin et al. in 2001 [36] and combines several features from other many-body potentials. First, it incorporates the idea of 'bond order', the idea that bond strength between two ions will depend on the environment. For example, the pair potential will give the same bond strength for the four Si-O bonds in a SiO_4 tetrahedra as it will give for a isolated Si-O bond. But in reality that is not the case, for example in covalent materials. If an oxygen atom is brought near a Si-O bond, the bond strength will decrease. Bond-order potential can describe this behavior. The bond-order term is still a function of distance beteween two atoms, however, it has other directional dependence. The feature which distinguishes ReaxFF from other bond-order potentials is atomic charges are not fixed in this model. The charges are dynamically updated using electron equilibration method (EEM) [37, 38]. ReaxFF potential also include nonbonding van der Waals and Coulomb interactions, as well as local perturbation terms like angle, torsion etc. whose strength also depend on bond order. The upshot of all these features is that it can describe different chemical environment including covalent, metallic, ionic materials and their interfaces simultaneously, which is not possible with other bond-order or pair potential. A review of ReaxFF and similar methods can be found in [39].

In this work, we made attempt to understand the surface chemistry dust grain collisions, and ReaxFF was an appropriate choice of potential for that. Also, we wanted to explain the different oxidation states of irons associated with nanophase iron formation in minerals on planetary

surfaces due to space weathering which is possible only through a potential like ReaxFF.

2.5 Density Functional Theory

Empirical potentials cannot explain electronic properties, a quantum mechanical treatment is required for that, which means instead of Newton's equation one has to solve Schrödinger equation. For a collection of N electrons moving under the influence of an external potential $V_{ext}(\mathbf{r})$ and mutual Coulomb repulsion, the Hamiltonian H is given by the following:

$$H = \sum_{i=1}^{N} \left[-\frac{\hbar^2 \nabla_i^2}{2m} + V_{ext}(\mathbf{r}_i) \right] + \sum_{i>j} \frac{e^2}{|\mathbf{r}_i - \mathbf{r}_j|}. \tag{2.3}$$

The Schrödinger equation is given by:

$$H \left|\Psi\right\rangle = \epsilon \left|\Psi\right\rangle \tag{2.4}$$

where $\left|\Psi\right\rangle \equiv \Psi(\mathbf{r}_1, \ldots, \mathbf{r}_N)$ is the many-body wavefunction.

Once $\left|\Psi\right\rangle$ is determined, the ground state energy E_0 of the system can be calculated by minimizing the energy functional $E[\Psi] = \dfrac{\langle \Psi H \Psi \rangle}{\langle \Psi \Psi \rangle}$. Also, the electron density $n(\mathbf{r})$ can be determined by integrating $\left|\Psi\right\rangle$ over spin coordinates of all electrons and over all but one of spatial variables. By its very definition, $n(\mathbf{r})$ is a function of only 3 spatial coordinates, and gives the probability of finding any of the N electrons within the volume elemment d^3r.

$$n(\mathbf{r}) = N \int d^3r_2 \ldots \int d^3r_N \left|\Psi(\mathbf{r}, \mathbf{r_2}, \ldots, \mathbf{r_N})\right|^2 \tag{2.5}$$

Conceptually the above recipe to determine wavefunction from a given Hamiltonian is simple, however, a direct evaluation is practically impossible because of the extraordinary number of calculations it requires. Historically there have been attempts to bypass this obstacle, most

notably the Hartree-Fock method, however, Hohenberg and Kohn came up with the most profound and simplifying ideas [40]. They observed, from Eqs. 2.4 and 2.3, that for a particular system, $|\Psi\rangle$ could vary only if V_{ext} were varied, which implied that $n(\mathbf{r})$ was a functional of V_{ext}. Hohenberg and Kohn showed, by *reductio ad absurdum*, that the converse was true, i.e., V_{ext} was a unique functional of $n(\mathbf{r})$ to within an additive constant. This in turn implied the ground state of the system was a unique functional of $n(\mathbf{r})$, and the energy E = E[$n(\mathbf{r})$] would assume its minimum value for the correct $n(\mathbf{r})$.

Kohn and Sham developed these ideas further, and derived the following equations [41]:

$$n(\mathbf{r}) = \sum_{i}^{N} \sum_{s} |\psi_i(\mathbf{r}, s)|^2 \tag{2.6}$$

$$-\frac{\hbar^2}{2m}\nabla^2\psi_i(\mathbf{r}, s) + v_{eff}(\mathbf{r})\psi_i(\mathbf{r}, s) = \epsilon_i\psi_i(\mathbf{r}, s) \tag{2.7}$$

$$v_{eff}(\mathbf{r}) = V_{ext}(\mathbf{r}) + e^2 \int \frac{n(\mathbf{r}')}{|\mathbf{r} - \mathbf{r}'|} d\mathbf{r}' + \frac{\delta E_{xc}[n]}{\delta n} \tag{2.8}$$

The transition from Eq. 2.5 to Eq.2.6 was a simplifying one – a system of N interacting electrons is now rendered to a system of N noninteracting electrons which generates the same electron density as the former. In Eqs. 2.6 - 2.8, v_{eff} is the effective potential acting at a given location, V_{ext} is the external Coulomb field produced by the nuclei and can include contributions from other external electromagnetic fields, and E_{xc} is exchange-correlation energy. E_{xc} is obtained through several schemes called local density approximation (LDA), generalized gradient approximation (GGA) etc. The equations are coupled, and have to be solved in a self-consistent, i.e., iterative way. One begins with an assumed $n(\mathbf{r})$, constructs v_{eff}, and find a new $n(\mathbf{r})$ from Eq. 2.7 and Eq. 2.6.

In this work, we used density functional theory as an ancillary tool for our work on ReaxFF potential development. In empirical potential development, target functions like system energy for different volumes are fitted by varying the fitting parameters. We calculated the target energies for Si-O dimer, Si-O-Si and O-Si-O trimers, crystal polymorphs of SiO_2 and other systems using DFT.

2.6 Pairwise potential development

2.6.1 Methodology

The empirical pair potentials (u_{ij}) used in this work has the form given by Eq. 2.2 which contains a Morse type potential (the second term), Coulombic interaction with fixed point charges (the first term), and a short-ranged Lennard-Jones type $1/r^{12}$ repulsive term (the third term). This form was used by Pedone et al. [28] who fitted the parameters to a range of binary oxides inlcuding MgO, FeO, SiO_2 at T = 300 K and P = 1 atm. The potential provided reliable description of more complex oxides not included in the fit including forsterite, fayalite, and enstatite. To enhance the description of the experimental properties of forsterite, fayalite, orthoenstatite, and ferrosilite, we further refined the parameters by fitting simultaneously to the observed lattice parameters, elastic constants, and crystal structure of the crystals. The fitting was done using the General Utility Lattice Program (GULP) code [42]. The electrostatic interactions were computed through the Ewald method [43, 44]. During the fit, the parameters C_{ij} for the repulsive interactions were not varied and were kept fixed at their original values from [28]. In the model, partial charges used for different ionic species were as follows: $Q_{\mathrm{Mg,Fe}} = +1.2$ e, $Q_{\mathrm{Si}} = +2.4$ e, and $Q_{\mathrm{O}} = -1.2$ e. The potential parameters obtained from the fit for different elemental pairs are shown in Table 2.1. The corresponding potential functions are plotted in Fig. 2.5.

Table 2.1: Parameters for the empirical pair potentials described by Eq. 2.2; parameters optimized for olivine and orthopyroxene.

Pair	D (eV)	a (Å^{-1})	r_0 (Å)	C (eV Å^{12})
Mg-O	0.123583	2.045583	2.424824	5.0
Fe-O	0.064948	1.888936	2.644110	2.0
Si-O	0.443427	1.758024	2.081625	1.0
O-O	0.042323	1.311417	3.762599	22.0

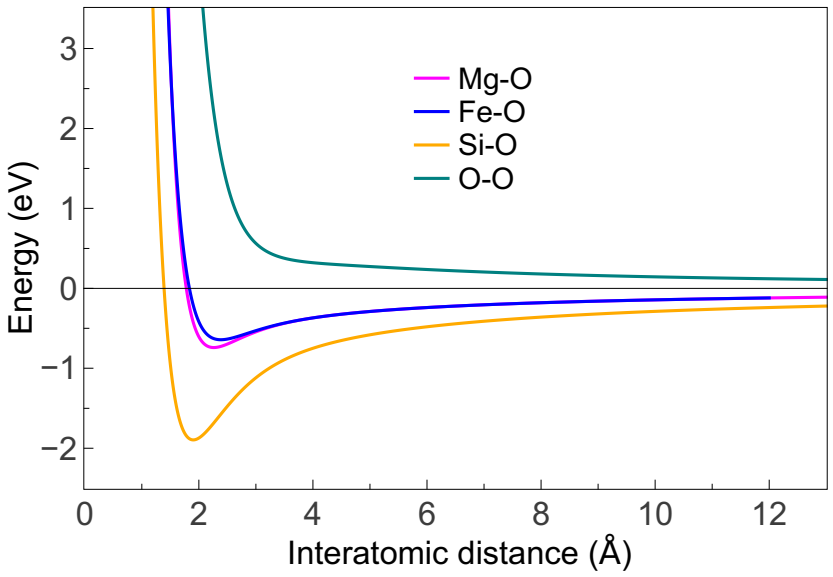

Figure 2.5: Pair potential for different pairs of elemental species in olivine and orthopyroxene. The plots indicate that Si–O interaction is the strongest.

2.6.2 Validation

Comparison of olivine and pyroxene properties including the lattice parameters, unit cell volume, and elastic properties computed from Pedone potential and the potential fit here at T = 0 K are given in Tables 2.2 - 2.5. We also tabulate, except in the case of ferrosilite, the target experimental values [45, 46] along with Pedone values reported in [28] for T = 300 K. As mentioned before, in contrast to the calculations reported here, the values from [28] were obtained by minimization of the free energy within the quasi-harmonic approximation at room temperature. It is important to note that the experimental properties tabulated here also were measured at room temperature. Therefore, the experimental values are best compared to calculations using free energy minimization. However, at T = 300 K, thermal expansion introduces a small effect.

In the case of forsterite (Table 2.2), the computed values for both the potential are in good agreement with experiment, however the potential fit obtained here produces better results for the

Table 2.2: Computed and experimental properties of ground state forsterite compared with experimental values. First column reported values from [28]. The values in the second column were computed here using the potential reported in [28]. The bulk modulus is computed using the Reuss approximation. Elastic constants and bulk modulus are given in units of GPa.

Property	Pedone (300 K) [28]	Pedone (T = 0 K)	This work	Experiment
a (Å)	4.8447	4.8454	4.7806	4.7530
b (Å)	10.1875	10.1891	10.1418	10.1900
c (Å)	6.0022	6.0032	5.9632	5.9780
Ω (Å^3)	296.2444	296.3792	289.1169	289.5329
C_{11}	298.2	298.0	323.6	328.0
C_{22}	174.6	174.5	195.2	200.0
C_{33}	216.0	216.1	243.3	235.0
C_{12}	69.4	69.5	72.9	69.0
C_{13}	74.1	74.2	77.2	69.0
C_{23}	74.4	74.4	85.6	73.0
C_{44}	38.7	38.9	45.9	66.7
C_{55}	58.5	58.5	68.1	81.3
C_{66}	68.2	68.2	76.1	80.9
B	119.9	119.9	132.6	129.5

overall cell volume Ω and the elastic constants C_{11}, C_{22}, and C_{33}. In the case of enstatite (Table 2.3), the modified potential again predicts better values of the cell volume Ω, and also of the elastic constants C_{22}, C_{33}, and the bulk modulus B. In the case of fayalite (Table 2.4), the modified potential does not demonstrate any significant improvement over the Pedone potential. In case of the ferrosilite (Table 2.5), the Pedone potential gives somewhat better results for the cell volume Ω and other elastic properties including C_{11}, but this trend is not uniform.

Though not included in the fit, we evaluate the dielectric constants of the minerals using the newly developed potential using GULP [42] and tabluate them along with the experimental values [47, 48] in Table 2.6. For forsterite and fayalite, all three diagonal components of the computed values, denoted by subscripts xx, yy and zz, are much lower than the experimental values, However, the relative strengths of xx, yy and zz components agreed with those from experiments.

Table 2.3: Computed and experimental properties of ground state orthoenstatite compared with experimental values. First column reported values from Pedone et al. [28]. The values in the second column were computed here using the potential reported in [28]. Elastic constants and bulk modulus are given in units of GPa.

Property	Pedone (300 K) [28]	Pedone (T= 0 K)	This work	Experiment
a (Å)	18.5219	18.5243	18.3335	18.2350
b (Å)	8.8489	8.8493	8.7116	8.8180
c (Å)	5.2582	5.2585	5.1820	5.1790
Ω (Å^3)	861.8050	862.0083	827.6299	832.764
C_{11}	202.9	202.9	260.4	224.7
C_{22}	115.2	115.4	158.9	177.9
C_{33}	155.7	155.5	210.8	213.6
C_{12}	50.1	50.2	63.4	72.4
C_{13}	32.8	32.9	50.3	54.1
C_{23}	14.6	14.6	50.2	52.7
C_{44}	68.3	68.4	86.0	77.6
C_{55}	61.6	61.6	74.3	75.9
C_{66}	53.5	53.5	63.6	81.6
B	68.4	68.5	102.5	107.8

In the case of enstatite and ferrosilite, only an aggregate value of the dielectric constant could be found from experiments which was higher than all three diagonal components of computed dielectric constants. The reason for the discrepancy between the experimental and computed values of dielectric constants could be due to the fact that in the formalism of pair potentials, dielectric polarization of the ions is not taken into account. This conclusion is also supported by our calculation of the dielectric constants with a shell model potential developed by Tilocca et al. [49]. The calculated values of dielectric constants using this model were found to be much closer to the experimental values, as shown in Table 2.6. Shell-model potentials attempt to account for atomic polarization of the ions. The core represents the nucleus plus core electrons, and the shell represents the valence electrons which are able to respond to a local electric field. The interaction between the core and

Table 2.4: Computed and experimental properties of ground state fayalite compared with experimental values. First column reported values from [28]. Elastic constants and bulk modulus are given in units of GPa.

Property	Pedone (300 K) [28]	Pedone (T = 0 K)	This work	Experiment
a (Å)	4.8727	4.8924	4.8508	4.8200
b (Å)	10.2539	10.2727	10.3386	10.4790
c (Å)	6.0564	6.0837	6.0686	6.0870
Ω (Å^3)	302.6050	305.7522	304.3459	307.4469
C_{11}	296.0	263.3	269.8	266.0
C_{22}	178.5	152.1	156.5	168.0
C_{33}	217.4	191.8	205.8	232.0
C_{44}	50.6	40.6	28.7	32.3
C_{55}	64.3	53.4	54.7	46.5
C_{66}	72.0	62.6	62.6	57.0
C_{12}	76.8	64.6	57.6	94.0
C_{13}	81.6	67.3	62.3	92.0
C_{23}	76.0	68.1	71.6	92.0
B	123.7	107.1	108.6	134.0

shell is given by a harmonic potential

$$u_{cs}(r) = \frac{1}{2} k_{spring}\, r^2, \tag{2.9}$$

where k_{spring} describes the spring and r is the separation between the core and the shell of a given ion. In response to external electric fields and other interactions, the shell will be displaced from the core representing polarization of the ion.

To summarize, the potential parameters reported here (Table 2.1) proved to be a better fit for the crystals olivine and orthopyroxene. In Chapter 3, we use this modified and improved potential to study radiation damage in these minerals.

Table 2.5: Computed and experimental properties of ground state orthoferrosilite compared with experimental values. Values in the first column are from [28]. Elastic constants and bulk modulus are given in units of GPa.

Property	Pedone et al. [28] (T = 0 K)	This work	Experiment
a (Å)	18.6658	18.5584	18.4180
b (Å)	8.8512	8.8556	9.0780
c (Å)	5.2640	5.2389	5.2366
Ω (Å^3)	869.6935	860.9917	875.5522
C_{11}	208.0	222.2	198.0
C_{22}	133.9	131.6	136.0
C_{33}	179.0	171.6	175.0
C_{44}	70.2	79.7	59.0
C_{55}	60.2	63.1	58.0
C_{66}	54.1	55.5	49.0
C_{12}	65.8	55.4	84.0
C_{13}	51.5	35.4	72.0
C_{23}	43.0	43.1	55.0
B	89.9	85.0	101

Table 2.6: Computed and experimental dielectric constants of forsterite, fayalite, enstatite, and ferrosilite. Forsterite and fayalite values from experiments are taken from [47], and the orthopyroxene values (i.e., enstatite and ferrosilite) are taken from [48]. The values from [49] were computed using a shell model.

Minerals	Experiment	This work	Pedone et al. [28]	Tilocca et al. [49]
Forsterite	$\varepsilon_{xx} = 7.16$	$\varepsilon_{xx} = 3.53$	$\varepsilon_{xx} = 3.09$	$\varepsilon_{xx} = 6.09$
	$\varepsilon_{yy} = 7.61$	$\varepsilon_{yy} = 4.56$	$\varepsilon_{yy} = 3.92$	$\varepsilon_{yy} = 7.34$
	$\varepsilon_{zz} = 7.03$	$\varepsilon_{zz} = 3.48$	$\varepsilon_{zz} = 3.11$	$\varepsilon_{zz} = 5.96$
Fayalite	$\varepsilon_{xx} = 8.80$	$\varepsilon_{xx} = 3.89$	$\varepsilon_{xx} = 3.17$	–
	$\varepsilon_{yy} = 8.92$	$\varepsilon_{yy} = 5.19$	$\varepsilon_{yy} = 4.12$	–
	$\varepsilon_{zz} = 8.58$	$\varepsilon_{zz} = 3.76$	$\varepsilon_{zz} = 3.22$	–
Enstatite	$\varepsilon = 8.4$	$\varepsilon_{xx} = 3.70$	$\varepsilon_{xx} = 3.14$	$\varepsilon_{xx} = 6.08$
	–	$\varepsilon_{yy} = 4.11$	$\varepsilon_{yy} = 3.50$	$\varepsilon_{yy} = 6.94$
	–	$\varepsilon_{zz} = 4.22$	$\varepsilon_{zz} = 3.17$	$\varepsilon_{zz} = 6.91$
Ferrosilite	$\varepsilon = 8.4$	$\varepsilon_{xx} = 3.78$	$\varepsilon_{xx} = 3.28$	–
	–	$\varepsilon_{yy} = 4.28$	$\varepsilon_{yy} = 3.56$	–
	–	$\varepsilon_{zz} = 4.33$	$\varepsilon_{zz} = 3.43$	–

CHAPTER 3: RADIATION DAMAGE IN OLIVINE AND ORTHOPYROXENE

3.1 Introduction

Minerals on the surfaces of airless bodies including the moon, Mercury and asteroids are impacted by energetic solar wind, cosmic rays and micrometeorite which causes damage to their crystalline structures and introduces defects [1, 11, 50]. Transmission electron microscopy (TEM) of lunar samples reveals characteristic amorphous rims caused by a combination of radiation damage, sputtering, and impact vapor deposition [1, 12–14]. As mentioned in Chapter 1, recent analysis of samples from asteroid Itokawa suggests nanophase iron inclusion could be produced by radiation damage as well as through vaporization-condensation resulting from micrometeorite impact [15, 16]. The mechanisms by which radiation damage can result in amorphization and npFe^0 inclusions lack a complete understanding.

Space weathering rates of minerals have been found to be correlated with mineral composition. In laboratories, space weathering has been simulated using ion bombardment [51–55] and pulsed laser heating, and the outcome of space weathering revealed compositional dependence. For example, in experiments where micrometeorite impacts were effected pulsed laser heating, it was found that spectral alterations take place more readily in olivine than in orthopyroxene [17, 18, 56]. Wang et al. [54] found that olivine required about four times higher radiation dose than enstatite to get amorphized, suggesting olivine might be more radiation resistant. Irradiation experiments using heavy ions by Christoffersen and Keller [51] showed a similar critical radiation dose for amorphization in olivine and enstatite, although olivine was found to be slightly more resistant to amorphization. In [55], radiation with He^+ ions consistent with solar wind conditions was used to determine the critical amorphization dose in olivine. However, no comparable experiment relevant for solar wind conditions exists for enstatite. Here we made effort to investigate through

atomic-scale simulations the underlying cause of the difference in space weathering in olivine and orthopyroxene.

Experimental investigation of the short-time scale evolution of the defects is difficult, and atomistic computer simulation has been proved to be useful in explaining the dynamical processes [57]. Atomic-scale simulation has been used to understand radiation damage in elemental metals or semiconductors [58], binary and more complex oxides including MgO [59], UO_2 [60, 61], CeO_2 [61], ZrO_2 [62], and $ZrCaTi_2O_7$ [63]. There have been very few computational studies on radiation damage in silicate minerals, the most notable being on zircon ($ZrSiO_4$) [64]. Olivine and orthopyroxene are two ubiquitous silicate minerals in the cosmos, and study of defects evolution in them have several scientific benefits.

Here we have carried out molecular dynamics (MD) simulations of the time evolution of the Frenkel defects in the minerals olivine (Mg_2SiO_4, Fe_2SiO_4) and orthopyroxene ($MgSiO_3$, $FeSiO_3$) at T = 1200 K and elucidated some aspects of the atomic-scale mechanism of space weathering caused by radiation damage in these minerals.

3.2 Approach to defect evolution study

Radiation damage generates Frenkel defects (interstitial-vacancy pairs), although more severe damage can lead to amorphization [65]. Annealing in radiation damaged material takes place through a number of processes, which include point defect migration, recombination of vacancies and interstitials, and the formation of extended defect structures, including dislocations and point defect clusters.

MD simulation of radiation damage has demonstrated that the kinetics of defect recombination, annihilation, and clustering can be obtained through a focus on the so-called kinetic phase. The defect structures that are observed to evolve after a full-scale simulation of the ballistic phase where a high energy primary knock-on atom (PKS) generates defects through atomic displacement

cascade, also called collision cascade, might be obtained simply by focusing on the evolution of randomly placed Frenkel pairs [59, 61]. The approach works for several reason. First, the time and length scale associated to the ballistic is very short, which are few picoseconds and few nanometers respectively [66]. Second, the number of generated and survived defects and volume of the cascade region are linearly dependent on the incident PKA energy [67]. We adopt the same approach, i.e., bypass the ballistic phase and consider only the kinetic phase. Specifically, we consider an initial distribution of Mg/Fe and O Frenkel defects. In a density functional theoretic study, it was found that the SiO_2 pseudo-Schottky defects were not energetically favorable [68] . Thus in the present study, the focus is directed toward understanding Mg/Fe and O Frenkel pairs.

3.2.1 Determination of stable interstitial sites

The starting structures for MD simulation were prepared in a two-step process. In the first step, stable locations for interstitial Mg/Fe cations and O anions were determined. As we have described in Chapter 2, many of the octahedral and tetrahedral sites in olivine and pyroxene remain unoccupied. Ideally, these sites could host interstitial cation or anion. Based on this local consideration, an interstitial was placed in a candidate interstitial site inside a unit cell of the crystal, and the structure was then relaxed (at T=0, P=0, resulting to force zero) using LAMMPS [69] and the displacements of the ions from their initial positions were recorded. It should be noted here, while determining possible interstitial sites, a Frenkel defect was placed with the vacancy and interstitial site widely separated so as to avoid any significant interaction. The final position of the interstitial in the relaxed unit cell was recorded in terms of fractional coordinate, and through the application of relevant space group ($Pbnm$ for olivine, $Pbca$ for orthopyroxene), all the crystallographically equivalent sites of this final position were generated. After introducing interstitials in all these symmetric sites, a visual inspection (using VMD) was made and this gave clue where a new crystallographically distinct interstitial site might possibly exist. With this new possible interstitial site, the same exercise described above was repeated, i.e., an interstitial was placed in the new sitek and

Table 3.1: Fractional coordinates of the olivine lattice [30]. Fractional coordinates for the two cation interstitial sites $M_{i,1}$ and $M_{i,2}$, and one anion interstitial sites $O_{i,1}$, determined in the present work, are also given.

M1	0.00000	0.00000	0.00000
M2	0.98975	0.27743	0.25000
$M_{i,1}$	0.52718	0.31430	0.25000
$M_{i,2}$	0.08281	0.85766	0.04677
Si	0.42693	0.09434	0.25000
O1	0.76580	0.09186	0.25000
O2	0.22012	0.44779	0.25000
O3	0.27810	0.16346	0.03431
$O_{i,1}$	0.52718	0.31430	0.25000

the structure (unit cell) was relaxed. This way, all the seemingly possible interstitial sites, both for cations and oxygen anion, were exhausted, and their positions were recorded in terms of fractional coordinates. At each candidate site, both cation and anion interstitials were considered.

For olivine, the above scheme produced two stable cation interstitial sites and one stable anion interstitial site. However, the anion interstitial site turned out to be the same as one of the two cation interstitial sites. For orthopyroxene, three crystallographically distinct interstitial sites and two distinct anion interstitial sites were obtained, and one interstitial site could stabilize both cation or anion since it turned out to be at a center of inversion symmetry. In Tables 3.1 and 3.2, along with the stable interstitial sites determined here, the fractional coordinates of the perfect olivine [30] and orthopyroxene [70] crystals are shown respectively.

3.2.2 Random placement of Frenkel defects

In the second step, Frenkel defects were randomly placed in the crystal lattice [59–61]. However, unlike [59–61], there was no requirement imposed that the initial interstitial sites and vacancy sites be separated by some minimum distance to prevent recombination in a very short time. Vacant sites were chosen at random with no preference for crystallographically distinct sites.

Table 3.2: Fractional coordinates of the orthopyroxene lattice [70]. Fractional coordinates for the four cation interstitial sites $M_{i,1}$, $M_{i,2}$, $M_{i,3}$, and $M_{i,4}$, and three anion interstitial sites $O_{i,1}$, $O_{i,2}$, and $O_{i,3}$, determined in the present work, are also given.

M1	0.3756	0.6539	0.8684
M2	0.3769	0.4846	0.3627
$M_{i,1}$	0.18839	0.56192	0.14328
$M_{i,2}$	0.50000	0.50000	0.50000
$M_{i,3}$	0.66858	0.33379	0.80381
$M_{i,4}$	0.42748	0.65659	0.56825
SiA	0.2715	0.3416	0.0495
SiB	0.4741	0.3379	0.7967
O1A	0.1834	0.3399	0.0371
O2A	0.3107	0.5019	0.0435
O3A	0.3027	0.2249	-0.1714
O1B	0.5627	0.3403	0.7981
O2B	0.4335	0.4844	0.6933
O3B	0.4478	0.1986	0.5988
$O_{i,1}$	0.1998	0.68303	0.12735
$O_{i,2}$	0.50000	0.50000	0.50000
$O_{i,3}$	0.55163	0.68732	0.59068

For each system studied, about $\sim 1\%$ of cations and anions were displaced from their perfect crystal sites to generate Frenkel pairs.

After placing the initial Frenkel defects, the structure was relaxed to a zero-temperature structure. The relaxation caused many ions in the crystal structure to displace significantly from their equilibrium lattice site. This is indicated in the snapshots of the defect structures taken before and after the relaxation step (Fig. 3.1). In this figure, only the point defects are shown which are defined in the following manner: displaced ions were identified as point defects if their coordinates are different from their equilibrium lattice site by more than 1 Å. Similarly, a lattice site, cation or anion, was identified as vacancy if there were no ion within 1 Å of the equilibrium site. The additional ion displacements occurred due to the long range Coulomb interactions between the defects and lattice strain.

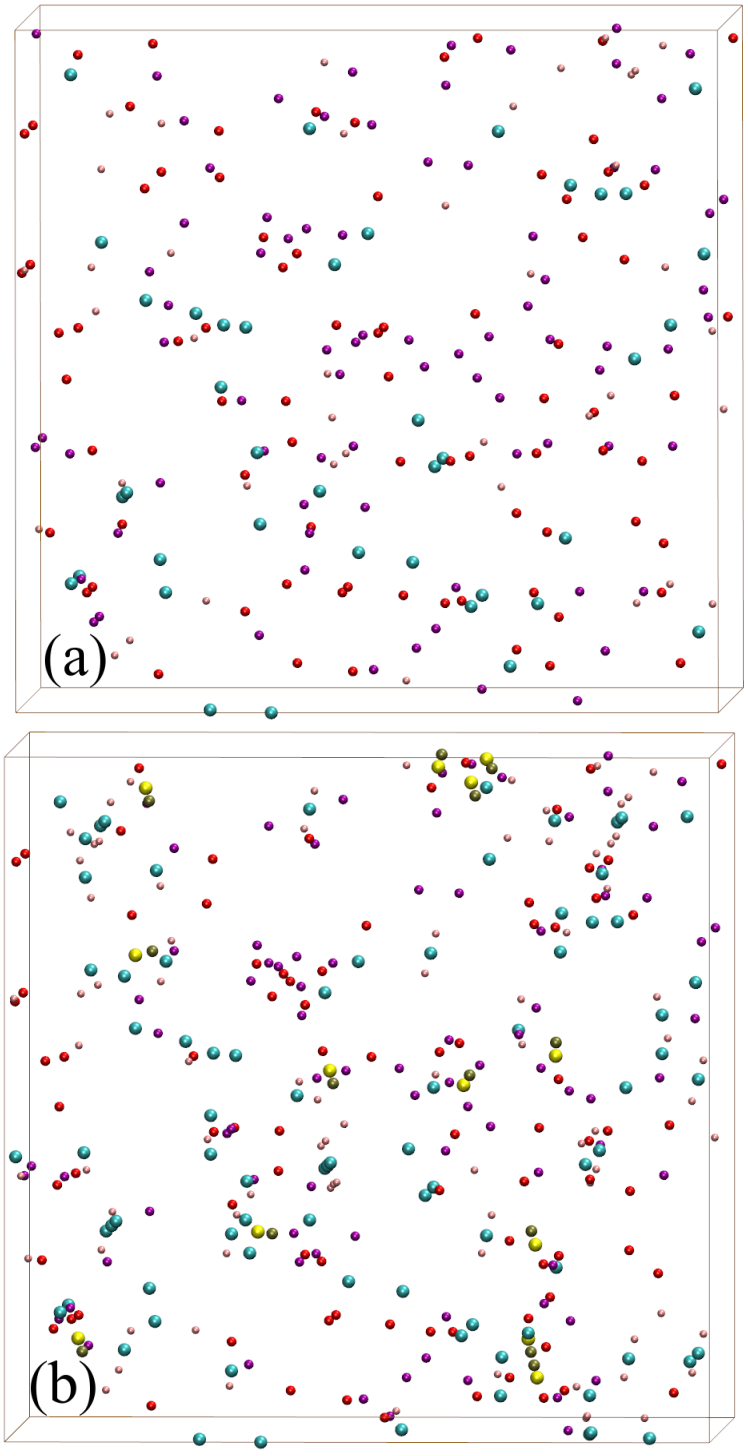

Figure 3.1: In (a), the initial defect structure for olivine (forsterite) is shown before relaxation was carried out in LAMMPS [69]. In (b), the number of defects has increased due to relaxation and interactions between the defects. Color scheme: Grey spheres = Mg interstitial, blue = Mg vacancy; red = O interstitial, purple = O vacancy; yellow = Si interstitial, green = Si vacancy.

In determining the count of Frenkel defects, not all displaced ions are considered. Vacancy-interstitial pairs that are separated by a distance less than 1.7 Å, which is comparable to the Si-O bond length in the silica tetrahedra, are considered to be part of a chain. Some point defects, while corresponding to significant displacements, resulted in vacancy-interstitial pairs or chains that were not widely separated and did not satisfy this criteria. In counting the number of Frenkel defects within a chain or cluster of defects, the net excess of interstitials or vacancies in the chain was determined and was used to determine the effective number of Frenkel defects.

Though Si Frenkel defects were not included in the starting structure, it was observed that in some cases significant Si displacement occurred during relaxation. This resulted in neighboring Si interstitial-vacancy pairs, however since they were not separated by the cutoff described above, they were not considered to be Frenkel defects. Even though the Si interstitial and vacancy were closely spaced, they did not necessarily annihilate. Rather it turned out that these local Si displacements were crucial for stabilizing other local defects in the lattice. In particular, we found that the large Si displacements aided in maintaining fourfold coordination of Si in the SiO_4 tetradhedra, and this kind of displacement which helped maintain the fourfold coordination was observed for O also both in olivine and orthopyroxene.

The total number of initial cation and anion Frenkel pairs in olivine and orthopyroxene are shown in Tables 3.3 and 3.4. In addition, the number of initial displaced ions in the initial structure is given. The initial numbers of defects are obtained after relaxation to the zero-temperature defective structure. As can be seen from the tables, the number of displaced ions turned out to be larger than the number of Frenkel pairs. In Table 3.5, the number of displaced Si ions in the initial olivine and orthopyroxene structures are shown. Though the Si ions were displaced, no Si Frenkel defects were obtained per criteria described above.

Table 3.3: Initial numbers of displaced cations and cation Frenkel pairs (FP). Final numbers after 3 ns of annealing are also reported.

Material	Mg/Fe FP (initial)	Mg/Fe FP (final)	Displaced Mg/Fe (initial)	Displaced Mg/Fe (final)
Forsterite	41	17	81	42
Enstatite	29	25	34	29
Fayalite	43	14	103	44
Ferrosilite	28	20	29	27

Table 3.4: Initial numbers of displaced anions and anion Frenkel pairs (FP). Final numbers after 3 ns of annealing are also reported.

Material	O FP (initial)	O FP (final)	Displaced O (initial)	Displaced O (final)
Forsterite	64	17	83	31
Enstatite	57	23	149	66
Fayalite	64	9	102	18
Ferrosilite	49	20	134	73

3.3 Molecular dynamics specifics

The time evolution of the system was determined for 3.0 ns using MD at constant temperature T = 1200 K and constant volume using LAMMPS code [69] . The volume corresponded to zero stress in the perfect crystal at temperature T = 1200 K. For olivine simulations, the supercell included $11 \times 5 \times 9$ unit cells and a total of 13860 ions. For orthopyroxene, $3 \times 6 \times 10$ unit cells and a total of 14400 ions were simulated. The number of the unit cells along different crystal axes were so chosen that system box size remains approximately cubic and avoids any simulation artifacts. Periodic boundary conditions were applied in all three directions. Coulomb interactions were computed using Wolf method using a cutoff of 12 Å and a damping parameter $\alpha = 0.2$ [71, 72]. The Morse potential was also computed using a cutoff of 12 Å. The integration time step was chosen to be 0.5 fs which ensured energy conservation. The partial charges of different elemental species were taken from the potential model as described in section 5 of Ch. 2.

Table 3.5: Initial numbers of displaced Si and Si Frenkel pairs (FP). Final numbers after 3 ns of annealing are also reported. Note that no Si Frenkel pairs were observed.

Material	Si FP (initial)	Si FP (final)	Displaced Si (initial)	Displaced Si (final)
Forsterite	0	0	13	15
Enstatite	0	0	13	17
Fayalite	0	0	14	9
Ferrosilite	0	0	18	10

3.4 Time evolution of Frenkel defects

3.4.1 Anisotropic diffusion of cations and anions

The number of displaced Mg/Fe, Si, and O ions for olivine and orthopyroxene are shown as a function of time in Figs. 3.2 and 3.3 respectively. It can be seen number of displaced Mg/Fe cations decreases more rapidly in the olivine minerals in comparison to the orthopyroxene minerals. The number of displaced O ions decreases substantially for each system studied, however, relatively large numbers of O ions persist in the orthopyroxene minerals in comparison to the olivine minerals. Finally, in all the minerals, the number of displaced Si ions changes with time but the changes are relatively small and are seemingly not systematic.

The time evolution of the total number of displaced ions was found to be strongly correlated with the fraction of remaining Frenkel pairs in the simulation at any given point of time. In Fig. 3.4, the number of Mg, Fe, and O Frenkel pairs as a function of simulation time is shown for olivine and orthopyroxene minerals. It can be seen that cation defects heal more slowly than anion defects in both type of minerals. However, olivine and orthopyroxene differ in the time evolution of the defects. Specifically, cation and anion Frenkel defects heal more slowly in orthopyroxene than in olivine. Later, it will be shown that these differences can be attributed to differences in the diffusion behavior and tendencies to trap point defects into larger clusters between the two minerals.

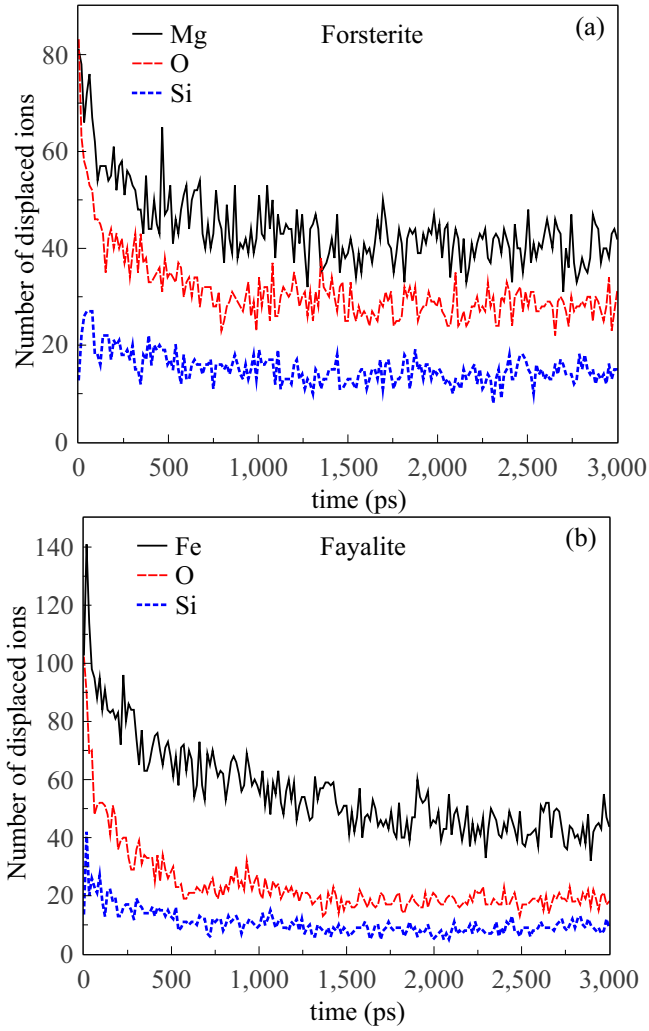

Figure 3.2: Total number of "displaced ions" (explained in text) as a function of time for the olivine minerals (a) forsterite and (b) fayalite.

In Figs. 3.5 and 3.6, mean squared displacements of the ions as a function of time are shown for olivine and orhthopyroxene respectively. Initially, the rate of diffusion is rapid for a very short duration, then it decreases due to both vacancy-interstitial annihilation and trapping of point defects into stable clusters. In olivine, cations diffuse more rapidly than anions. By contrast, anion diffusion is more rapid than cation diffusion in orthopyroxene. In enstatite, rapid oxygen diffusion is observed. Finally, though Si ions undergo significant displacements to maintain local

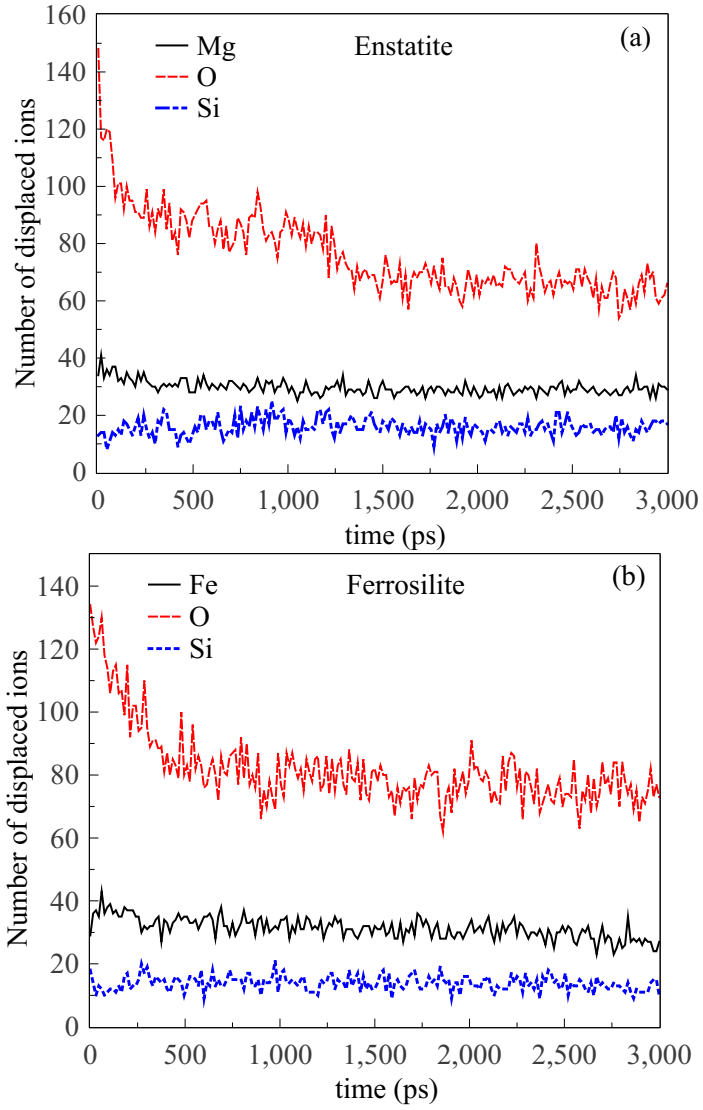

Figure 3.3: Total number of "displaced ions" (explained in text) as a function of time for the orthopyroxene minerals (a) enstatite and (b) orthoferrosilite.

coordination of the tetrahedra, they never exhibit displacements characteristic of diffusion. The rapid decrease in the number of cation Frenkel defects in olivine can be traced to fast cation diffusion. In contrast to olivine, cation defects diffuse rather slowly in orthopyroxene minerals. As expected, annihilation of Frenkel defects is governed by the diffusion rate. Since anion diffuse rapidly in orthopyroxene, it might be expected that anion Frenkel defects should annihilate more

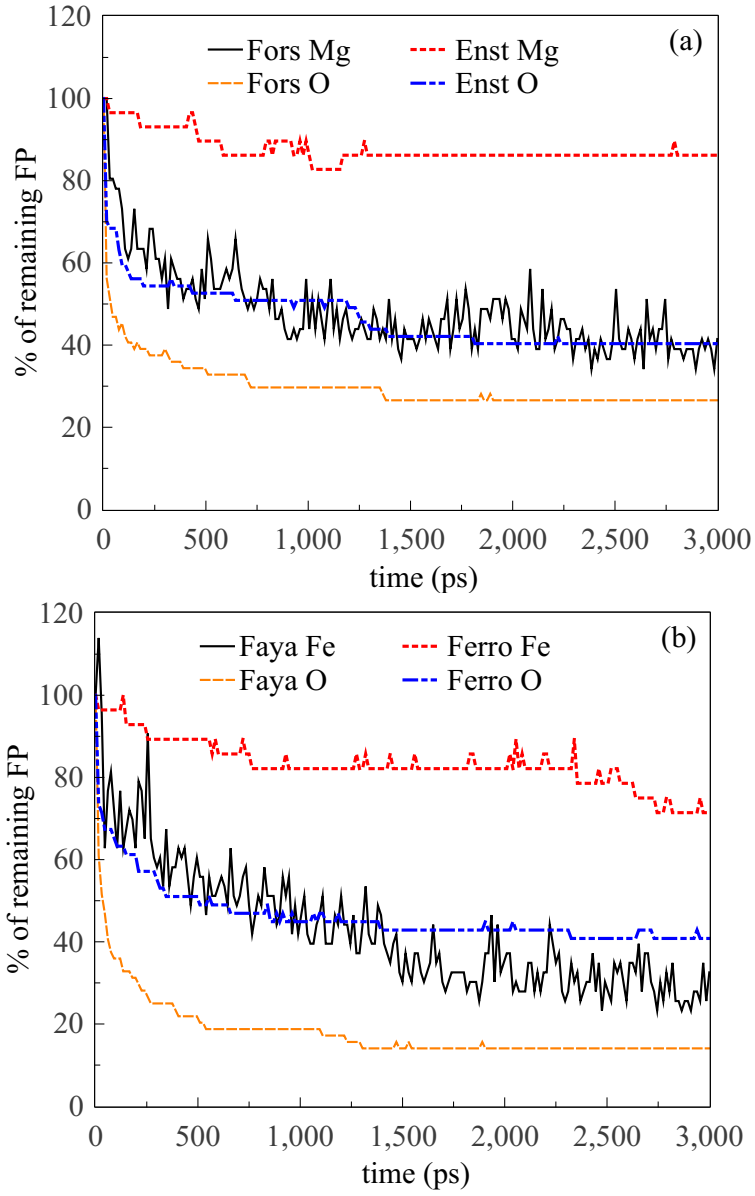

Figure 3.4: In (a), the number of remaining Mg Frenkel pairs (FP) and O FP in forsterite and enstatite are plotted as the percentage of their initial counts versus time. In (b), remaining Fe FP and O FP in fayalite and orthoferrosilite are plotted the same way. The figures clearly indicate anion FP anneal is much faster in olivine (forsterite, fayalite) than in orthopyroxene (enstatite, ferrosilite).

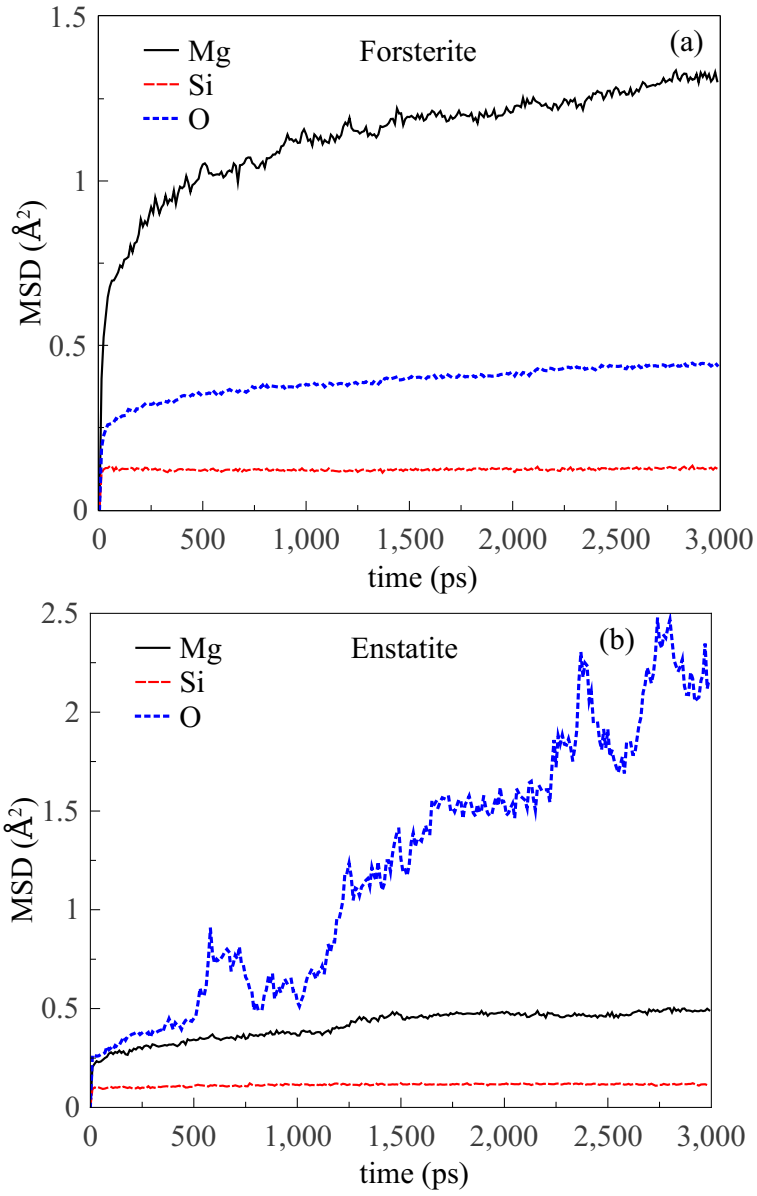

Figure 3.5: Mean squared displacement of different ion species as a function of time in (a) forsterite, and (b) enstatite. While Mg cation is more mobile in forsterite, O anion is more mobile in enstatite. Similar difference is also observed in the case of fayalite and ferrosilite (Fig. 3.6), thus indicating that anions are more mobile in olivine than in orthopyroxene.

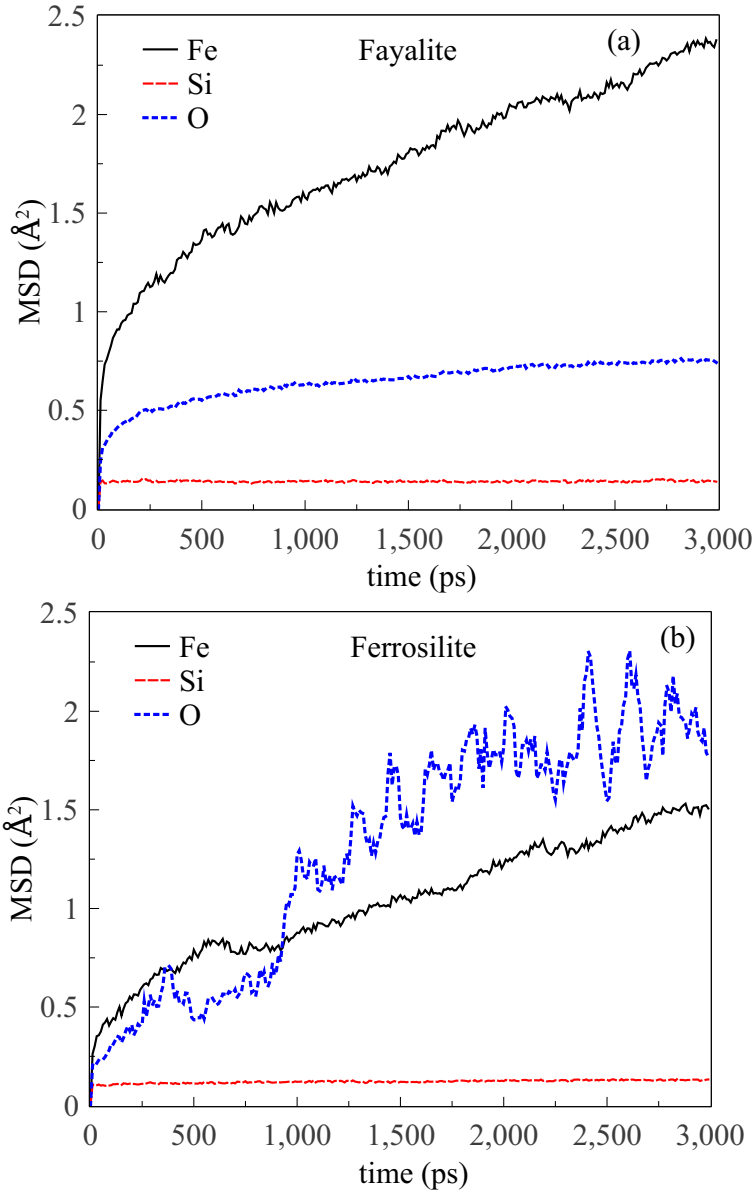

Figure 3.6: Mean squared displacement of different ion species as a function of time in (a) fayalite and (b) ferrosilite.

rapidly in orthopyroxene in comparison to olivine. However, the data in Fig. 3.4 indicates otherwise, that is, anion Frenkel defects annihilate more rapidly in olivine. The reasons for this apparent anomaly is connected to the strong anisotropy in point defect diffusion observed in orthopyroxene.

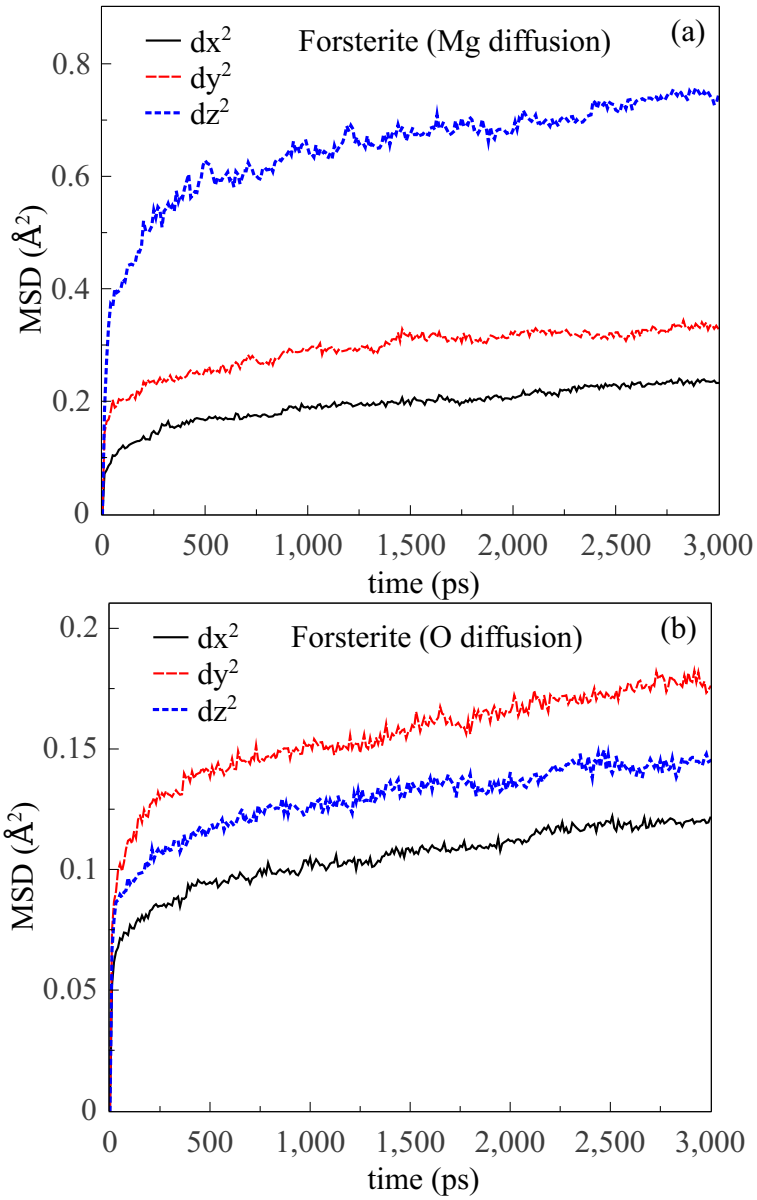

Figure 3.7: Components of the mean squared displacement of (a) Mg and (b) O along the three crystal axes in forsterite. The cation is found to have the highest diffusion rate along c axis, which is in agreement with previous experimental result Buening and Buseck [73].

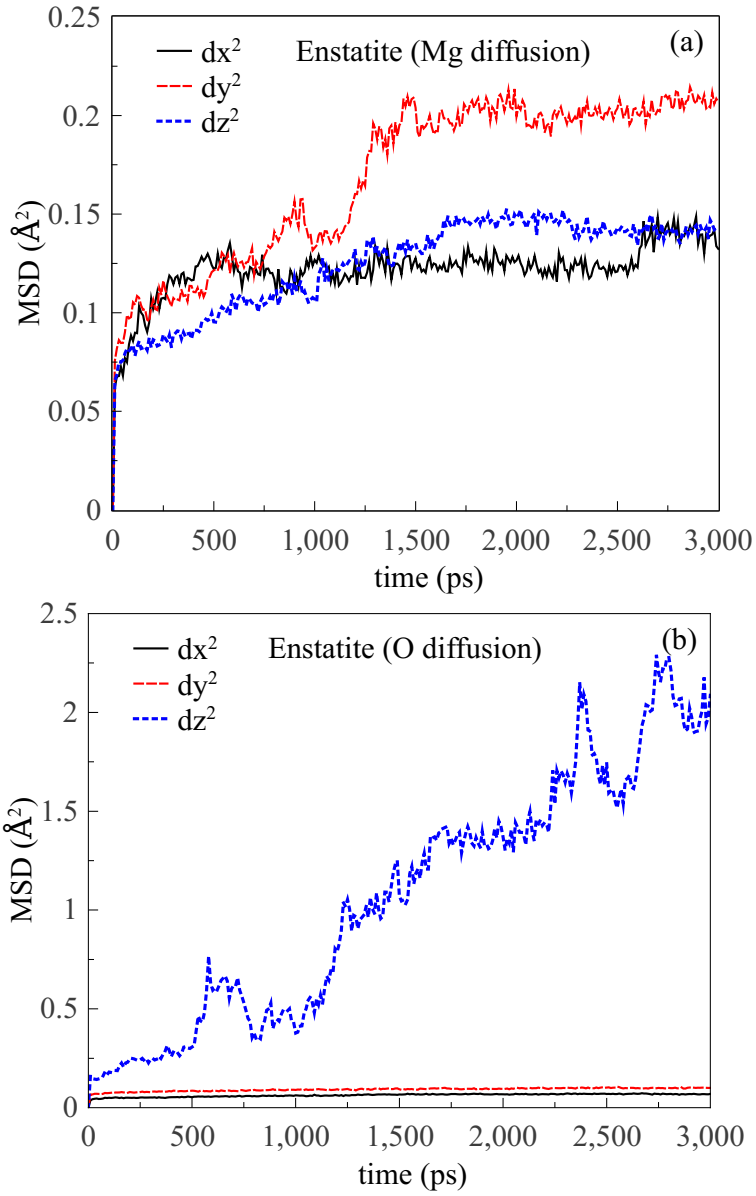

Figure 3.8: Components of the mean squared displacement of (a) Mg and (b) O along the three crystal axes in enstatite. The anion diffusion rate demonstrates large anisotropy, in agreement with experiments Farver [74].

To explain the above point further, the x, y, and z components of the mean squared displacements are shown in Fig. 3.7 for forsterite and are shown in Fig. 3.8 for enstatite. Here, the x, y, and z Cartesian directions are chosen along the a, b, and c axes, respectively, of the orthorhombic olivine and orthopyroxene unit cells. In Fig. 3.7, cation diffusion shows significant anisotropy, but for anions, anisotropy is not so evident. By contrast, in enstatite (Fig. 3.8), cation diffusion is only weakly anisotropic, whereas anion diffusion is very strongly anisotropic. In particular, anion defects diffuse almost exclusively along the z direction in enstatite, which corresponds to the c ($[001]$) crystallographic axis. This explains the reason for Frenkel defects to heal more slowly in orthopyroxene than in olivine despite the very strong anion diffusion in orthopyroxene. Since anions diffuse effectively along only one direction, vacancies and interstitials are constrained and less likely to annihilate. The most effective mechanism for anion diffusion along the $[001]$ direction in orthopyroxene is found to involve breaking and reforming bonds along the corner-linked tetrahedra in orthopyroxene. As the oxygen defects migrate along that direction, the system generally maintains the fourfold coordination of Si ion. Though this mechanism is effective at transporting oxygen defects, it is very inefficient for healing the lattice via interstitial-vacancy annihilation.

Experimental evidence for anisotropic diffusion of both cation and anion in olivine has been reported in the literature. In experiments on Mg-Fe interdiffusion, Buening and Buseck [73] reported that cation interdiffusion is the highest along the c axis which is in agreement with Fig. 3.8. This effect was explained using atomic-scale defect calculations in [75]. Our simulation results for anisotropic diffusion of oxygen is in qualitative agreement with the experimental results from Reddy et al. [76] where diffusion rates were found to be the largest along the b axis.

Anisotropic cation diffusion had also been observed in enstatite [77]. Schwandt et al. [77] reports at T = 1200 K, cation diffusion is the highest along the c axis and the lowest along the b axis, which is at odd with our results. Fig. 3.8 indicates that cation diffusion is the greatest along the b axis. One possible explanation for this discrepancy is that the results presented here are dominated by interstitial diffusion, whereas experiments are likely to be dominated by vacancy mediated

processes. Indeed, in our simulations, we find cation vacancies in enstatite to be immobile within the 3 ns of simulation time.

The most revealing feature in Fig. 3.8 is the large and strongly anisotropic oxygen diffusion in enstatite. There is no corresponding experimental result that uses enstatite, however, the result is consistent with the experimental results for diopside ($CaMgSi_2O_6$) [74]. Though diopside is compositionally and structurally distinct from orthopyroxene, it is characterized by an interlocking chains of SiO_4 along the c axis similar to enstatite. Oxygen diffusion in diopside along the c axis was found to be 100 times greater than that along the a and b axes [74]. In addition to c axis, oxygen also diffuses rapidly along a axis unlike the result we obtained [74, 78].

3.4.2 Defect cluster formation

As time evolves, point defects get trapped in energetically stable clusters and this lead to decrease in diffusion rate and defect annihilation both in olivine and orthopyroxene. The dominant mechanism for trapping defects in both olivine and orthopyroxene is rearrangement of bonds in the SiO_2 network to maintain tetrahedral coordination of the Si ions. Thus, as bonds break and form during diffusion, Si ions try to remain coordinated with four oxygen nearest neighbors.

Several Coulomb-neutral clusters are observed in olivine. For example, cation and anion vacancies are often found together in Schottky clusters. In presence of an oxygen vacancy, the local structure rearranges so that an oxygen ion is shared between neighboring tetrahedra and this way Si maintain the fourfold coordination. Trapping of cation and anion vacancies in Schottky clusters leads to local transformation of olivine structure to short-range order similar to orthopyroxene.

As in olivine, in orthopyroxene, where corner sharing between neighboring tetrahedra is intrinsic to the perfect crystal, the fourfold coordination of Si is preserved by different mechanisms. Anion vacancies in orthopyroxene can cause local rearrangement of bonds so that additional sharing of oxygen ions occurs between neighboring tetrahedra. Anion interstitials on the other hand tend to result in the breaking of corner-sharing bonds, resulting in independent tetrahedra. Cation

interstitials and vacancies lead to local rearrangement of the SiO_2 network. Since cation defects are relatively immobile in orthopyroxene even without trapping, it turns out formation of Coulomb-neutral clusters is not an effective way trapping cation and anion defects as is the case in olivine. In fact, in orthopyroxene, anion displacements along the c axis, the direction along which tetrahedra are connected by corner-shared bonds, lead to breaking and reformation of bonds between neighboring tetrahedra, and this explains the very large diffusion rates of oxygens in orthopyroxene observed along the c axis.

In olivine, several defects clusters were identified, which are shown in Fig. 3.9. Several Mg/Fe split interstials were found, always with displacement of an ion from an M1 site. Only a few isolated Mg/Fe vacancies are found at M1 sites, consistent with the theoretical results in [75]. For anion defects, many instances of split interstitials were found. No split anion vacancies were observed. The observance of split interstitials is in agreement with previously reported density functional theoretic (DFT) calculations where it was shown that split cation interstitials were energetically favorable over various tetrahedral and octahedral sites [79]. Cation and anion vacancies are trapped in clusters in olivine. These include isolated nearest-neighbor Schottky clusters at M1-O2 or M1-O3 sites. In addition, vacancies at M2 and O3 nearest-neighbor sites lead to formation of a split cation vacancy. Many bound Schottky clusters at second-nearest neighbor sites form as well, for example at M2 and O1 sites. One frequent structure that was observed particularly in forsterite consists of two cation vacancies and two anion vacancies occurring at second-nearest neighbor sites. These clusters also involved large displacement of an Si ion. In particular, an Si with two neighboring anion vacancies is displaced to form two corner-sharing bonds with neighboring tetrahedra. In Fig. 3.10, a defect cluster of this type observed in forsterite is shown. Interestingly, stable Schottky clusters are often formed at second-nearest neighbor sites, and prevented the formation of nearest-neighbor bound Schottky clusters.

The defect clusters in olivine described above are consistent with a local transformation from olivine to pyroxene. In olivine minerals, this local transformation represents the most impor-

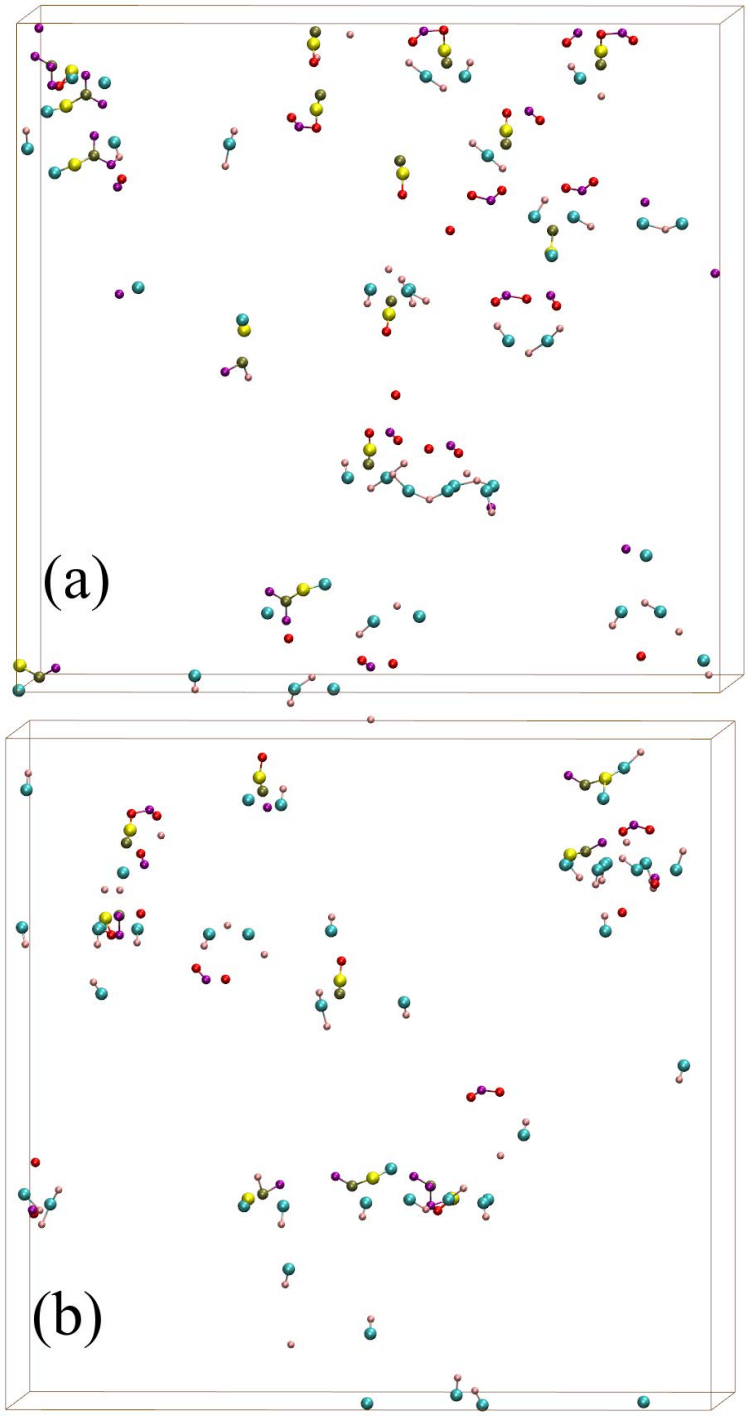

Figure 3.9: The final defect structures of (a) forsterite and (b) fayalite (annealing time 3 ns). The color scheme is the same as used in Fig. 3.1. Comparison of the final defect structure of forsterite with its initial defect structure (Fig. 3.1(b)) reveals that most of the FP get annihilated, while the surviving FP either form defects cluster or remain as isolated interstitials and vacancies.

tant trapping mechanism for point defects that inhibits vacancy-interstitial recombination. Transformation of olivine to an amorphous material with pyroxene composition has been observed in interplanetary dust particles [80]. However, in that case, the transformations take place on a global scale, i.e., compositional change occurs in the entire mineral, as opposed to local transformations observed in the MD simulations where the overall composition remains stoichiometric to olivine.

3.4.3 Energy calculation of defect clusters

We computed energies of isolated Schottky clusters and examined some general trend. The cluster formation energies were determined with respect to perfect-crystal MgO. The energy of an MgO or FeO Schottky defect in forsterite was determined by computing the energy of supercells of perfect-crystal forsterite with N MgO units, forsterite with a single Schottky defect and $(N-1)$ MgO units, and perfect-crystal MgO. The energy E_S for a Schottky defect was computed using

$$E_S = E^{Fo}_{(N-1)} + E_{MgO} - E^{Fo}_N, \tag{3.1}$$

where $E^{Fo}_{(N-1)}$ is the energy of a supercell of defective forsterite with a single Schottky defect, E^{Fo}_N is the energy of a supercell of perfect-crystal forsterite, and E_{MgO} is the energy of a single formula unit of MgO in the rocksalt structure. The size of the supercell used for the forsterite energy calculations was the same as those used in the defect annealing, so that the number of MgO units was $N = 3960$ in the perfect crystal and $(N-1) = 3959$ in the defective cell. In this way, the energy is defined as the energy per MgO Schottky defect. Because the calculations were performed with relatively large simulation cells with dimension along any direction ~ 50 Å, interactions that occur due to periodic boundary conditions were small, which justifies the use of supercell methods rather than the Mott-Littleton approach. Moreover, the defect energies computed for the supercell should be most relevant to the energetics of defects in the annealed system.

In Table 3.6, we tabulate formation energies for nearest-neighbor, second nearest-neighbor,

and widely separated Schottky pairs. The relatively low formation energies for M1-O2, M1-O3, and M2-O3 Schottky clusters explains their observed presence in the annealed structures. All of the other possible nearest-neighbor pairs result in significantly higher formation energies, and consequently were not observed in the annealed structures. Note also that relaxation of the M2-O3 cluster resulted in the formation of a split cation vacancy bound to the anion vacancy, as was observed in the annealed structures.

Table 3.6 als shows the energy of Schottky defects where the two vacancies were widely separated but remained in the same supercell. These energies are, as expected, larger than those of the Schottky clusters, since the Schottky clusters are bound attractively by Coulomb interactions. The energy values from Walker et al. [79] are also tabulated for comparison, and they turn out to be substantially larger than our caomputed values. The reasons for this disagreement are twofold: first, the values reported in Walker et al. [79] are computed using the Mott-Littleton method as implemented in GULP [42] which do not include the attractive interaction between the vacancies in the Schottky pair. These values, therefore, most closely correspond to the values we obtained with widely separated Schottky pairs. Second, Walker et al. [79] uses an empirical potential with formal point charges, whereas we have used partial charges. The use of formal point charges is likely to exaggerate the ionic nature of olivine, and thereby magnify the Schottky energies. Thus, due to differences in computational models and methods, a quantitative comparison cannot be made between our results and those in [79]. However, Table 3.6 demonstrates similar trends in both set of Schottky energies. It is clear that both M1 and O1 sites result in the largest Schottky defect energies. Both the O2 and O3 sites are more favorable than the O1 sites for oxygen vacancies. Also, M1 sites are significantly more favorable for Mg vacancies than the M2 sites.

A certain type of extended defect cluster, which is observed in the final forsterite and fayalite structures, involves an MgO (FeO) Schottky pair with a displaced Si ion. In this cluster, the Si ion is displaced by $\sim$ 1.6 Å toward the Mg (Fe) vacancy. Near the original Si site, an O vacancy was generally observed. The sites for the Mg (Fe) and O vacancies were found at the

Table 3.6: Schottky defect energies E_S (see Eq. 2) for nearest-neighbor, second nearest-neighbor, and widely separated Schottky pairs in forsterite. Values are given in eV.

Schottky pair	Nearest-neighbor energy	2nd nearest-neighbor energy	Widely separated Scottky pair energy	Calculated from Walker et al. [79]
M1O1	4.66	4.15	6.12	11.14
M1O2	2.99	–	4.27	8.37
M1O3	3.38	–	4.67	7.71
M2O1	5.96	3.99	7.27	13.06
M2O2	4.03	4.58	5.42	10.29
M2O3	4.24	3.35	5.82	9.63

second nearest-neighbor sites. The vacant sites for these extended clusters were found to be in the combinations M1-O1, M2-O1, M2-O2, and M2-O3. The formation energy of these second nearest-neighbor Schottky pairs are also shown in Table 3.6. It can be seen that in some cases, the energy of the extended, second-nearest neighbor clusters is lower than the formation energy of corresponding nearest-neighbor Schottky pairs. This suggests that Schottky clusters are readily trapped at second-nearest neighbor sites, thereby preventing the formation of nearest-neighbor Schottky clusters.

The formation energy of the Schottky cluster shown in Fig. 3.10 was also computed. As mentioned before, clusters of this type were frequently found in forsterite. No clusters of this kind were observed in the annealed fayalite. The energy of formation of this entire cluster is calculated to be 4.194 eV. Since the structure involved two MgO Schottky pairs, this means formation energy of each Schottky pair was 2.097 eV, which is significantly lower than the lowest formation energy among all the nearest-neighbor MgO Schottky pairs shown in Table 3.6. This explains the stability of these clusters and their frequency in the annealed forsterite structure.

The energies of various Frenkel defects in forsterite were also computed and compared with those reported in [79] in Table 3.7. The energy of a Frenkel defect was determined by placing an interstitial and a vacancy at far distant sites. In the present work, in contrast to [79] where only

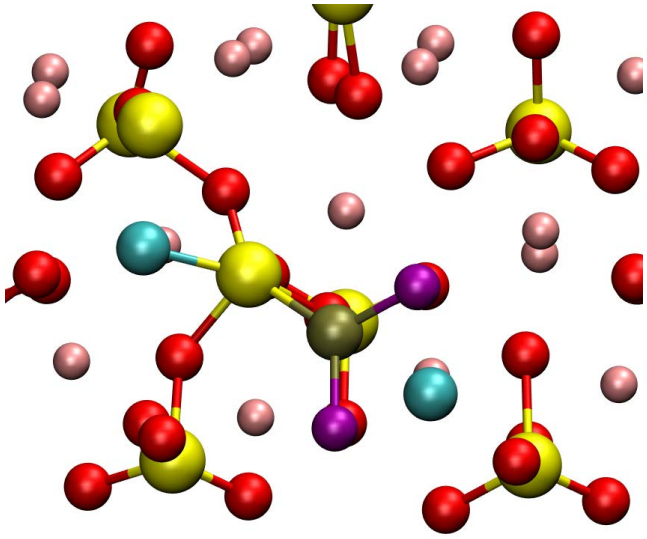

Figure 3.10: Structure of a common defect cluster observed in olivine. The structure consists of a displaced Si, two oxygen vacancies (purple spheres) and two Mg vacancies (blue spheres). One of the Mg vacancies is nearest-neighbor to both the oxygen vacancies, while the other is located at a second nearest-neighbor position. The Si inside the tetrahedron which contains the oxygen vacancies undergoes a significant displacement, thereby trapping two MgO Schottky pairs and forming a charge neutral cluster. The displaced Si shares new bonds with neighboring tetrahedra to maintain its fourfold coordination.

split interstitials were observed, we found that it was possible to stabilize Mg interstitials at two distinct sites $M_{i,1}$ and $M_{i,2}$. However, in the annealed structure split Mg interstitials with the same structure as that reported in [79] were indeed observed, and the energy of this structure is also given in Table 3.7 for direct comparison to [79]. The values computed using the potential reported here are somewhat lower, apparently due to the fact that partial charges were used. Interestingly, we find that Frenkel defects that correspond to a split Mg interstitial are actually somewhat higher in energy. We did not explore the energies of near vacancy-interstitials pairs, which would be expected to be bound by Coulomb interactions in the same way that Schottky clusters are bound.

The evolution of orthopyroxene minerals with Frenkel defects exhibits some mechanisms in common with olivine, but also some unique characteristics. In Fig. 3.11, the point defect structure of orthopyroxene is shown after 3 ns of simulation time for ferrosilite. From this figure, it is evident

Table 3.7: Frenkel defect energies for forsterite. For the Mg Frenkel defects, the vacancy was at an M1 site in each case. For the oxygen Frenkel defect, the vacancy was at an O2 site. Values are given in eV.

Frenkel pair	This work	Calculated from Walker et al. [79]
$Mg_{i,1}$	4.35	–
$Mg_{i,2}$	4.34	–
Split Mg interstitial	4.88	6.73
$O_{i,1}$	6.27	9.09

that the dominant mechanism of evolution is the migration of anion interstitials along the c axis. This results in chains of anion vacancies and interstitials. A closer look at these chains reveals that there is only one extra anion interstitial in each chain. This is consistent with the large, anisotropic diffusion of anion described previously. In contrast to the behavior of anion interstitials, cation defects and isolated anion vacancies are fairly immobile. This is consistent with the observation of slow healing rates in orthopyroxene. Specifically, while anion interstitials are extremely mobile, diffusion only occurs along the c axis. Hence, the likelihood of an anion interstitial encountering an anion vacancy for recombination is relatively low. Moreover, the slow diffusion rates for cation defects and anion vacancies also makes trapping into extended clusters less likely to occur.

As with olivine, the presence of isolated cation or anion defects in orthopyroxene can result in significant displacements of Si ions. These in turn tend to occur while maintain fourfold coordination of the tetrahedra, but significant overall reorganization of the network. In particular, displacements of the Si ions tends to break the bonds that join tetrahedra along the c axis, and alternately forming new bonds in the perpendicular directions. Hence, Si displacements primarily occur perpendicular to the c axis. It is also apparent that large Si displacements tend to act in a way that immobilizes cation defects and prevents annihilation of cation Frenkel defects. Specifically, there are several instances in orthopyroxene where Si ions are displaced away from a cation interstitial toward a cation vacancy. In this structure, the cation interstitial tends to relax toward

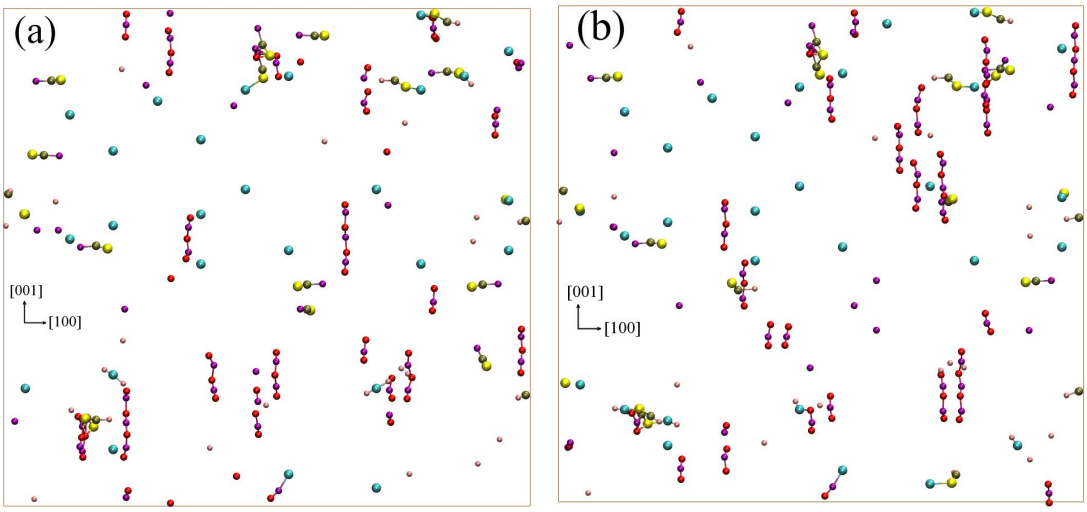

Figure 3.11: Snapshots of enstatite defect structures at (a) 2.5 ns and (b) 3 ns. A close examination of these figures reveals that while the Mg interstitials (grey spheres) and Mg vacancies (blue spheres) remain essentially trapped and immobile, long connected chains of oxygen vacancies (purple spheres) and oxygen interstitials (red spheres) continuously appear and disappear (annihilate) along the $[001]$ direction.

the vacancy Si site. This essentially results in the Frenkel pair being stabilized by the formation of (Mg,Fe)/Si anti-site defects.

As mentioned before, displacements of ions and migration of defects tend to occur to maintain the fourfold coordination of the tetrahedra. Some of these mechanisms are shown in Fig. 13, in this case for enstatite. In Fig. 3.12(a), an Mg and O interstitial are bound together, resulting in a disruption of the bonds joining neighboring tetrahedra. In Fig. 3.12(b), the presence of an isolated oxygen vacancy is stabilized by a bond joining tetrahedra along a direction perpendicular to the c axis. Finally, in Fig. 3.12(c), an oxygen interstitial results in disruption of bonds joining neighboring tetrahedra together. In short, defects are accommodated in the lattice by rearrangement of the SiO_4 network, with bonds breaking and forming so that each Si ion tends to be coordinated with four O ions.

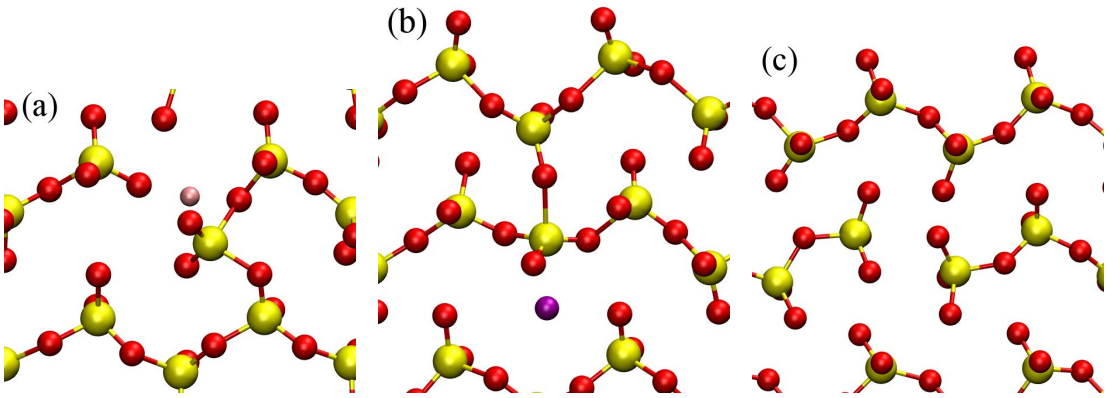

Figure 3.12: Different mechanisms in orthopyroxene that occur in response to local defects which act to maintain the fourfold coordination of the Si ions, as described in the text. In (a) a Mg interstitial (grey sphere) causes rearrangement of the SiO_2 network. In (b), an oxygen vacancy (purple sphere) results in an additional bond joining neighboring tetrahedra. In (c), an extra oxygen interstitial results in the chain of tetrahedra becoming broken.

3.5 Discussion

Experiments reported in [54] indicate that olivine is more resistant than orthopyroxene to amorphization due to radiation damage. The same trend was reported in [51], although the results were within the experimental error. The results from atomic-scale simulation of radiation of these minerals described here provide an explanation for these observations. In the simulated annealing, cation and anion Frenkel defects were found to heal more rapidly in olivine due to strong differences in the diffusion between the two crystal structures. In orthopyroxene, oxygen defects migrate rapidly along the c axis by a mechanism which rearranges the bonds between SiO_4 tetrahedra. This phenomena appears to lead to local disruption of the oxygen sublattice and potentially amorphization of the tetrahedral network. Although the oxygen diffusion in orthopyroxene is rapid, its one-dimensional nature renders it very inefficient at healing Frenkel defects. In olivine, by contrast, diffusion was found to be more isotropic. As a result, even though the defects in olivine can become easily trapped in clusters, there is also a greater probability of annihilation of Frenkel defects and healing of the crystalline lattice.

While this study was on radiation damage, the results nonetheless shed some light on the pulsed laser experiments reported in [17, 18, 56], where changes in the optical reflectivity of olivine were found to be more significant than orthopyroxene. Given the apparent tendency of olivine to be more resistant to radiation damage, this might at first seem conflicting. The key to this is to recognize that the laser heating experiments were primarily focused on optical effects and the production of npFe^0, whereas TEM analysis of radiation damage was focused on determining the critical dose for amorphization, and not necessarily reduction. We propose that as the surface is reduced, oxygen should diffuse from the bulk of the system to replenish oxygen lost at the surface. The simulations reported here show that orthopyroxene is significantly more efficient at transporting oxygen from the bulk to the surface, thereby preventing strong reduction of the surface. By contrast, the larger cation mobility in olivine should tend to result in the rapid formation and growth of Fe inclusions that are characteristic of space weathering.

These predictions suggest specific features that might be observed in strongly reduced materials, either produced in natural space weathering or in the laboratory via pulsed laser heating. In particular, if oxygen lost on the surface is replenished by diffusion from deeper in the bulk, then surface reduction should be less significant on orthopyroxene, but might penetrate deeper into the bulk. For olivine, oxygen is less mobile, and hence surface reduction might be expected to be more significant at the surface, but with more shallow penetration into the bulk. Surface reduction of olivine should also be stabilized by the more rapid cation diffusion and formation of Fe metal inclusions.

3.6 Conclusions

The atomic-scale simulations of defects in olivine and orthopyroxene revealed that defect diffusion and clustering occur by mechanisms which act to maintain the coordination of the SiO_4 tetrahedra. While this aspect is common to both olivine and orthopyroxene, there were some

clear and striking differences. Specifically, cation diffusion occurs more readily in olivine than in orthopyroxene, which lead to faster healing of Frenkel defect and trapping of defects in point defect clusters. Several forms of defect clusters including split interstitials and split vacancies were observed. Diffusion of anion interstitials in orthopyroxene was found to be highly anisotropic, leading to long chains of anion vacancies and interstitials. This anisotropy, despite the rapid anion diffusion, inhibits both recombination with anion vacancies and trapping into point defect clusters. The differences observed in the evolution of radiation damage provides some explanation in the differences of amorphization and space weathering in these minerals.

CHAPTER 4: DUST GRAINS COLLISION AND SURFACE CHEMISTRY

4.1 Introduction

As described in Chapter 1, the stage of planet formation where dust grains collide and grow to kilometer-sized planetesimals is not completely understood. In this regime, where gravitational force is negligible, dust accretion is thought to occur primarily by van der Waals (vdW) interactions between mineral grains. Earth-based experiments on collisional accretion and numerical simulations on the basis of Johnson-Kendall-Roberts (JKR) theory [22] reveals that dust grains can grow up to a radius of $\sim$ 1 mm and for relative speed up to 10 m s^{-1} beyond which the collisions result in bouncing or fragmentation [25, 81, 82].

The experiments and simulations reported previously have some inherent limitations. In this paradigm, surface chemistry, e.g., the chemical environment at the surface essentially has no role in the outcome of the collision. This is in contrast to the observation that friction and adhesion between solid surfaces generally involve strong chemical bonds and can depend on surface adsorbates. Experiments to date have generally paid little attention to the chemical state of the surfaces. Yet the chemical environment of the Earth, where collisional aggregation is often studied, is quite different from that in the environment of space. For example, when a mineral is fractured in the oxygen and water-rich environment of the Earth, dangling bonds on the surface tend to rapidly react. By contrast, much less is known about the chemical properties of mineral surfaces in space environment. In computataional simulations, the models do not have a mecahnism to incorporate chemistry in them. For exampl, JKR theory considers adhesion by balancing elastic and surface energy.

In recent years, experimental tribology has demonstrated that surface adsorbates can play often an important or even dominant role in adhesion and friction. It therefore seems quite likely that experimental studies of tribological and dissipative properties of mineral grains should more

clearly relate properties to the chemical state of the surfaces.

Within this purview, we set forth to carry out atomic-scale simulations using classical molecular dynamics (MD) to explore how surface chemistry affects the outcome of collisions of nanometer-sized amorphous silica (a-SiO_2) grains. The motivation was a study of this nature would shed light on chemical effects on dissipation and adhesion, and thus elucidate some of the hitherto unconsidered effects in submicron grain collisions.

4.2 Molecular dynamics specifics

Silica grains, both amorphous and crystalline, have been used as prototype of cosmic silicates in the majority of collision experiments (e.g., [83, 84]) and coarse-grained numerical simulations (e.g, [5]). Silica has similar properties, like high sublimation temperature, high Young moduli etc. similar to that possesed by grains important for terrestrial planets formation [85]. We also use a-SiO_2 particles in this work to elucidate chemical effects in collisional dissipation and adhesion,

As menioned in Chapter 2, ReaxFF potential can describe chemistry, and since we were interested in the surface chemistry of dust grain collisions, we chose ReaxFF approach to model a-SiO_2 nanoparticles as well as to simulate their collision. In particular, we used the potential developed by Kulkarni et al. [3] to describe interactions between oxygen and a silica surface. ReaxFF involves numerous sets of parameters where each best describes the dynamics of a certain chemical environment or condition and which are fit to ab initio calculations, choice of a certain set of parameters can be important in a specific purpose or context. The potential in [3] was the result of two successive reparametrization of a Si-O potential that described materials involving silicon and silicon oxides, their interfaces, hydrolysis [86]. In the first reparametrization, water-silica interaction was considered [87]. Later, Kulkarni et al. [3] extended it to incorporate gas-surface interaction.

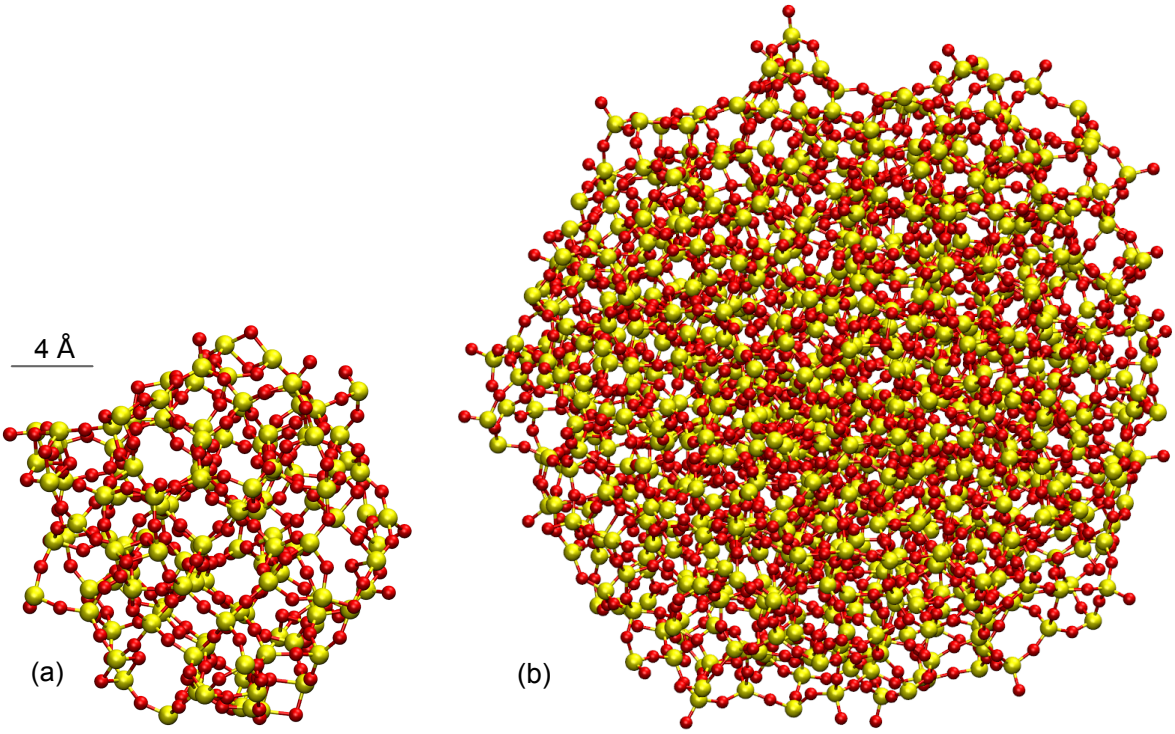

Figure 4.1: Nonhydroxylated amorphous silica nanoparticles generated through molecular dynamics with LAMMPS. Si ions are yellow and O ions are red. (a) A small nanoparticle containing 127 SiO_2 units ($a \sim 10$Å). (b) A large nanoparticle containing 894 SiO_2 units ($a \sim 20$Å).

We used ReaxFF implementation within LAMMPS [69] package to prepare a-SiO_2 nanoparticles and to simulate two-particle collisions. Non-periodic boundary conditions were applied in each step of the particle preparation and the collisions. Energy conservation was ensured using a MD timestep of 0.2 fs. The cutoff for Coulumb interaction was 10 Å.

4.3 Preparation of nonhydroxylated a-SiO_2anoparticles

Two spherical a-SiO_2 nanoparticles with different sizes were generated using the LAMMPS MD code. The structure of the silica nanoparticles are shown in Fig. 4.1. The small nanoparticle was made from 127 SiO_2 units, and the larger was made from 894 SiO_2 units. The initial structures were generated by selecting spherical segments from an α-quartz crystal. The radii of the small

and large particles were about 10 Å and 20 Å respectively. To generate the desired amorphous particles, the systems were first melted and then slowly cooled to T = 0 K. This general approach is quite standard for the generation of a-SiO_2 Feuston and Garofalini [88]. In some instances it was found that partial recrystallization occurred, and consequently there was some experimentation to find a procedure that yielded a relatively spherical, a-SiO_2 nanoparticle. Though both spherical and irregularly-shaped grains are believed to have played roles in the formation of planetesimals [85], the particles in our studies were taken to be nearly spherical, so that the results would be controlled more by surface chemistry rather than surface roughness and variations in contact area during a collision. Lack of spherical symmetry often leads to more complex dynamics involving rolling, sliding, and deflection [89, 90].

The small nanoparticle was melted at T = 3500 K using the ReaxFF potential and then was cooled to 0 K in one single run using a constant cooling rate of 1×10^{13} K s^{-1}. In preparing the large nanoparticle, the empirical pair potential developed in [91] was used. After melting the large nanoparticle at T = 3600 K, it was cooled to 0 K in several subsequent runs in a constant temperature regime. First, it was cooled to 2600 K using a constant cooling rate of 1×10^{14} K s^{-1}. The system was then run at constant energy for 20 ps to achieve greater structure relaxation. The system was again cooled to $\sim$1600 K using the same cooling rate, followed by a 20 ps run of constant energy MD. This cycle was repeated, and eventually the system temperature reached near 0 K.

4.3.1 Surface energy of nonhydroxylated nanograins

Although the two nanoparticles were generated using two different force fields and two different routes for cooling the silica melt, the resultant amorphous nanoparticles revealed very similar structural properties. Surface energies, γ, were computed using the formula

$$\gamma = \frac{1}{4\pi a^2} \left[E_{np} - n E_{bulk} \right], \tag{4.1}$$

where E_{np} is the total energy of the nanoparticle of approximate radius a, E_{bulk} is the energy of bulk a-SiO_2 per SiO_2 unit, and n is the number of SiO_2 units contained in the nanoparticle. E_{bulk} was calculated by first generating bulk a-SiO_2 from an α-quartz structure consisting of 450 SiO_2 units using ReaxFF and employing periodic boundary conditions, and then relaxing the structure to its ground state at temperature T = 0 K and pressure P = 0. The value of E_{bulk} was computed to be -22.81 eV/formula unit SiO_2. The computed surface energies were γ = 0.04 eV/Å^2 for both small and large nonhydroxylated nanoparticles, correct to within the error inherent in the calculation. These values fall within the range of surface energies reported in the literature, which is rather wide. Kimura et al. [92] provides a comprehensive list of experimental values obtained with different techniques, where values range from as low as γ = 0.0003 eV/Å^2 to as high as 0.274 eV/Å^2. Our values for surface energy of the a-SiO_2 nanoparticles are also comparable to some of the numerical results reported in the literature. For example, Roder et al. [93] did a numerical calculations with a 432 ion a-SiO_2 nanoparticle using the Beest-Kramer-van Santen (BKS) potential, and obtained a value of $\gamma = 0.078$ eV/Å^2 at T = 2850 K, with temperature dependence suggesting a value $\gamma \approx 0.11$ eV/Å^2 at T = 0 K . While this value is double the value we have obtained, it is well known that pair potentials with fixed point charges systematically result in cohesive energies greater than experiment by a similar factor [94]. First-principle calculations of the surface energy of a-SiO_2 are absent in the literature; therefore, we compare to energies computed for crystalline quartz surfaces. Goumans et al. [95] reported a value of 0.022 eV/Å^2 of a reconstructed α-quartz (001) surface obtained via periodic density functional calculations. The close agreement between the values of our calculated surface energies with those obtained from experiments as well from first-principle calculations validates our approach of generating the amorphous nanoparticles, and also the empricial ReaxFF potential that has been used.

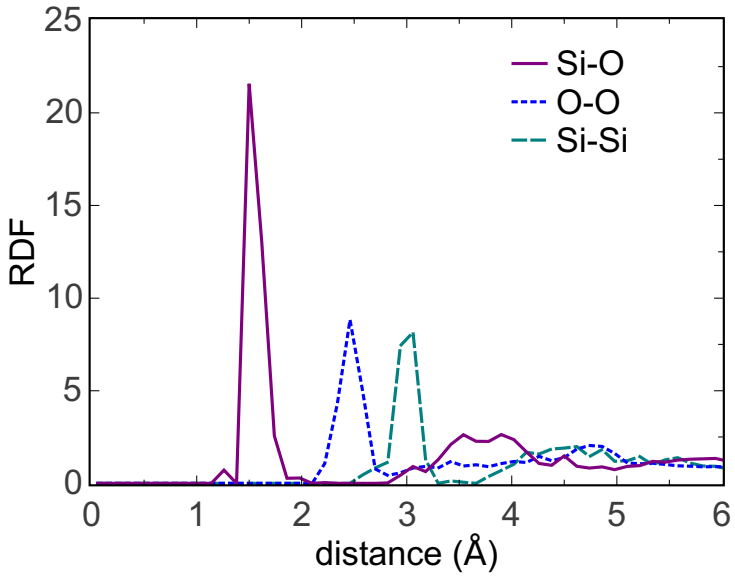

Figure 4.2: Radial distribution functions (RDF), $g(r)$, for the small nonhydroxylated nanoparticle. The first peak of each species corresponds to the nearest neighbor shell.

4.3.2 Radial distribution function

In addition to calculating surface energy, we determined the radial distribution functions (RDF) of both the particles in order to verify the amorphous structure of the generated particles. The RDF for the small nanoparticle is shown in Fig. 4.2. As expected, there is only one broad peak for each of the Si-O, O-O, and Si-Si pairs. The absence of long-range order in the RDFs of both the small and large nanoparticles demonstrates their amorphous nature.

4.4 Preparation of hydroxlyated nanoparticles

Hydroxylated nanoparticles were generated by adding water molecules to the a-SiO_2 silica nanoparticles prepared above. The atomic structures of the small and large hydroxylated nanoparticles are shown in Fig. 4.3. Hydroxyl groups and hydrogen atoms were attached to the undercoordinated Si and O sites. In determining the coordination number of Si and O, a cutoff radius of

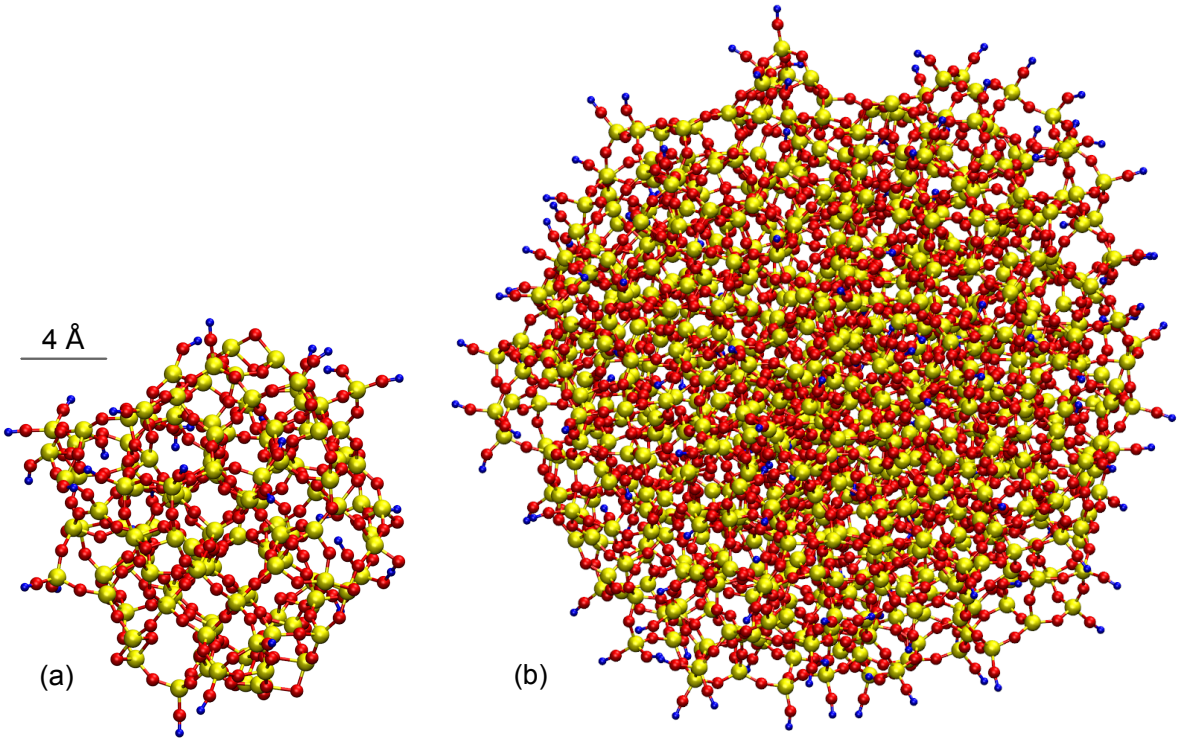

Figure 4.3: Hydroxylated amorphous silica nanoparticles. Si ions are yellow, O ions are red, and H ions are blue. (a) A hydroxylated small nanoparticle obtained by adding 16 water molecules to the particle in Fig. 1(a). (b) A hydroxylated large nanoparticle obtained by adding 88 water molecules to the particle in Fig. 1(b).

2.025 Å was used. For Si ions that lacked an O ion, i.e., which had a coordination number of 3, a tetrahedron was constructed with the Si ion at the centroid of the tetrahedron and three tetrahedral vertices were determined by the locations of the three bonded O ions. The location of the unoccupied vertex was determined and an OH group was placed at this point. Similarly, H atoms were placed near surface undercoordinated O ions. After hydroxylation, the atomic structure was relaxed to a ground state. A total of 16 H_2O molecules were attached to the small silica nanoparticle, and 88 H_2O molecules were attached to the large nanoparticle, yielding a hydroxylation density of 1.27 OH/nm^2 and 1.75 OH/nm^2 respectively. These values are similar to those determined by Leroch and Wendland [96] who obtained a density of less than 1 dangling bond/nm^2 from their

simulation of a-SiO_2 with a Morse-type pair-potential. Also, to achieve a hydroxyl density of 3 OH/nm^2, they randomly broke siloxane bonds (≡Si–O–Si≡ bridges with oxygen atoms on the surface) and attached OH groups at the newly created Si dangling bonds. Zhuravlev [97] reported an experimental density of 2.6 – 4.6 OH/nm^2 for fully hydroxylated bulk a-SiO_2 surface. Based on these previous studies, it seems likely that the hydroxylated surfaces used in this study had a lower OH density than might be expected in experiments, and that obtaining similar values to experiment would require breaking siloxane bonds to generate more sites for OH groups.

4.4.1 Energy of hydroxylation

The energy of dissociative adsorption of water molecules was computed using the following formula:

$$E_{ads} = (E_{np} + n_{H_2O}E_{H_2O} - E_{hyd,n_{H_2O}})/n_{H_2O}. \tag{4.2}$$

Here, E_{np} and $E_{hyd,n_{H_2O}}$ are the total energies of the nonhydroxylated and the hydroxylated nanoparticles, respectively, E_{H_2O} is the energy of a water molecule, and n_{H_2O} is the number of water molecules adsorbed on the nanoparticle surface. For the small nanoparticle, the value of E_{ads} was computed to be 2.9 eV/water molecule, whereas for the large nanoparticle the value was 3.1 eV/water molecule. These values are very close to the values obtained by C.-Vives [98] from their density functional theory (DFT) calculations. To reach a silanol density of 3.3 OH/nm^2 starting from a fully hydroxylated a-SiO_2 surface with silanol density 7.2 OH/nm^2, they removed 9 molecules of water, and the average energetic cost turned out to be 1.461 eV per water molecule. The removal of two additional water molecules needed much more energy, requiring 4.415 eV and 4.571 eV, respectively.

4.4.2 Surface energy of hydroxylated nanograins

The surface energy γ of the hydroxylated nanoparticles was also computed. In this case, the calculation assumes that the nanoparticle is in equilibrium with a reservoir of H_2O molecules at a chemical potential μ_{H_2O}. The surface energy for a nanoparticle with n_{H_2O} dissociatively adsorbed water molecules is,

$$\gamma = \frac{1}{4}\pi a^2 \left[E_{hyd,n_{H_2O}} - nE_{bulk} - n_{H_2O}\mu_{H_2O}\right]. \tag{4.3}$$

The value of μ_{H_2O} was determined by assuming that the system was in equilibrium with the reservoir,

$$\mu_{H_2O} = E_{hyd,n_{H_2O}} - E_{hyd,(n-1)_{H_2O}}. \tag{4.4}$$

In short, the change in energy of the system was determined as the result of removing a single H_2O molecule. Since this energy depends on the environment of the adsorbed water molecule, several calculations were done by removing different water molecules and an average value of μ_{H_2O} was obtained. This yielded a surface energy of γ = 0.05 eV/Å^2 for both small and large hydroxylated nanoparticles. While this value was higher than the surface energy for the nonhydroxylated particles, which was γ = 0.04 eV/Å^2, it did not have any implication in the sticking probability of the two types of particles during their collisions as will be evident later.

4.5 Simulation of collisions and analysis tools

To simulate collisions, the nanoparticles were initially placed such that the distance between their centers of mass was 55 Å for the small nanoparticle and 100 Å for the large nanoparticle. These distances were chosen to be much higher than the cutoff distance 10 Å of the empirical potential, and ensured that the nanoparticles did not interact with each other at the start of the collision simulation. After initial placement, both of the particles were kept stationary and were allowed to reach thermal equilibrium over a sufficient period of time ($\sim$20 ps) using a constant

energy run. The equilibrium temperatures computed were in each case very low, specifically below 25 K. After thermal equilibrium was attained, both particles were imparted equal but opposite velocities in order to simulate a head-on collision. The directions of the velocity vectors were chosen to lie exactly along the vector that connected the center-of-masses of the two particles, and as a result the total angular momentum of the system was zero. Collisions were simulated for 18 different velocities for the small and for 17 different velocities for the large nanoparticles over a range of 30 m s^{-1} to 2000 m s^{-1}. Since the surfaces and shapes of the nanoparticles were not completely uniform, it was expected that the outcomes of collisions would be described by a statistical distribution. To sample the distribution, Euler rotations were applied to the nanoparticles to generate 30 random orientations prior to collision at each specific velocity. Thus, by varying orientations and initial velocities, a total of 540 unique collisions were simulated for each of the following two cases: small nonhydroxylated nanoparticles and small hydroxylated nanoparticles. For the remaining two cases, i.e., collisions involving large nonhydroxylated nanoparticles and large hydroxylated nanoparticles, this number was 510.

Collision outcomes were first analyzed to determine whether the entire center-of-mass kinetic energy was dissipated resulting in a sticking event, or whether only partial dissipation occurred resulting in a bouncing event. In the case of complete dissipation, the irreversible work of adhesion was computed to determine the strength of the interaction between the two particles. For bouncing events, the coefficient of restitution was computed.

4.5.1 Work of adhesion

In order to calculate of the irreversible work of adhesion W_{adh}, the fundamental assumption made was that the translational kinetic energy was dissipated as internal thermal energy. Moreover, it was assumed that the thermal energy of this system was described by a collection of simple harmonic oscillators with average energy related to the temperature by the equipartition theorem. With these assumptions, the value of W_{adh} was determined from the values of the system temper-

atures before and after the collision event. The calculation of W_{adh} starts from a statement of the conservation of energy,

$$K_{trans} + K_{therm,i} + U_i = K_{therm,f} + U_f, \tag{4.5}$$

where K_{trans} is the translational kinetic energy before the collision, $K_{therm,i}$ and $K_{therm,f}$ represent the kinetic energy associated with internal thermal energy before and after the collision, respectively, and the terms U_i and U_f describe the potential energy before and after the collision. The potential energy terms can be separated into contributions due to the chemical bonds in the ground state and thermal vibrational energy:

$$U_i = U_i^{(0)} + \Delta U_{therm,i}, \tag{4.6}$$

$$U_f = U_f^{(0)} + \Delta U_{therm,f}. \tag{4.7}$$

Here U_i^0 and U_f^0 are the ground state energy of the chemical bonds before and after the collision, respectively. The terms $\Delta U_{therm,i}$ and $\Delta U_{therm,f}$ represent the thermal vibrational potential energy before and after the collision. Next we define the work of adhesion, W_{adh}, as the difference between the final and initial ground state potential energies,

$$W_{adh} = U_i^{(0)} - U_f^{(0)}. \tag{4.8}$$

This derivation makes it clear that W_{adh} represents the change in ground state potential energy associated with formation of chemical bonds at the interface between the colliding particles. Applying the equipartition theorem to the kinetic and potential contributions to the internal thermal energy, and using Eq. 4.5, the work of adhesion becomes,

$$W_{adh} = 3Nk_B(T_f - T_i) - K_{trans}, \tag{4.9}$$

where N is the total number of particles in the simulation and k_B is the Boltzmann constant. T_i and T_f are the temperatures of the nanoparticles before and after the collision event respectively, computed using the following equation:

$$T = \frac{2K}{3Nk_B}. \tag{4.10}$$

Here, K is the average thermal kinetic energy of the ions, i.e., average kinetic energy without the contribution from the translational motion of the nanoparticles.

A plot showing the evolution of system temperature during a typical collision as a function of simulation time is presented in Fig. 4.4. In Fig. 4.4, the temperature during the period t = 5-11 ps, which is the equilibrium temperature before the collision, is taken to be the initial temperature T_i and is about 25 K. At 11 ps, both the particles are given a velocity kick of 150 m s^{-1}, and this added translational kinetic energy manifests itself as a non-thermal temperature jump of about 18 K, resulting in a total of 43 K. The final temperature T_f is recorded after sufficient time has elapased and the particles have reached thermal equilibrium after the collision. In the example shown in Fig. 4.4, T_f = 38 K, averaged over the period t = 50 - 53 ps. These values of T_i and T_f are used in Eq. 4.9 to obtain the value of W_{adh}.

The energy associated with forming chemical bonds at the interface between two particles is given by W_{adh}, and the process of converting translational kinetic energy to internal thermal energy is dissipative and irreversible. In order for the grains to adhere, the translational kinetic energy must be completely dissipated as internal thermal energy. Specifically, in events where sticking occurs, the collision must be perfectly inelastic. Moreover, the approach to calculate W_{adh} is only valid and meaningful when the particles do completely adhere. Finally, it is clear that the magnitude of W_{adh} is a measure of the interaction strength between the two particles at the atomic scale, and hence should be correlated with the ability of the interactions to dissipate the kinetic energy as internal thermal energy.

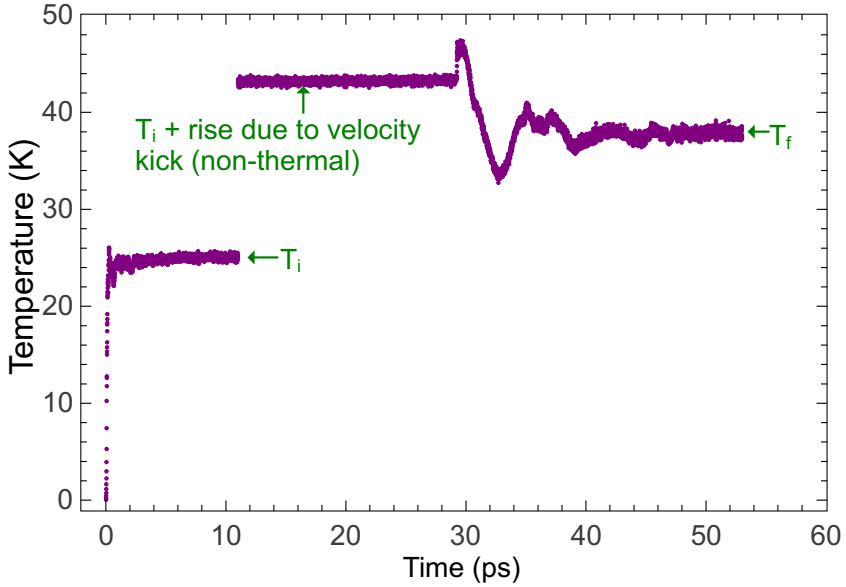

Figure 4.4: Plot of computed temperature for a collision between two large nonhydroxylated nanoparticles with velocity 150 m s^{-1}. The initial and final temperatures used in Eq. 4.8 to obtain W_{adh} are shown.

4.5.2 Coefficient of restitution

In the events where particles bounced instead of sticking, the COR was computed using the following formula:

$$COR = \frac{v_f}{v_i}. \tag{4.11}$$

Here, v_i and v_f are the relative speeds of the nanoparticles before and after the collision. As can be understood from the definition, a value of unity of COR indicates nearly elastic and reversible collision. By contrast, very small values of COR indicate that a sticking event nearly occurred. In a sticking event, the COR is exactly zero. In case of bouncing events, the collisional energy dissipated partially. As in the case of sticking, most of the kinetic energy was dissipated as vibrational thermal energy, however, some energy got dissipated as rotational kinetic energy.

4.6 Results and Discussion

4.6.1 Sticking probability of small nanoparticles

The probability of sticking both for nonhydroxylated and hydroxylated small nanoparticles as a function of velocity is shown in Fig. 4.5. In particular, the independent axis represents the magnitude of the initial velocity vector of both particles. Since the collision data were taken from a statistical distribution of different initial orientations, the mean values and standard deviations were computed at each simulated velocity. These are shown in the figures 4.5(a) and 4.5(b) along with the results of each individual calculation. The plots indicate that the probability of sticking depends on both the particle velocity and whether or not the surfaces are hydroxylated. At about 200 m s^{-1} and below, sticking dominates for both hydroxylated and nonhydroxylated particles, with a systematic greater probability of sticking for hydroxylated particles. Above 200 m s^{-1}, the probability of sticking for hydroxylated particles drops significantly, with most collisions resulting in bouncing at 400 m s^{-1}. However, it rises again at velocity about 500 m s^{-1} and above. By contrast, the sticking remains the most likely outcome with a probability higher than 0.6 for non-hydroxylated particles over the entire range of velocities. The sticking probability corresponding to 2000 m s^{-1} is 1, which needs to be explained. At this high velocity, the colliding nanoparticles undergo structural deformation that leads to high energy dissipation and the particles stick together for all orientations, yielding a value of 1 for the sticking probability.

4.6.2 Sticking probability of large nanoparticles

The probability of sticking in the case of the large nanoparticles is shown in Fig. 4.6, and exhibits a similar trend to that observed in case of the small nanoparticles. In this case, the outcome of the collisions depends more strongly on hydroxylation. For the nonhydroxylated particles, sticking is the dominant outcome with the exception of the interval between about 700 m s^{-1} and 1000 m s^{-1} where sticking and bouncing seems to be equally likely. By contrast, the likelihood

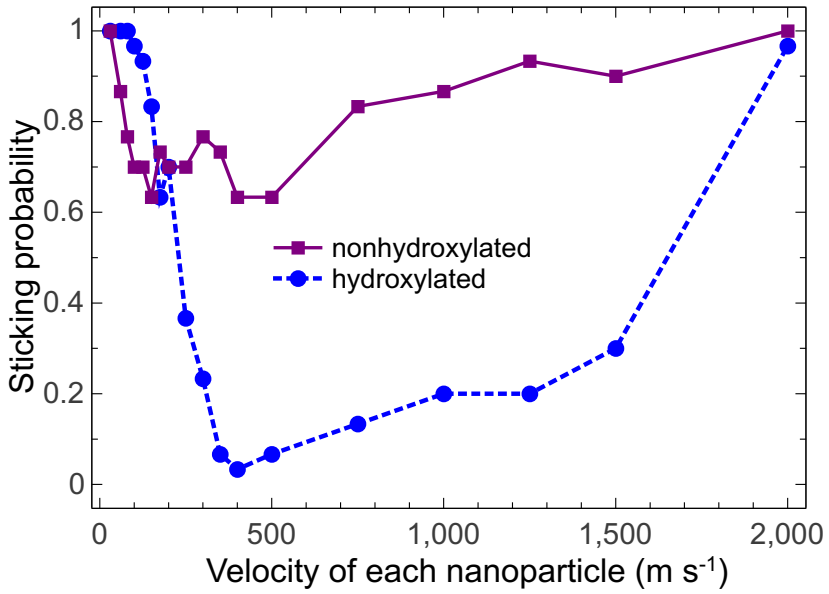

Figure 4.5: Outcomes of collisions of the small silica nanoparticles, for both the nonhydroxylated and hydroxylated cases, shown in terms of sticking probability.

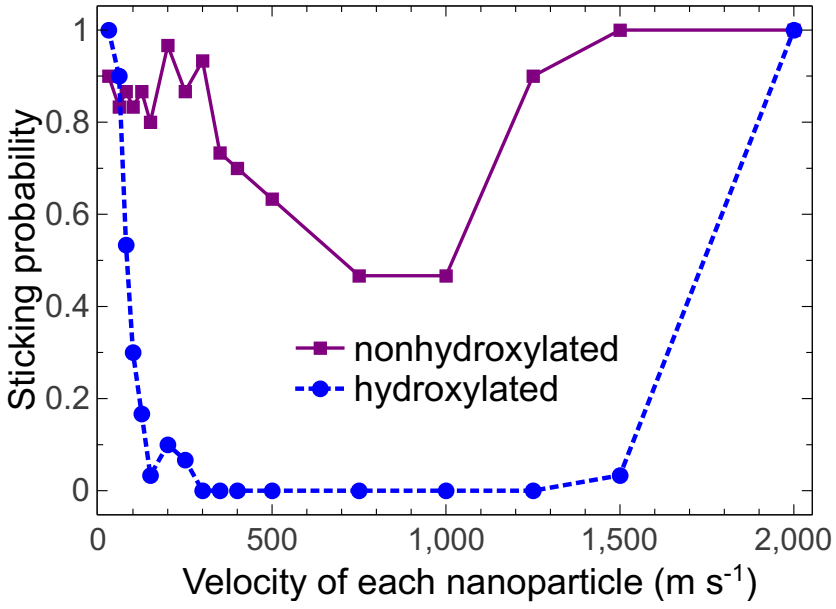

Figure 4.6: Outcomes of collisions of the large silica nanoparticles, for both the nonhydroxylated and hydroxylated cases, shown in terms of sticking probability.

of sticking of the hydroxylated grains for velocities above $\sim$ 150 m s^{-1} was very low. Comparison with Fig. 4.5 suggests that dependence on particle size is more pronounced when surfaces are hydroxylated. These results indicate that dependence on the chemical state of surfaces may actually be more significant when extrapolated to larger particle sizes. Finally, as in the case of small nanoparticles, the large nanoparticles underwent deformation and adhere together (Fig. 4.7) at velocity 2000 m s^{-1} for all the simulations, yielding a sticking probability of 1.

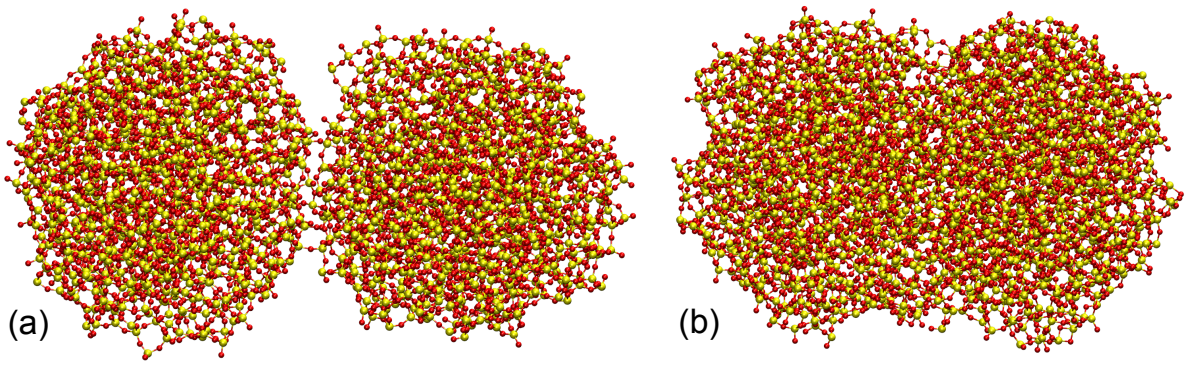

Figure 4.7: Sticking of two large nonhydroxylated silica nanoparticles approaching each other with (a) 60 m s^{-1} and (b) 2000 m s^{-1}. As can be seen in (b), a significant deformation of the particles takes place during collision at high impact velocities.

4.6.3 Work of Adhesion

The work of adhesion, W_{adh}, are plotted as a function of individual nanoparticle's velocity in Fig. 4.8 and in Fig. 4.9 for the small nanoparticles and large nanoparticles respectively. These plots do not include the results from all the collision events for two reasons. First, W_{adh}, as defined in Eq. 4.8 was meaningful only for those collision events where the outcome was sticking. For bouncing outcomes, the coefficients of restitution was the parameter to consider. Second, for some high velocity collisions, we obtained negative values of W_{adh} in addition to usual positive values. The negative values of W_{adh} indicate large internal deformation of the particles during collision, causing some of the center-of-mass kinetic energy to be converted into strain energy. In those

cases, bonds were disrupted in the interior of the particles while bond formation took place on the surface, resulting in an increase in the energy that did not correspond to internal thermal energy. Eq. 4.8 is not adequate to calculate W_{adh} for those events. Thus, in Fig. 4.8 and 4.9, we plotted W_{adh} only up to those velocities for which no negative value of W_{adh} was obtained. It may be noted here although we observed deformation of the particles in the simulations, no fragmentation was observed.

Fig. 4.8 shows that for sticking events the mean values of W_{adh} are only slightly larger for the small nonhydroxylated particles in comparison to the small hydroxylated particles. Specifically, for the hydroxylated particles, we find an average value of about 3.68 eV, in contrast to 3.93 eV for the nonhydroxylated particles. However, closer inspection reveals a larger range of values of W_{adh} for the nonhydroxylated particles, with maximum values approaching 12.88 eV. The plot in Fig. 4.8 also reveals that the standard deviation of the distribution of W_{adh} is larger for the small nonhydroxylated particles.

The same trend is observed for collisions involving the large nanoparticles with more pronounced effect (Fig. 4.9). Nonhydroxylated nanoparticles consistently exhibited significantly higher values of W_{adh} when compared to the hydroxylated nanoparticles, and the large nonhydroxylated particles exhibit a much broader distribution of W_{adh} and an increased likelihood of large values of W_{adh}. Several events yielded values of W_{adh} in the range between 20 – 40 eV.

A clear dependence of W_{adh} on the velocity of the particles cannot be established from the results, however, the large nanoparticles appear to show most of the large values of W_{adh} occurring at the largest velocities. This could indicate that deformation during the collision, which is more substantial at higher velocities, causes bond rearrangement and allows the particles to form more bonds at the interface. However, as mentioned before, at very high velocities, deformation resulted in a significant increase in the potential energy and in some cases yielded negative values for W_{adh}. This demonstrates that the collision energy can be dissipated as both internal thermal energy and strain energy associated with large deformations.

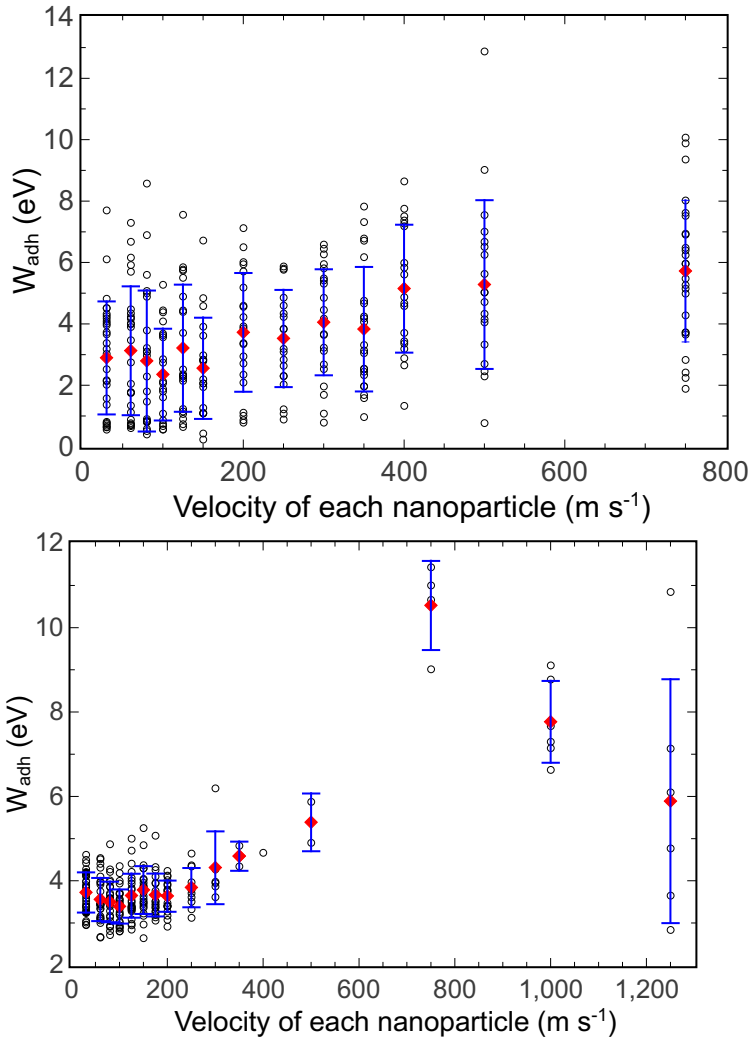

Figure 4.8: The work of adhesion, W_{adh}, calculated for a small (a) nonhydroxylated and (b) hydroxylated silica nanoparticle involved in the collisions for which the outcomes were particle sticking. Here, we plot W_{adh} only up to the velocity for which a positive value of W_{adh} was obtained.

The results presented above demonstrate that the chemical state of the surface plays a critical role in determining the ability of the interactions between the grains to dissipate translational kinetic energy. This behavior cannot be explained solely by vdW interactions between the particles, which is the usual approach taken during modeling intergrain interactions. Strong chemical

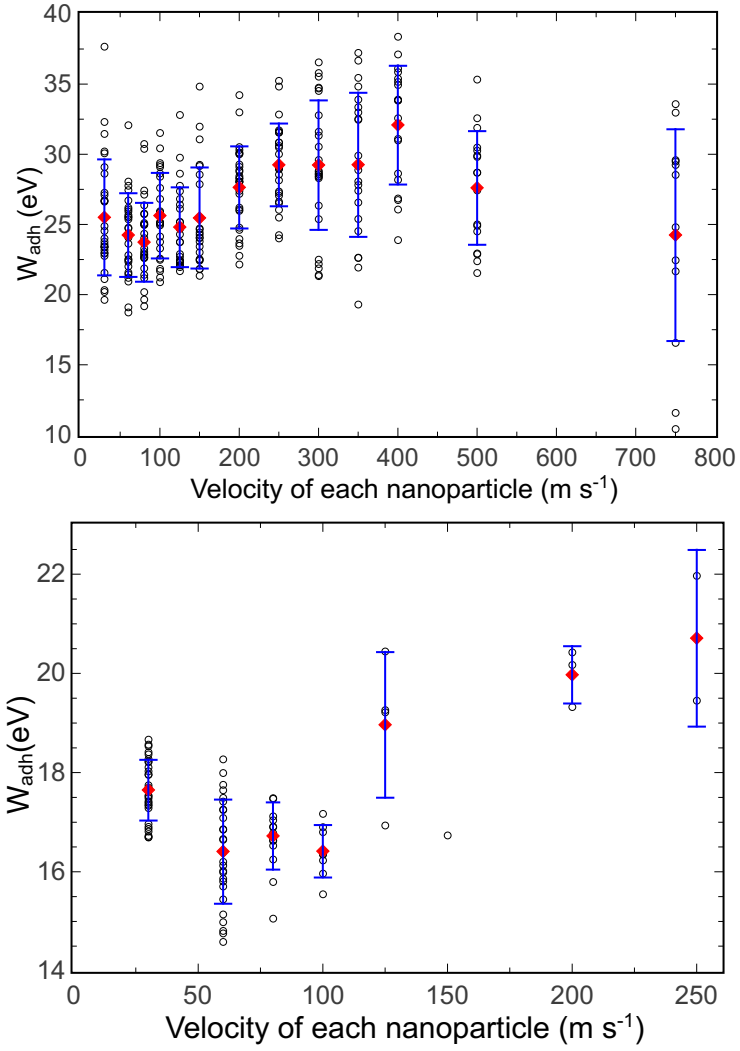

Figure 4.9: The work of adhesion, W_{adh}, calculated for large (a) nonhydroxylated and (b) hydroxylated silica nanoparticles involved in collisions in which the outcomes were particle sticking. Here, we plot W_{adh} for only up to the velocity for which a positive value of W_{adh} was obtained.

bonds, with a partially ionic and covalent character, are formed during a collision event that leads to sticking. There are two aspects of the results that highlight this point. First, the energy scale for W_{adh} is comparable to what would be expected from a calculation of surface energy, γ. Here we focus on the nonhydroxylated nanoparticles, for which $\gamma \approx 0.04$ eV/Å^2. This value is directly related to the number of bonds broken per unit surface area to generate a nanoparticle from bulk a-

SiO_2. If during the collision between two nanoparticles new bonds were formed with coordination similar to bulk a-SiO_2, then one would expect that W_{adh} could be obtained from the surface energy γ and the contact area A. Here we calculate what we call effective contact area A_{eff}, determined from

$$A_{eff} = \frac{W_{adh}}{2\gamma}, \tag{4.12}$$

and compare it to the cross-sectional area of the nanoparticles πa^2, where a is the radius of the nanoparticle. We call this ratio as η, which is effectively a measure of the strength of the interaction between the two nanoparticles. Thus,

$$\eta = \frac{A_{eff}}{\pi a^2}. \tag{4.13}$$

The average values of η obtained for collisions between the nonhydoxylated particles are consistent with the formation of strong bonds. From the average computed values of W_{adh}, we found η = 0.15 and η = 0.13 for the small nonhydroxylated and hydroxylated nanoparticles, respectively, and η = 0.27, η = 0.14 for the large nonhydroxylated and hydroxylated nanoparticles, respectively. However, as can be seen in Fig 7 and 8, the range of values for W_{adh} is broad and for some collisions its value is large indicating strong adhesion. For instance, if we consider the maximum values of W_{adh} for each type of collisions, we obtain η = 0.51, 0.36, 0.38 and 0.17 for the small nonhydroxylated, small hydroxylated, large nonhydroxylated and large hydroxylated nanoparticles collisions respectively. These values of η indicate that in each category of collisions, some collision events resulted in strong adhesion and formation of chemical bonds.

4.6.4 Formation of strong chemical bonds

To demonstrate that strong chemical bonds, rather than weak vdW interactions, are responsible for dissipation and adhesion, we determined the dependence of the attractive force component along the direction of motion of the colliding particles, which we denote by F_y, on the particle separation r. In Fig. 4.10, we show the results for the collision of two small nonhydroxylated

nanoparticles each having an initial speeds of 30 m s^{-1}. For large separations, where vdW interactions play a role, F_y should scale as $F_y \propto r^{-7}$. However, in the log-log plot, we find that in the region r = 22.28 – 23.55 Å, $F_y \propto r^{-27.1}$. This spatial dependency is indicative of non-vdW type higher order multipolar interactions.

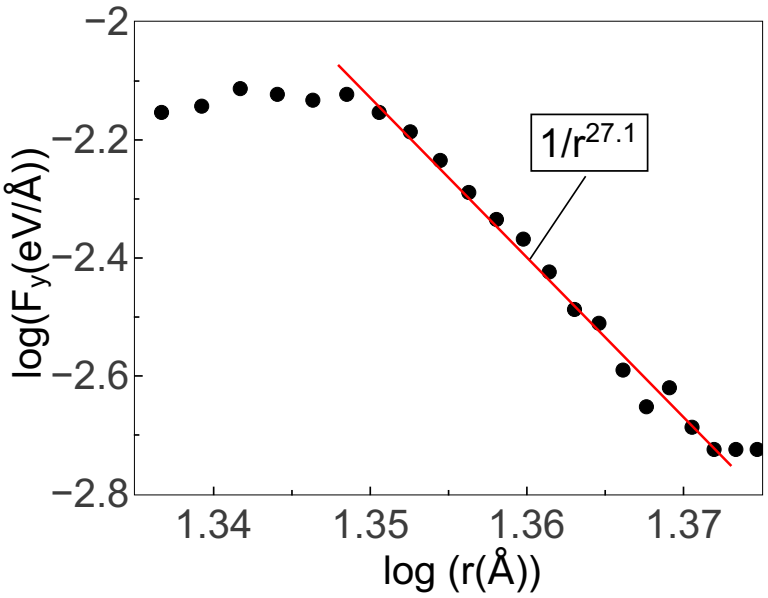

Figure 4.10: Log-log plot of ReaxFF force component in the direction of motion of the colliding particles (F_y) as a function of the distance between their center of masses, based on the data from the collision of two small nonhydroxylated nanoparticles each having an initial velocity of 30 m s^{-1}. The slope of the curve is about -27 in the region r = 22.28 – 23.55 Å ($\log(r)$ = 1.348 – 1.372). At $r < 22$ Å, the nanoparticles touch, and for $r > 25$ Å, F_y is not calculated accurately due to a cutoff distance of 10 Å in the ReaxFF methodology.

To emphasize the above argument, we also simulated a collision between two nonhydroxylated forsterite (Mg_2SiO_4) nanoparticles using the empirical pair-potential developed in [91]. Each of the forsterite grains was made of 128 Mg_2SiO_4 units, had a radius of about 13.5 Å, had identical spatial orientation, and approached the other with a relative speed of 20 m s^{-1}. The corresponding result is shown in Fig. 4.11, where it can be seen that the scaling of F_y with separation r is consistent with those expected for vdW interactions only for separations larger than $\sim$ 10 Å.

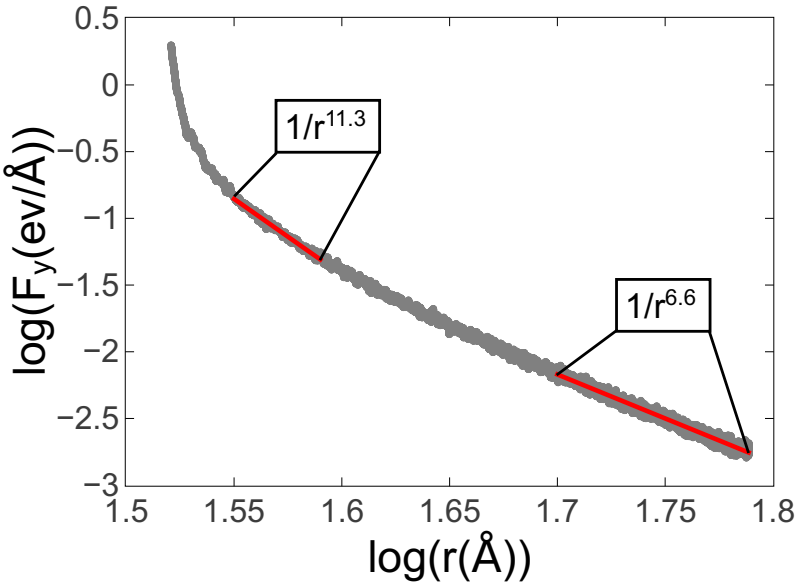

Figure 4.11: Pair-potential force component in the direction of motion of the colliding nanoparticles (F_y), plotted in a log-log scale as a function of inter-particle separation. This plot is based on the data from the collision of two nonhydroxylated nanoparticles, each made up of 896 ions, which approached each other with a relative speed of 20 m s^{-1}. The slope is close to -11 in the near-field and -7 in the far field, indicating the presence of vdW interactions only at longer distances and a much stronger force at closer distances.

When the particle separation becomes less than 10 Å, higher order multipolar interactions rather than vdW interactions become dominant. Since the attractive interactions in the model from [91] are entirely Coulombic and do not contain any covalent bonding terms, as is the case in ionic bonding between point charges, the results indicate that strong ionic bonds form during collisions.

4.6.5 Calculated coefficients of restitution

In Fig. 4.12(a), the COR values for the small nonhydroxylated nanoparticles with bouncing events are shown as a function of the relative collision velocity. For comparison, the COR values for the small hydroxylated nanoparticles are shown in Fig. 4.12(b). No difference between the two systems could be immediately discerned, indicating similar dissipation. The average COR value

in these cases is about 0.4.

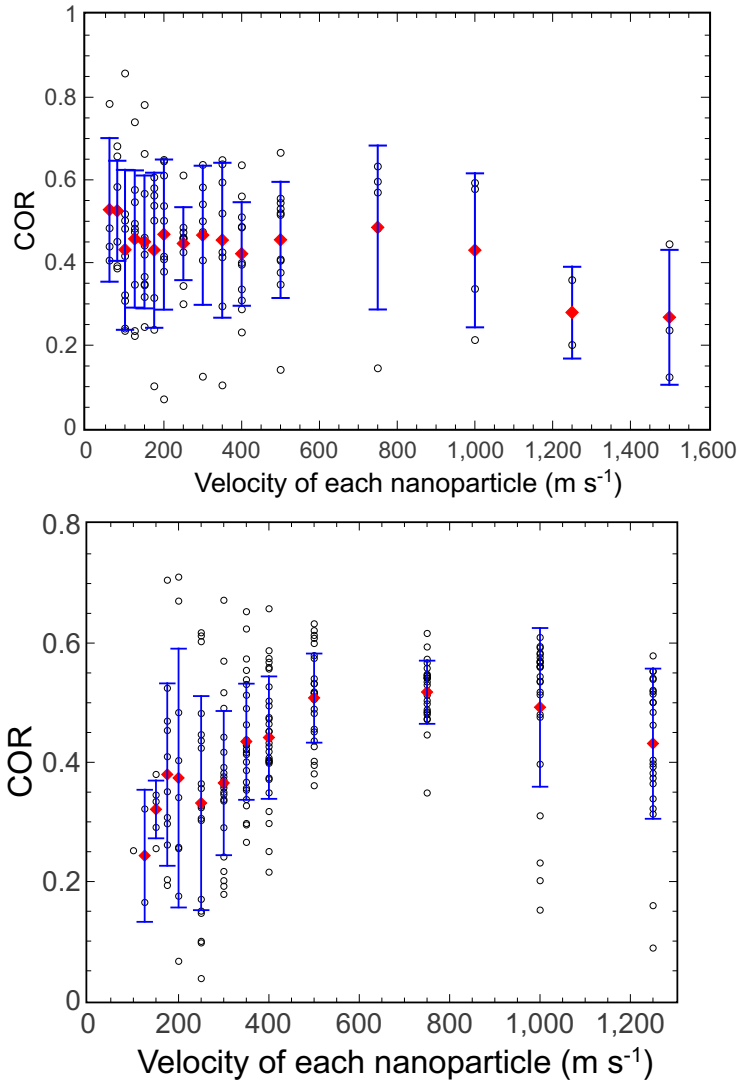

Figure 4.12: Coefficients of restitution (CORs) calculated for collisions of small (a) nonhydroxylated and (b) hydroxylated silica nanoparticles that resulted in bouncing events.

In Fig. 4.13(a) and Fig. 4.13(b), the COR values are plotted for the nonhydroxylated and hydroxylated large nanoparticles, respectively. As with the sticking cases, the behavior is more clearly impacted by hydroxylation of the large particles. Specifically, the average value of COR for the large, nonhydroxylated nanoparticles is ~ 0.4, quite similar to the small nanoparticles. By

contrast, the COR values for the large, hydroxylated particles are ~ 0.6, consistently higher. This indicates less effective dissipation when surfaces are hydroxylated.

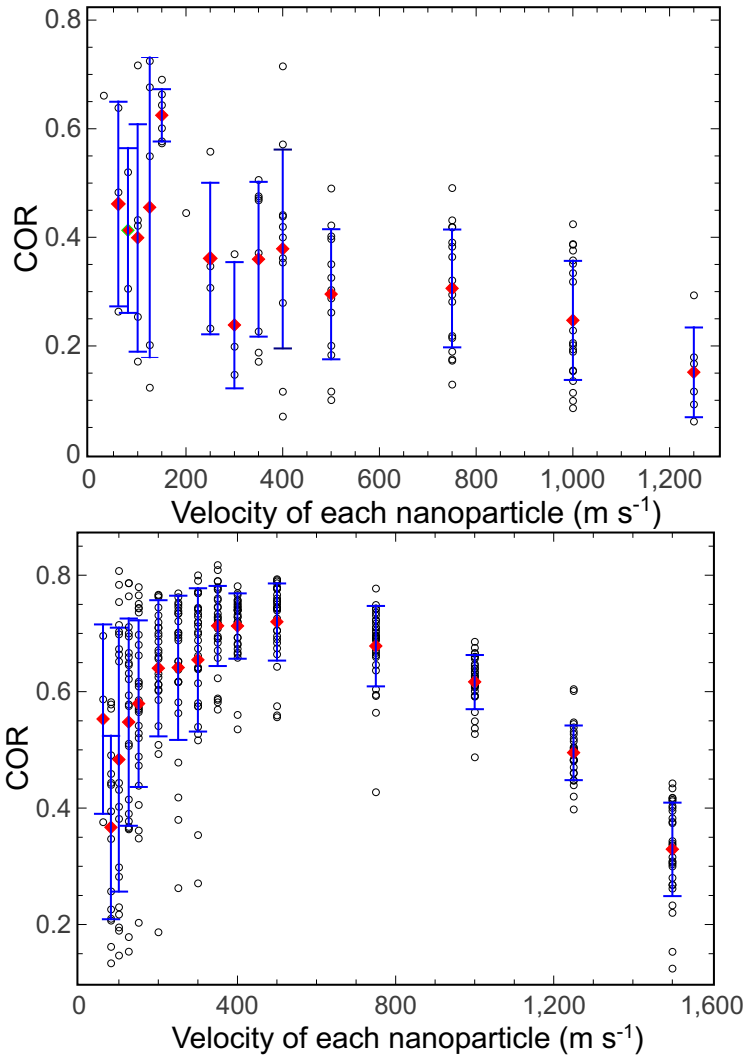

Figure 4.13: Coefficients of restitution (CORs) calculated for collisions of large (a) nonhydroxylated and (b) hydroxylated silica nanoparticles that resulted in bouncing events.

Any attempt to correlate COR and relative velocity requires more calculation. The statistical distribution of COR values appears to overwhelm any trend, and relating it to velocity would require significantly more sampling of the distribution. In case of the large hydroxylated particles, however, a trend could be seen, which is the value of COR is smaller at low collision velocities,

and larger at higher collision velocities. Values of COR ~ 0.8 obtained in some cases approach COR = 1 for perfectly elastic collisions. The trend towards elastic behavior and values of COR approaching 1 correlate with conditions where few sticking events were observed.

4.7 Conclusions

The results presented here demonstrate that during grain collisions, strong chemical forces, rather than simply weak vdW interactions, dominate and can lead to bond formation. Through bond formation, kinetic energy is dissipated effectively, a requisite for particle adhesion or sticking. Consequently, whether two particles will stick after collision will depend on the likelihood of chemical bond formation at the grains' interface, which is highly dependent on the chemical state of the grain surfaces. In case of nonhydroxylated particles, the adhesion is more pronounced. This attributed to the presence of dangling bonds on the surfaces, which helped form strong chemical bonds between the colliding particles. In hydroxylated particles, the dangling bonds are passivated, and consequently the probability of adhesion and also the energy of adhesion gets significantly reduced. Our MD study also reveals that chemical interaction can lead to stronger dissipation than what is expected from theoretical models based on adhesion of elastic spheres.

Our study opens up new avenues for future experimental and numerical studies of proto-planetary grain-grain interactions. In experiment, our results suggest that more attention should be paid towards the chemical state of mineral surfaces in experiments, including how representative the surface chemistry is in comparison to minerals in the space environment. Computationally, our study is an attempt to bring in ideas from materials science to planetary sciences. For example, one can investigate if surface defects that get activated during collisions could aid to effective dissipation. With more works similar to the one pursued here, a greater understanding of the grain-grain collisions, and planetesimal formation could be achieved.

CHAPTER 5: MOLTEN SILICA NANOGRAIN COLLISION

A possible solution to the 'bouncing barrier' to growth of dust grains is proposed through molten grain collision [99]. In protoplanetary disk, due to aerodynamic drag solids spiral inward and enter disk regions which have high temperatures, densities, and pressures. High partial pressures of rock vapor can suppress solid evaporation, thus dust grains can remain in partially molten state, and collision can take place and sticking can occur at higher velocities than predicted by current theories. Also, it has been found that molten chondrules, the millimeter-size, igneous spherules that dominate the textures of primitive meteorites, can survive collisions at velocities as high as a few hundred meters per second [100]. Motivated by the above arguments, we carry out molecular dynamics simulation of collisions of molten silica nanograin.

5.1 Preparation of molten particles

We made use of our previous work where we melted silica using a ReaxFF [3] potential. As mentioned in Chapter 4, we melted it towards 4000 K. We gradually cooled the same melt, and obtained structures at the desired temperatures. Here we consider collisions only between the large nonhydroxylated nanoparticles, which had 894 Si ions and 1788 oxygen ions.

5.1.1 Nanoparticle Melting Temperature

Melting temperature of nanoparticles can be determined by calculating various dynamic and structural properties as a function of time, e.g., from energy-temperature plot [101, 102], temperature dependence of Lindemann index [101]. Here we determine the melting temperature of the large nonhydroxylated nanoparticle for the ReaxFF potential [3] observing potential energy as a function of temperature (Fig. 5.1). At melting temperature, the potential energy plot exhibits a change of derivative [101]. Since the nanoparticle is amorphous, the transition temperature is

broad, and is around 1800 K in Fig. 5.1. Though melting temperature of nanoparticle differs from that of the bulk, we nevertheless found out the mean square displacement for bulk a-SiO_2 for T = 1500 K. Fig. 5.2 and 5.3 show mean square displacement of oxygen and silicon ions respectively in silica melt at T = 1500 K.

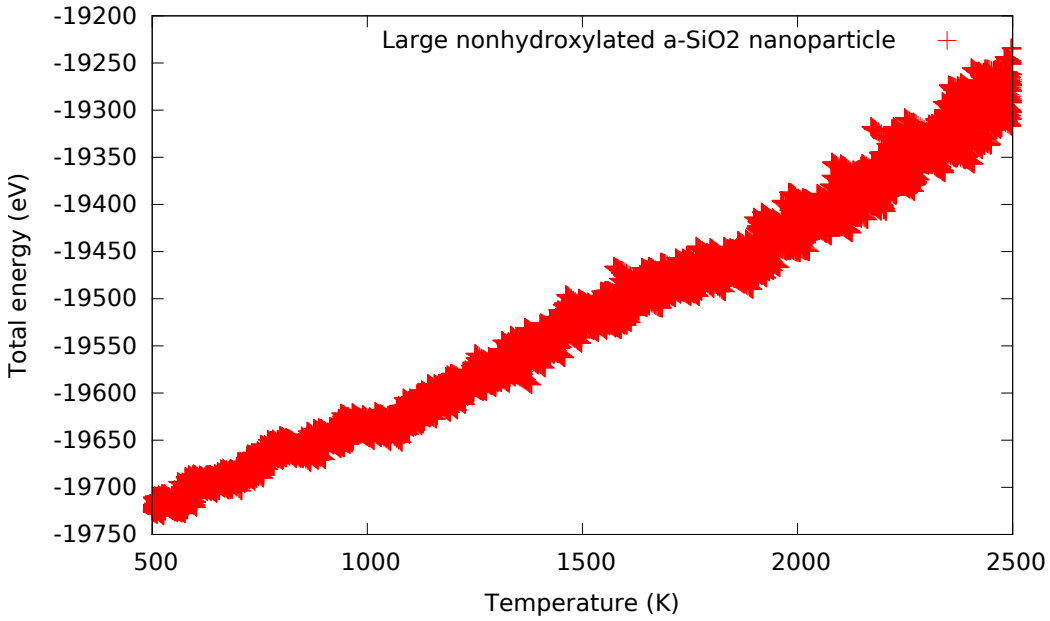

Figure 5.1: Potential energy of amorphous silica nanoparticle as a function of temperature.

5.2 Simulation of collisions

Since in our previous study (Chapter 4) the sticking probability was somewhat higher at lower velocities, here we pick three high velocities to observe the effect of molten state more clearly. We simulated collision at 3 relative velocities, in particular for 400 m s^{-1}, 800 $^{-1}$ and 1500 $^{-1}$. For collision at each velocity, we carried out 30 collisions and observed the outcome. We calculated sticking probability in the same way we did in our previous study in Chapter 4.

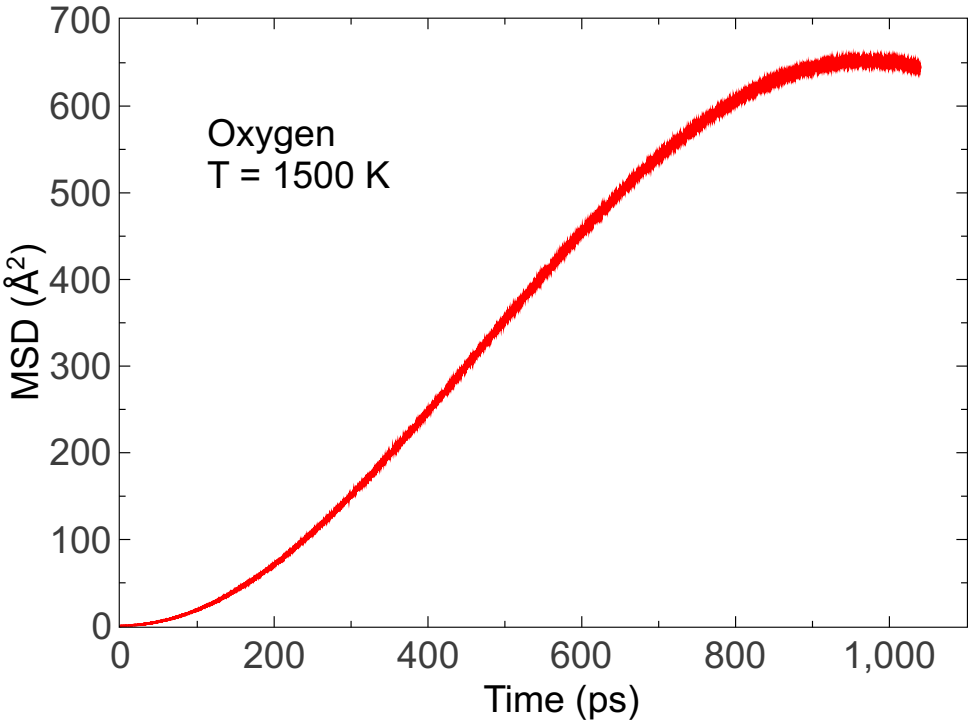

Figure 5.2: Mean square displacement of oxygen inside silica at T = 1500 K.

5.3 Results

5.3.1 Sticking Probability

For each temperatures, sticking probability was calculated for relative speeds 400 m s^{-1}, 800 m s^{-1} and 1500 m s^{-1}. The results are shown in Fig. 5.4. The plots reveal that except at some odd cases, sticking probability is higher at higher temperatures. The trend can be seen more clearly in Fig. 5.5.

5.3.2 Bulk modulus calculation

Bulk modulus for amorphous silica was calculated corresponding to ReaxFF potential at three different temperatures. This is shown in Fig. 5.6. At ambient temperature, amorphous silica

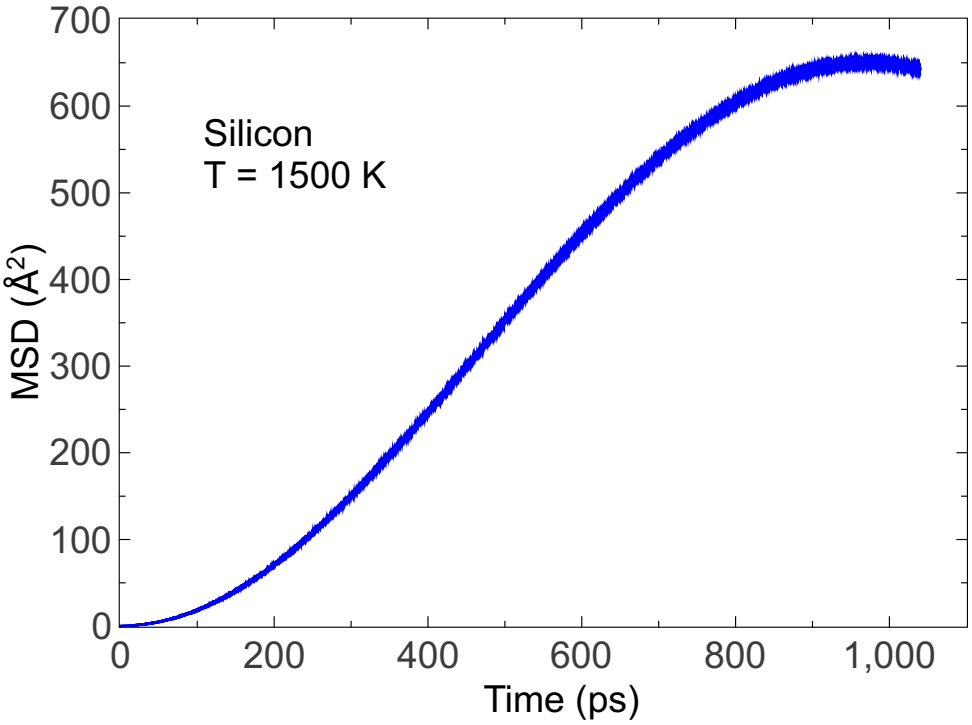

Figure 5.3: Mean square displacement of silicon inside silica at T = 1500 K.

has a bulk modulus of 37.5 GPa [103], and from Fig. 5.6 we can see that ReaxFF model fails to predict this value of bulk modulus. However, at 823 K and at 1273 K, bulk modulus of amorphous silica is 42.2 GPa and 43.2 GPa respectively [104], and our calculation is relatively close to the experimental results.

5.3.3 Shear viscosity calculation

Viscosity can be calculated from equilibrium molecular dynamics using the following Green-Kubo relation where pressure tensor $\langle A_{\alpha\beta}(t)A_{\alpha\beta}(0)\rangle$ autocorrelation function is integrated over correlation time.

$$\eta = \frac{1}{k_B T V}\int_0^\infty dt\,\langle A_{\alpha\beta}(t)A_{\alpha\beta}(0)\rangle\,. \tag{5.1}$$

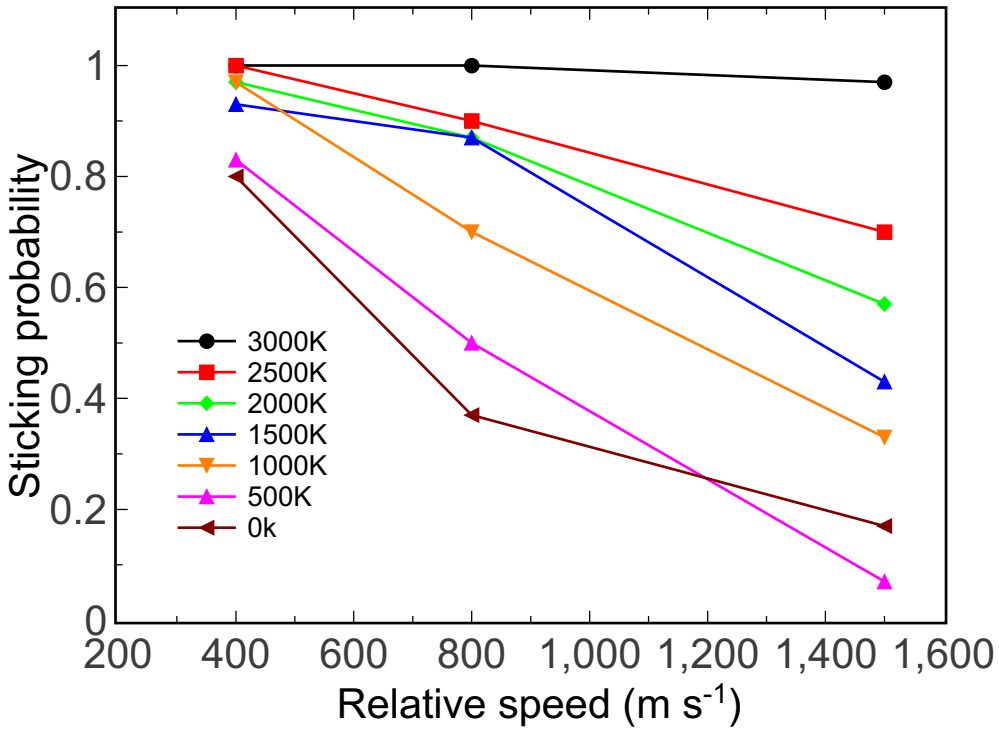

Figure 5.4: Sticking probability of silica nanograins for different temperatures over a range of collision velocity.

Here, V is the volume of the system, k_B is Boltzmann constant, T is the system temperature, and $A_{\alpha\beta}$ is the off-diagonal elements of pressure tensor given by:

$$A_{\alpha\beta} = \sum_{i-1}^{N} m_i \mathbf{v}_i^{\alpha} \mathbf{v}_i^{\beta} + \sum_{i-1}^{N} \sum_{j>1}^{N} F_{ij}^{\alpha} r_{ij}^{\beta}, \quad \alpha \neq \beta, \tag{5.2}$$

where F_{ij}^{α} is the α component of the force between ions i and j.

Theoretically, after a long time the pressure tensor autocorrelation function $\langle A_{\alpha\beta}(t) A_{\alpha\beta}(0) \rangle$ should decay to zero, and consequently the integral in Eq. 5.1 or in other words viscosity should approach a plateau after initial rise. However, due to noise accumulation, the integral does not always converge and instead shows large fluctuations at long times. As as result, one needs to take the average of several trajectories [105].

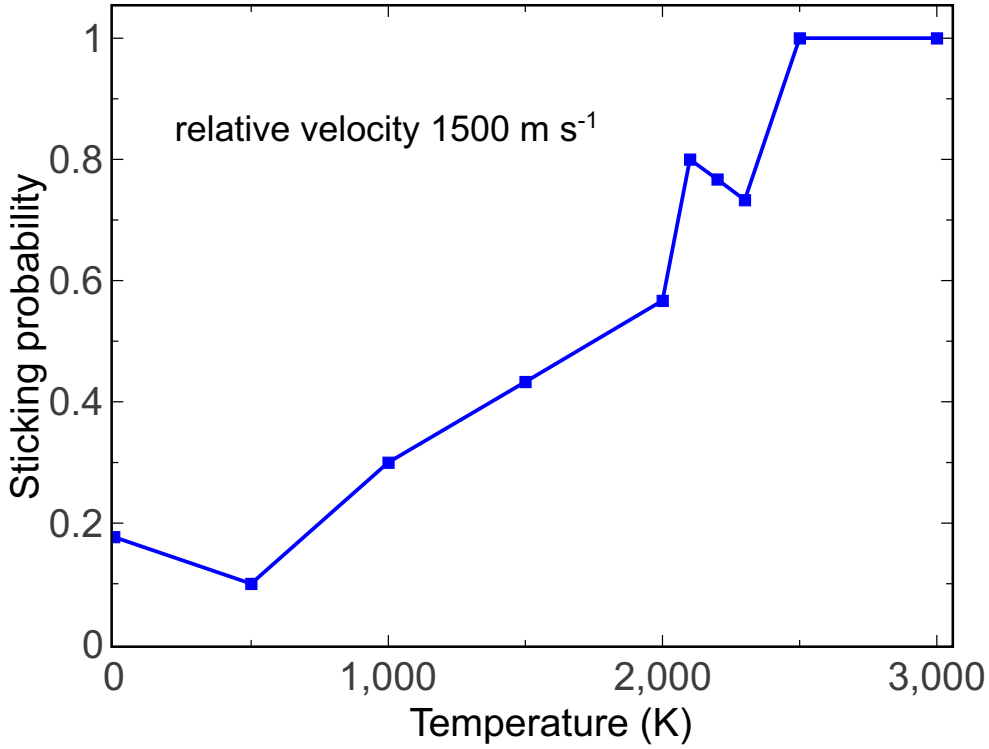

Figure 5.5: Sticking probability of silica nanograins at different temperatures for a particular collision relative velocity.

We used the inbuilt procedure in LAMMPS [69] to calculate autocorrelation functions, and carry out the integration in Eq. 5.1 using trapezoidal rule and determine the viscosity for each temperatures as a function of correlation time t. The calculations for T = 1500 K, 2000 K, 3000 K and 4000 K are shown in Figs. 5.7 - 5.10. In determining viscosity, we followed a procedure similar to the one outlined in [105], however, unlike [105] where the equilibrium molecular dynamics was done in NVT, we carried out MD using NVE ensembles as has been done in [106]. The MD timestep was taken to be 0.2 fs to ensure energy conservation.

First, we equilibrated a system at a target temperature, e.g., 3000 K using NVT ensemble. The ensemble average of temperature from the NVT run came out to be almost exactly the target temperature. We then took the system, and perturbed the system by providing random motion to the

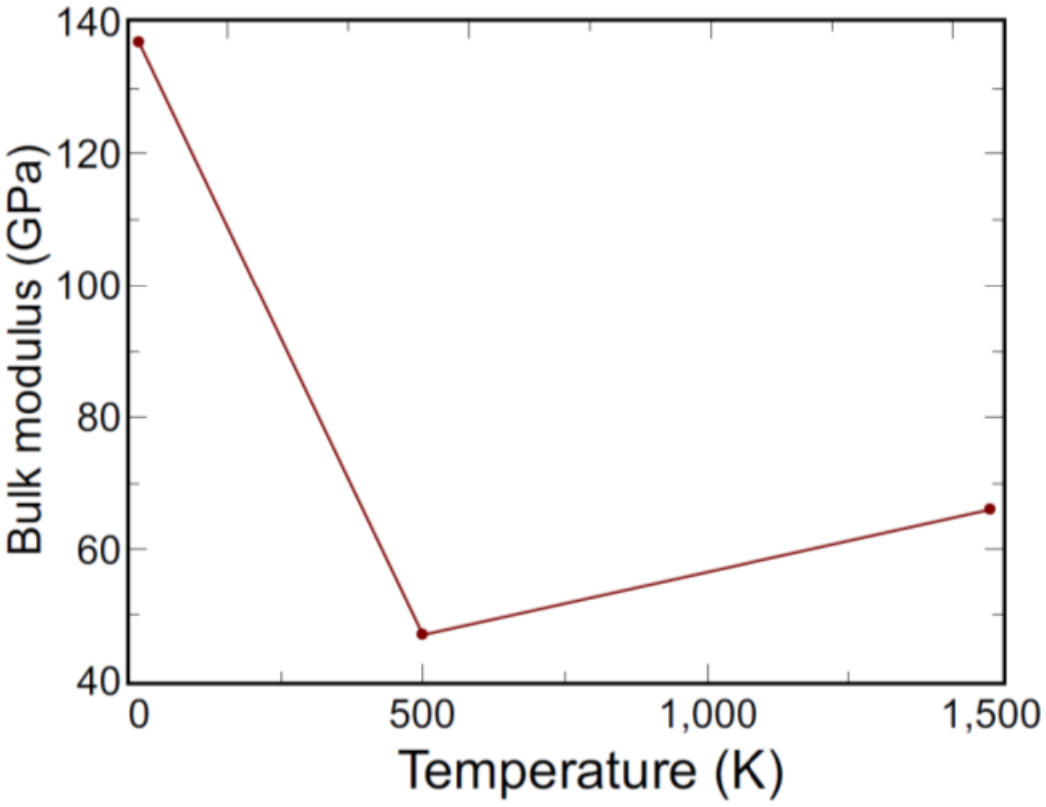

Figure 5.6: Bulk modulus of amorphous silica using Kulkarni ReaxFF force field for different temperatures.

atoms corresponding to the same target temperature. This kept the total energy of the system same as before, however, the velocity space got new configuration. By making use of random number, we generated 30 such configurations all of which had the same amount of total energy and the same amount of thermal energy but differed in velocity distribution among the atoms. We carried out NVE molecular dynamics with all 30 systems. Since redistribution of velocity in the systems as described above did not perturb the systems from their previous equilibrium state significantly, we recorded the autocorrelation function for the nondiagonal element of pressure tensor from the start of NVE run.

After the NVE runs, we collected the data from LAMMPS, and carried out running inte-

gration to obtain viscosity as a function of correlation time. This did not yield positive viscosity for all the NVE runs. We retained only those runs which produced positive values of viscosity, and took an average of them. In Figs. 5.7 - 5.10, the average is shown along with error bars. The averaging was done taking averages of the autocorrelation functions for P_{xy}, P_{xz} and P_{yz}. As can be seen from the figures, the total correlation time was 600 ps for the temperatures T = 1500, 2000 K and 3000 K, and was 300 ps for T = 4000 K.

It can be seen from Fig. 5.7 and Fig. 5.8 that the average did not approach any plateau for the cases T = 1500 K and T = 2000 K. As a result, no extrapolation could be done to determine viscosity. This indicates longer correlation time is required to determine viscosity at this temperature. Indeed, Horbach and Kob [106] reported that because of the long relaxation times at T = 2900 K and T = 2750 K, they were not able to carry out 18 runs for averaging as they did for higher temperatures, and consequently could not determine viscosity at these temperatures.

The viscosity condition to avoid splashing upon collision is given by [107, 108]

$$\eta \leq 6 \times 10^7 \left(\frac{a}{\text{cm}}\right) \left(\frac{\nu}{\text{cm s}^{-1}}\right)^{-1/5}. \tag{5.3}$$

Here, η is given in Poise. Taking a = 20 Å and ν = 400 m s^{-1}, we find value of viscosity has to be lower than 1.44 Poise. However, we find sticking is taking place when viscosity is much higher than that. For example, at T = 3000 K, the viscosity is about 15 Poise, and we find sticking probability reaches almost 1.

5.4 Conclusion

Results from the simulation of collisions of molten silica nanograins carried out here corroborates the assertion that molten silica nanograins are more sticky than in solid phase. We aim to provide a sound theoretical understanding of the observed result. For example, Eq. 5.3 does not have any reference to the temperature. Also, we need to investigate how the temperature depen-

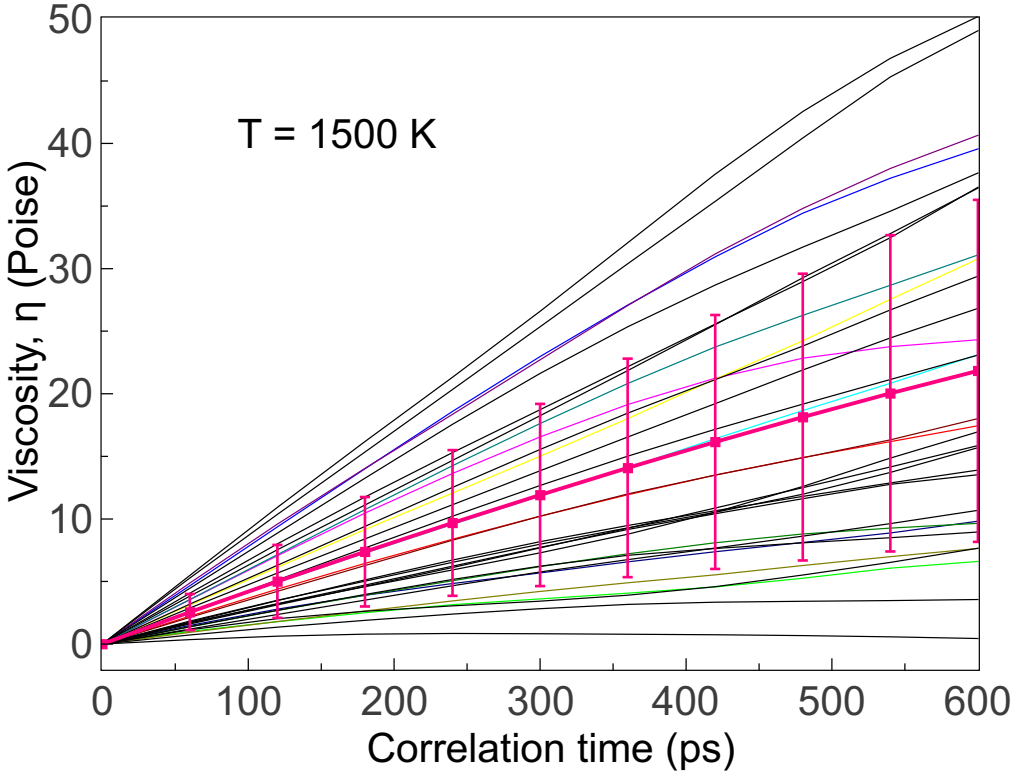

Figure 5.7: Shear viscosity of molten silica at T = 1500 K.

dence of the elastic properties come into play in determining the outcome of molten silica grain collisions.

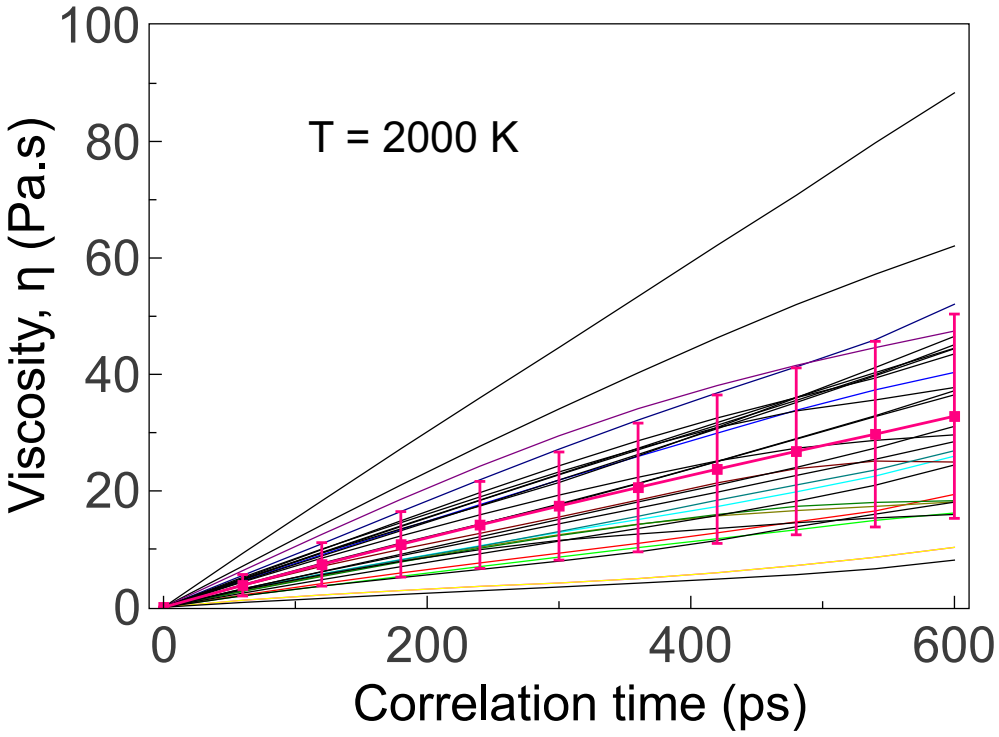

Figure 5.8: Shear viscosity of molten silica at T = 2000 K.

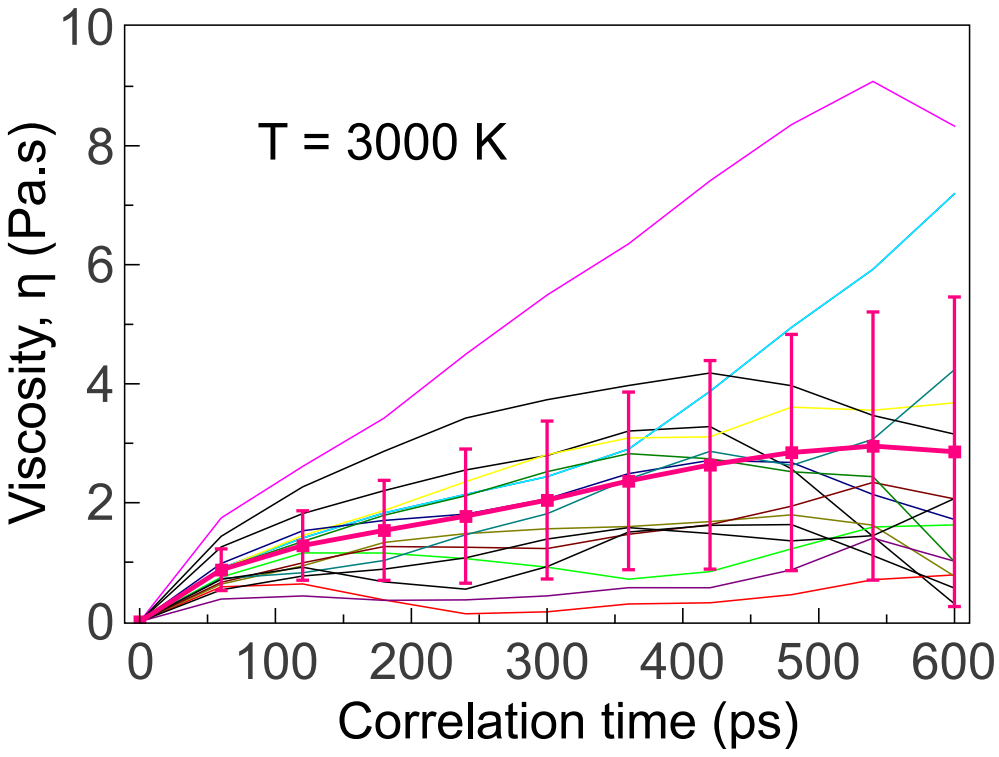

Figure 5.9: Shear viscosity of molten silica at T = 3000 K.

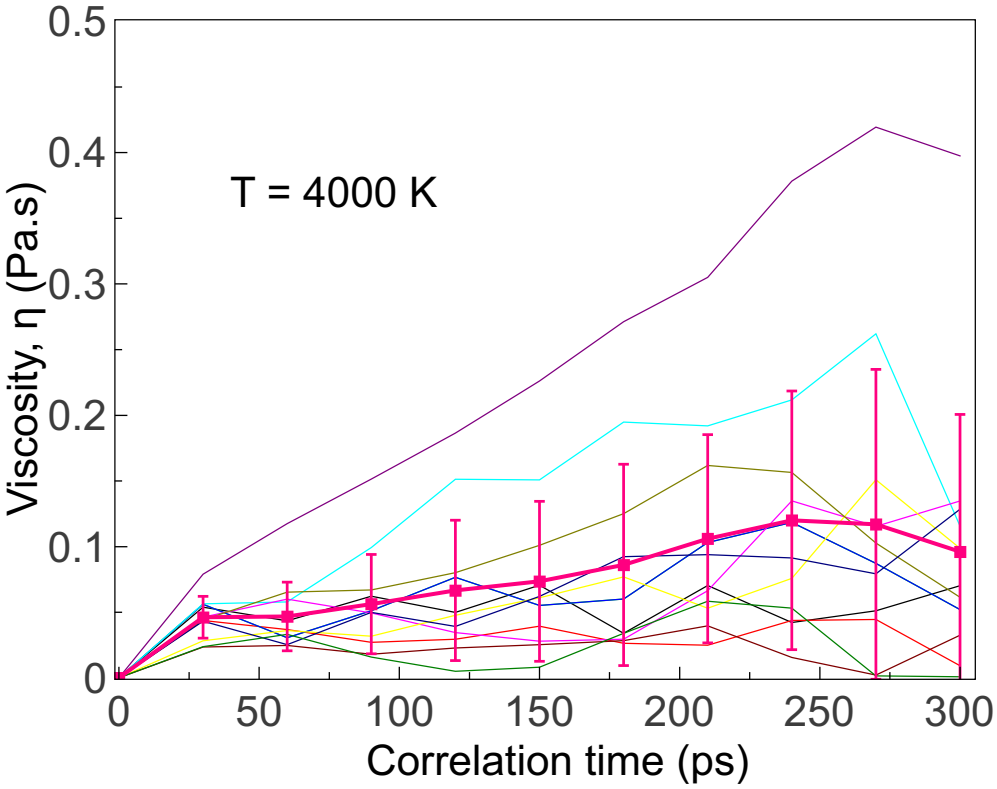

Figure 5.10: Shear viscosity of molten silica at T = 4000 K.

CHAPTER 6: DEVELOPMENT OF ReaxFF POTENTIAL FOR FAYALITE

In our brief overview of ReaxFF potential in Chapter 2, we mentioned it is a many-body reactive empirical force field that can model changing chemical environment of a system [36]. We wanted to extend the range of materials that could be simulated with ReaxFF model including non-stoichiometric minerals. The molecular dynamics study of radiation damage described in olivine and orthopyroxene Chapter 3 was limited by the fact that due to use of a pair potential, charges on the atoms remain fixed and no chemistry took place. Point defects lead to only local deviations from stoichiometry, while maintaining overall stoichiometry of either olivine or orthopyroxene. Thus, reduction of the mineral surface, and the gradual formation of metallic Fe clusters, cannot be directly explored by the methodology through atomic-scale simulation using a pair potential.

To go beyond this level of calculation, we put our effort to develop a reactive potential for fayalite (Fe_2SiO_4), or in other words the three component Fe-Si-O system. This approach uses variable charges, and allows for the formation of elemental metal and deviations from perfect stoichiometry. Hence, the evolution of the olivine and orthopyroxene systems can be determined as oxygen is lost due to heating or preferential sputtering due to radiation damage. Such an study could reveal the relative roles of vapor deposition and radiation damage (e.g. via preferential sputtering of oxygen) in the production of $npFe^0$, and help explain the observed differences in space weathered samples, e.g., between those collected from the moon and the asteroid Itokawa.

With the above goal in mind, we set out for developing a ReaxFF potential for fayalite. One such potential would also enable us to explore role of chemistry in the collisions of olivine similar to the study presented in Chapter 4. However, our attempt had not been completely successful for reasons that will elaborated in the subsequent sections. We identified fundamental limitations of the ReaxFF formulation, which we report here in the hope that the discussion might be useful for

other researchers who may attempt to generate new ReaxFF force field.

6.1 Approach to develop ReaxFF potential for Fe_2SiO_4

In developing ReaxFF models for Fe_2SiO_4, we were guided by two factors. First, fayalite can be regarded as weakly interacting chemical systems, or solid mixtures of SiO_2 and FeO:

$$2FeO + SiO_2 \rightarrow Fe_2SiO_4 \tag{6.1}$$

Second, ReaxFF potentials are expected to be transferable across different material systems. Thus, it was expected that if existing ReaxFF potentials for Si-O [3] and Fe-O [109] were combined along with introduction of Fe-Si interaction, then the resultant model should be able to describe the three-component mineral reasonably well. Bond-order potentials are expected to take into account the environment while determining the interaction between two atoms. Thus, ideally Fe and Si should not have any strong interaction inside fayalite, and ReaxFF should be able to predict that. However, ReaxFF model turned out to be unable to do so, and we scrutinize its limitations later.

We organize this chapter in the following way. We describe the fitting obtained for Fe-Si first, then show how the combination of Fe-Si, Fe-O and Si-O models failed to generate a model that could stabilize fayalite. Then we describe our efforts for improving Si-O model. We present the mathematical formulation of ReaxFF in Appendix A. In this chapter, we describe the training set, steps followed for fit, and the validation process.

6.2 Training Sets

In each cases, the target energies were calculated using density functional theoretic (DFT) calculations which were adjusted to experimental values whenever available. If absolute value could not be determined due to lack of experimental data, we targeted energy difference of struc-

tures rather than absolute energy of those structures. The DFT calculations were done using PBE pseudopotentials [110]. Convergence was tested for k-space. The crystal structures were obtained as crystallographic information file (cif) from the RRUFF database [111]. The original source of the cif files are previously published results on the corresponding crystal structures, and here we cite the source in every case. We carried out the calculations using the package VASP. The structure files for VASP were generated using a open-source tool cif2cell [112].

6.3 Fitting Procedure

After obtaining the training set through DFT calculations, we fit a set of selected parameters appearing in the energy terms to obtain the target energies. The fitting is done using the single-parameter search optimization technique described in [113].

6.4 ReaxFF Model for Fe-Si interaction

The target energies included that of Fe-Si dimer, Si-Fe-Si and Fe-Si-Fe trimers, and crystal naquite. First Fe-Si dimer energies were calculated in DFT. We kept a particular parameter fixed at a set of values and carried out the fit. The trimers were then included in the training set, and each of the previous fits were continued. Finally, naquite was included in the training set. Naquite is cubic, and its symmetry group is P 2_1 3. The naquite structure corresponded to that described in [114]. Self-consistent calculations were performed using a $7 \times 7 \times 7$ mesh according to the Monkhorst-Pack scheme. The cutoff energy was taken to be 400 eV. The GGA cohesive energies are overestimated by 2.88 eV/atom for Fe and 0.16 eV/atom for Si. The heat of formation ΔH of iron silicide series is evaluated with respect to the ground state of ferromagnetic Fe bcc, and nonmagnetic Si diamond energies. Our DFT calculated energies were in very close agreement with the DFT energies reported in [115].

6.4.1 Results from Fe–Si fit

The fits to the target energies came out to be good. In Fig. 6.1, we show a set of fits to the Fe–Si dimers. Fig. 6.2 shows the fits to the trimers. Finally, Fig. 6.3 shows the naquite fits.

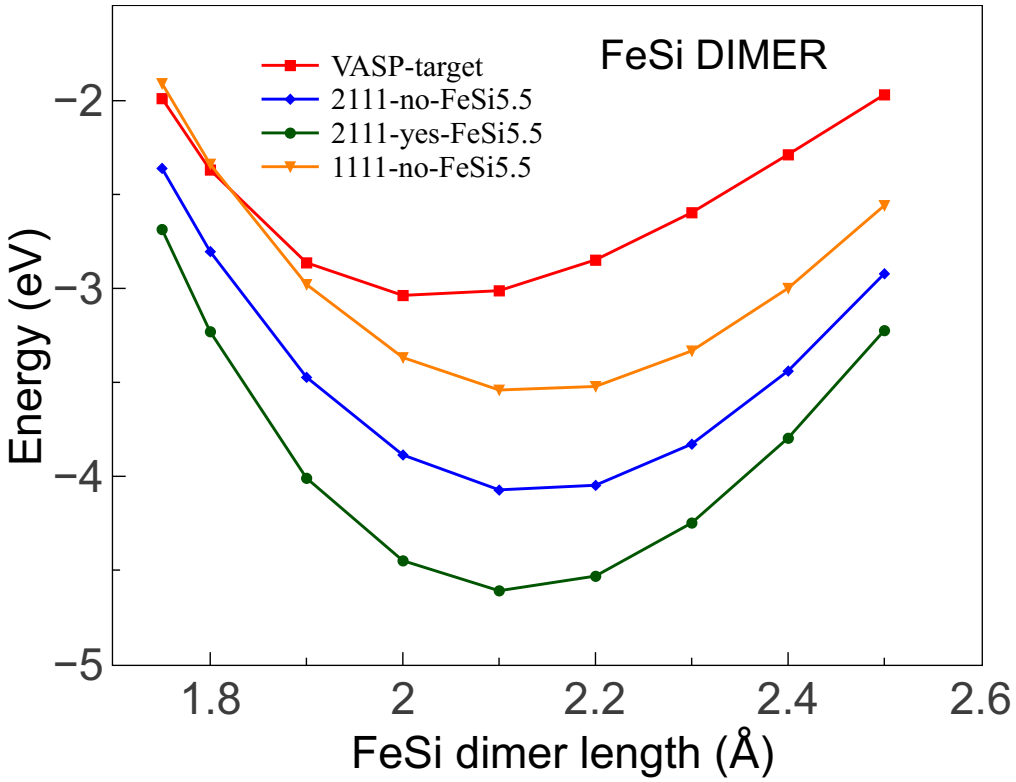

Figure 6.1: ReaxFF fit to FeSi dimer (FeSi).

6.5 Combining Fe-Si Fit with Existing Si-O Fit

We combined the newly obtained Fe–Si model with an existing Si–O model, and included fayalite in the training set. Again, the fit came out to be reasonable (Fig. 6.4). However, when we carried out NPT simulation with fayalite, the model was unable to stabilize fayalite structure, and there was a phase transformation as found from visual inspection (Fig. 6.5).

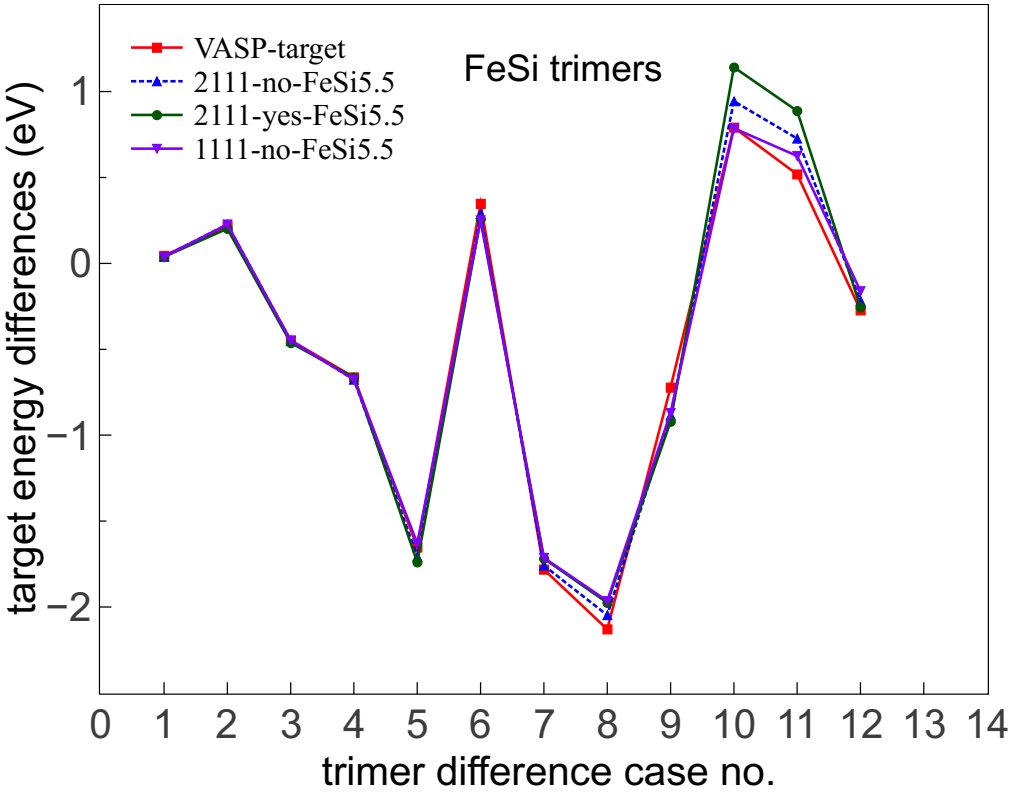

Figure 6.2: ReaxFF fit to FeSi trimer (Fe-Si-Fe and Si-Fe-Si).

6.6 Assesment of Existing ReaxFF Models for Silica Elastic Property

Having found our proposition that amalgamation of various ReaxFF model should be able to predict fayalite behavior reasonably does not work, we set out to examine the silica ReaxFF model that we used. We calculated the Si-O dimer energies, energy vs volume curve for four silica polymorphs namely α-quartz, α-cristobalite, β-tridymite and coesite. Along with Kulkarni model, in each of the above case we calculated the energies using two other silica models which we label here as Fogarty [87] and Pitman [116]. For all the models, we notice discontinuity. It should be mentioned here during energy calculation in DFT, we did not relax the structure, thus the DFT energy curves we were comparing were obtained from unrelaxed crystal structures.

The result for dimer energy is shown in Fig. 6.6. The energy vs volume plots for α-

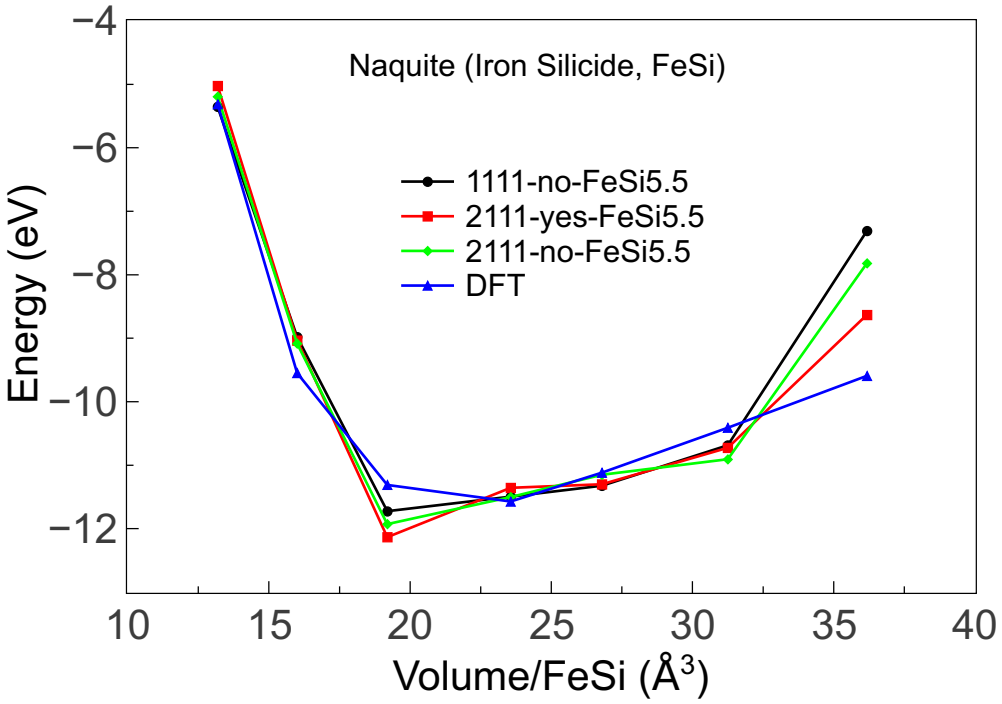

Figure 6.3: ReaxFF fit to Naquite (FeSi).

quartz, α-cristobalite and β-tridymite are shown in Figs. 6.7, 6.8 and 6.9 respectively. We also calculated the equation of state curve for α-quartz and amorphous silica and determined their bulk modulus using Kulkarni model. To do so, we allowed the structures to relax at T = 0 K at different external applied pressure. In case of α-quartz, we also determined if the structures remained indeed α-quartz, or changed to some other phase. Using Birch-Murnaghan equation of state, we then determined the bulk modulus. We found that Kulkarni cannot reproduce good elastic properties. The results for α-quartz and amorphous silica are shown in Figs. 6.10 and 6.11. The bulk modulus for α-quartz came out to be 166 GPa, and for amorphous silica the value was about 130 GPa. This is far from the experimental values. Bulk moduli of quartz and amorphous silica at ambient temperature and pressure are 37.5 GPa [103] and 36 GPa [104] respectively.

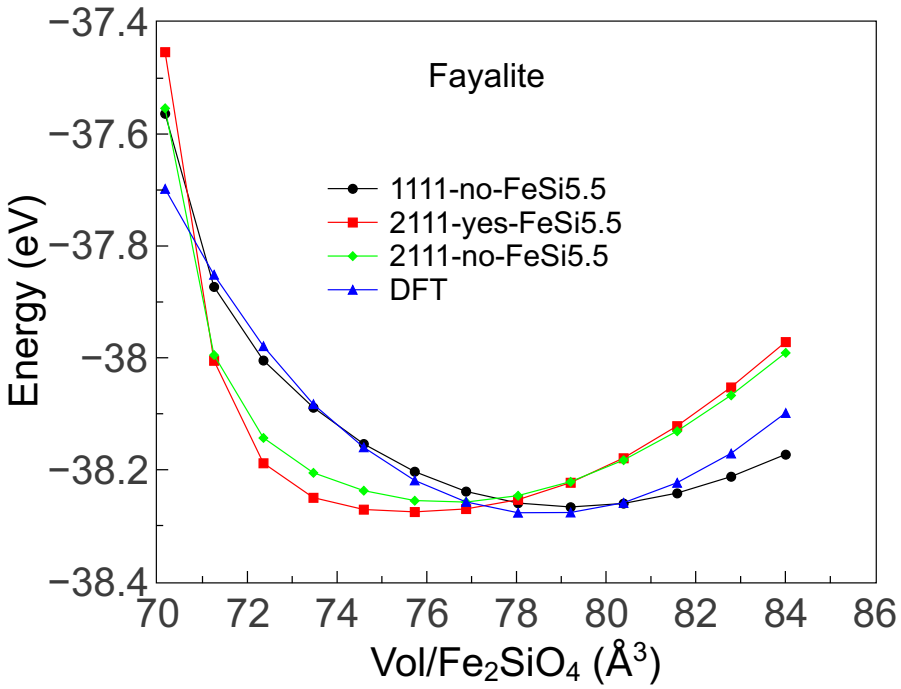

Figure 6.4: ReaxFF fit to fayalite.

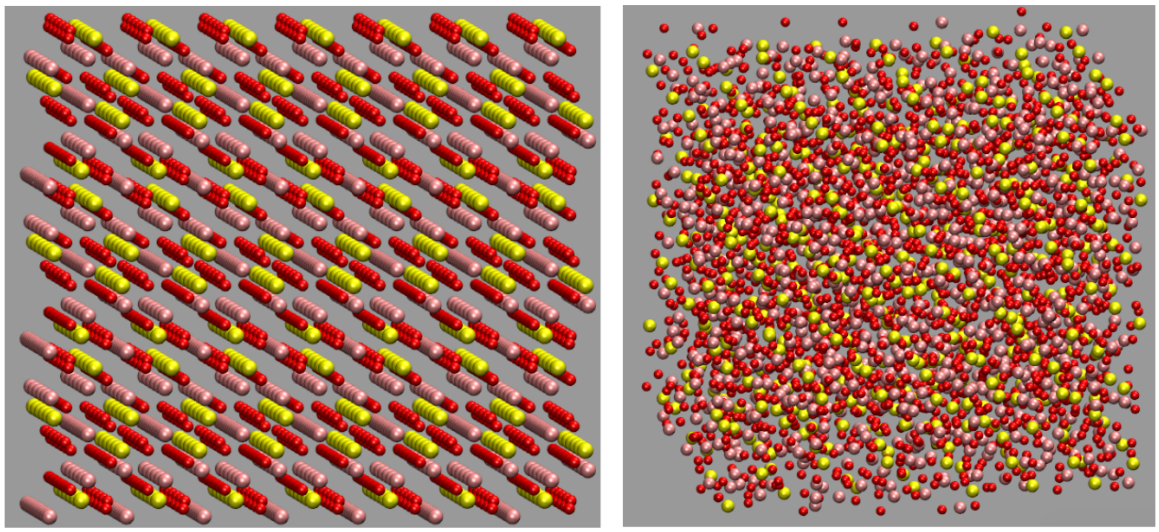

Figure 6.5: The ReaxFF model for fayalite cannot stabilize its structure.

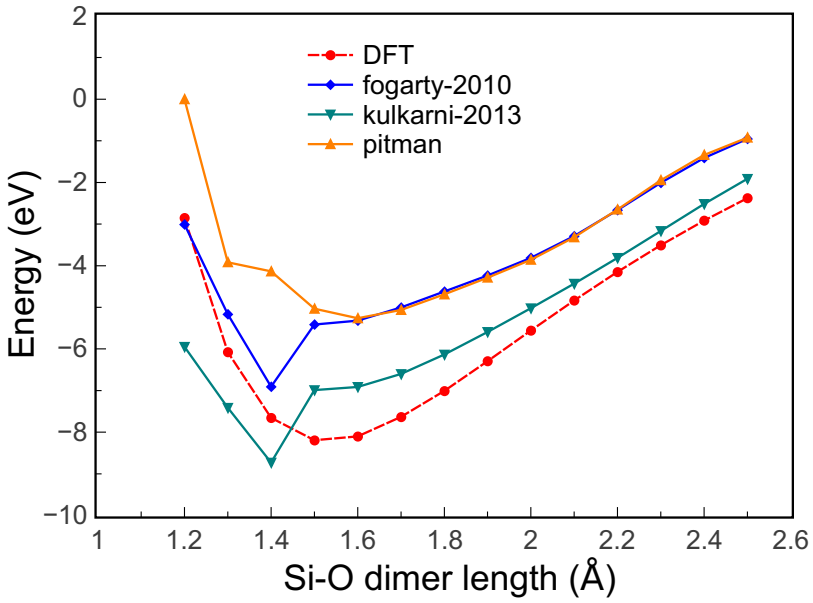

Figure 6.6: Si-O bond energy as a function of bond length.

6.7 Development of a New ReaxFF Si-O Model

The Kulkarni model for Si-O [3] is rather limited in its prediction of the elastic properties of silica. We thus made attempt to improve the model. The training set included Si-O dimer energy, Si-O-Si and O-Si-O trimer energy, and cohesive energies of several polymorphs, namely α-quartz, α-cristobalite, β-tridymite and coesite.

In the first step, we only fitted Si-O dimer energies. We kept the value of R_0 fixed at some selected values, and varied 14 other parameters. Later we included the trimer energies in the fit. We then included the angle parameters. After the above two cycles, we included the bulk structures, and added few more parameters in the fitting. To understand the training set, it is pertinent to have ideas about the structures of silica polymorphs. They are described in Appendix B.

We calculate α-quartz energies for the equilibrium structure [117] and for structures which are expanded and compressed in steps of 2% up to 12%. Thus we calculate energies for 13 struc-

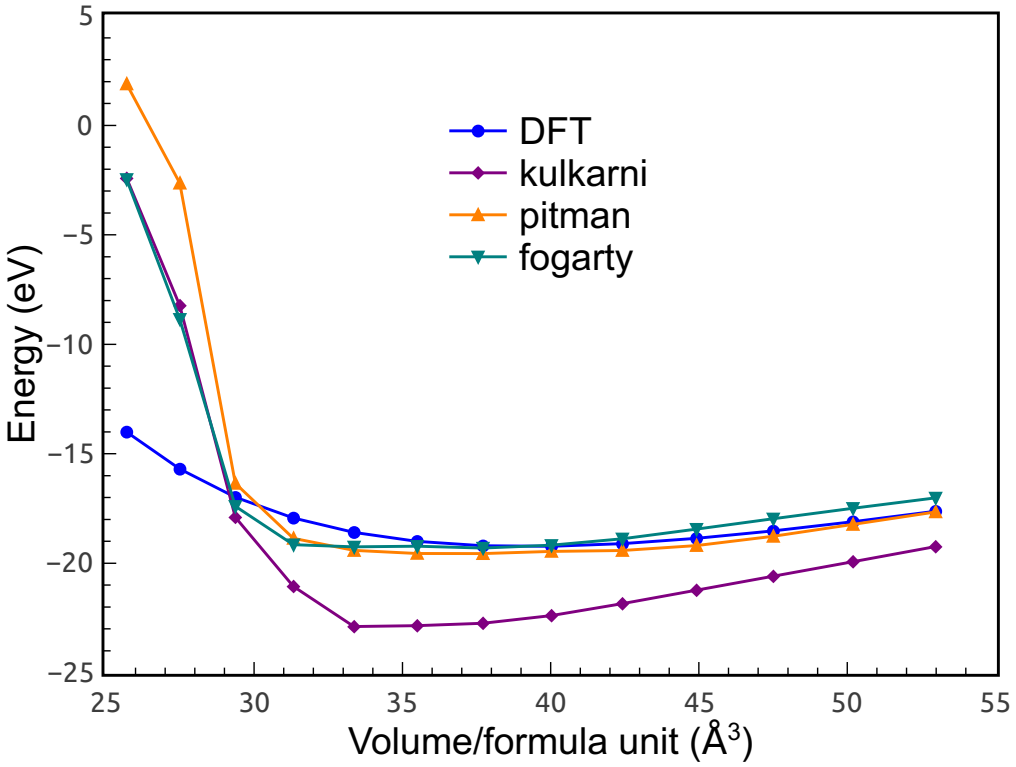

Figure 6.7: Cohesive energy of α-quartz.

tures. Comparison of DFT cohesive energy to experimental cohesive energy mandated a shift of +4.7 eV. This energy shift was applied to all subsequent calculations of energies of other silica polymorphs.

We took expanded and contracted volume upto 12% in steps of 2% on both ranges. We calculated their ground state energy by keeping the volume fixed while allowing the lattice parameters vary and internal coordinates to relax. At first, we determined the cohesive energy of quartz using DFT calculations where we kept the volume fixed but allowed the lattice constants to vary and also the internal coordinates to vary. We adjusted the DFT curve to experimental cohesive energy, which is -19.3 eV, and found an offset of +4.47 eV. We applied this shift on the subsequent DFT calculations of cohesive energies of other polymorphs, namely of α-cristobalite, β-tridymite, and coesite. We varied the internal parameters of α-quartz, α-cristobalite and β-tridymite and cal-

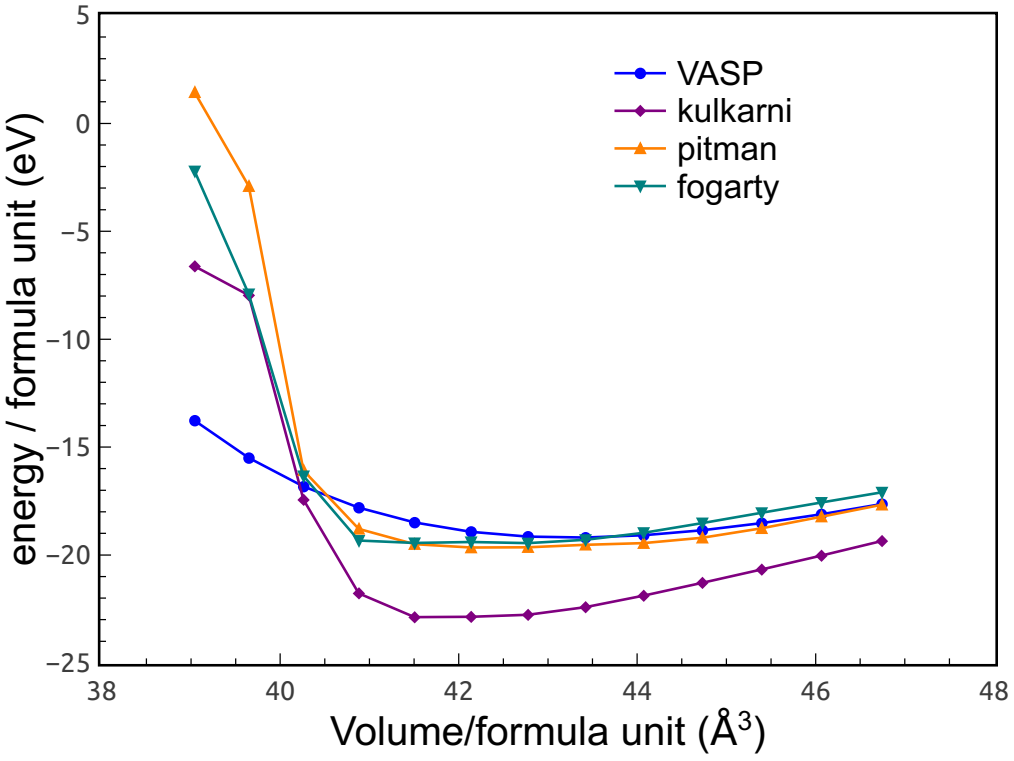

Figure 6.8: Cohesive energy of α-cristobalite.

culated their energies using DFT calculations. We started fitting with Pitman potential since it gave better cohesive energy.

6.7.1 Results from Si-O fit

We obtained good fit with energies, however, the model did not stabilize α-quartz when we carried out dynamics. Some of these results are shown in Figs. 6.12 (Si-O dimer), 6.13 (α-quartz), 6.14 (α-cristobalite) and 6.15 (β-tridymite). Our fit produced good agreement with other target energies, e.g., energy variation with internal coordinates in some of the above polymorphs, trimer energy differences, etc.

However, when it came to dynamics, our fit did not perform well. For NPT runs, it could not stablize α-quartz and there was phase transformation. We examined this by first determining

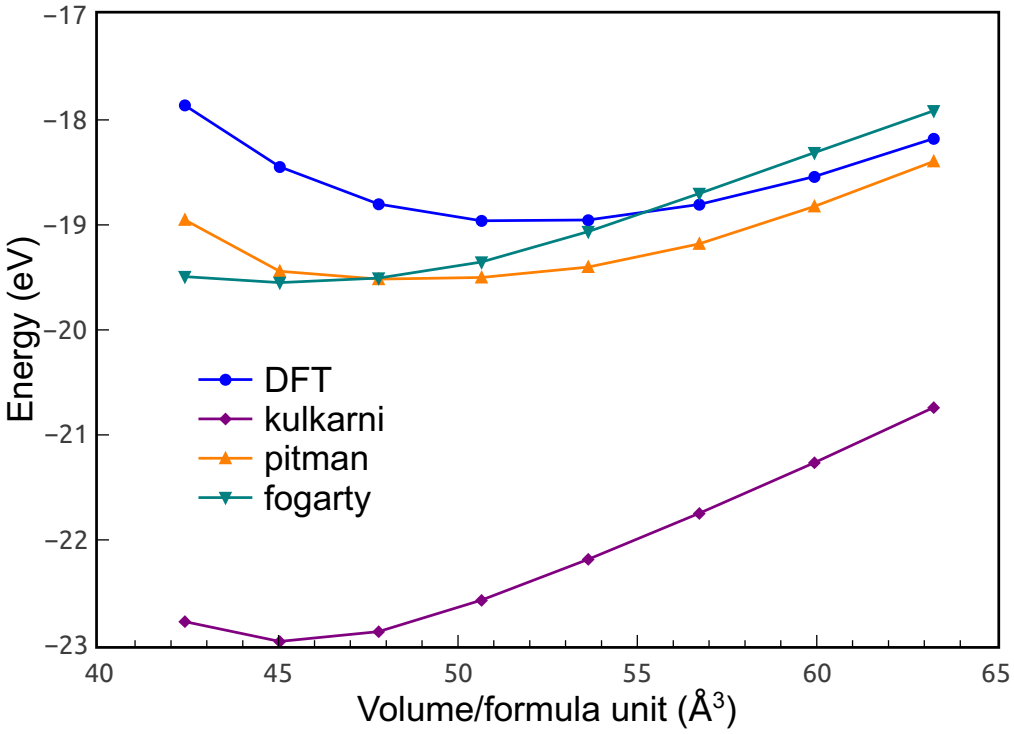

Figure 6.9: Cohesive energy of β-tridymite.

the internal coordinates of the ions and then looked for the α-quartz symmetry. Also, the instability was evident from the significant increase in simulation box size. The lattice dimensions changed by more than 5%. This is shown in Fig. 6.16. For comparison, we also plot on the same graph the result obtained with Kulkarni. We also calculated the bulk modulus of amorphous silica using the current fit (Fig. 6.17). We obtained a very high value of bulk modulus, specifically 303 GPa.

6.8 Fundamental limitations of ReaxFF model

We investigated the bond-order feature of ReaxFF model, and it turns out that it is unable to faithfully describe bond-order behavior of chemical bonds. The idea is when an atom has more neighbors around it, each bond should get weaker than if there were only that bond. We calculated Si-O bond energy for one-fold to all the way five-fold Si, and in each case Si-O bond energy came

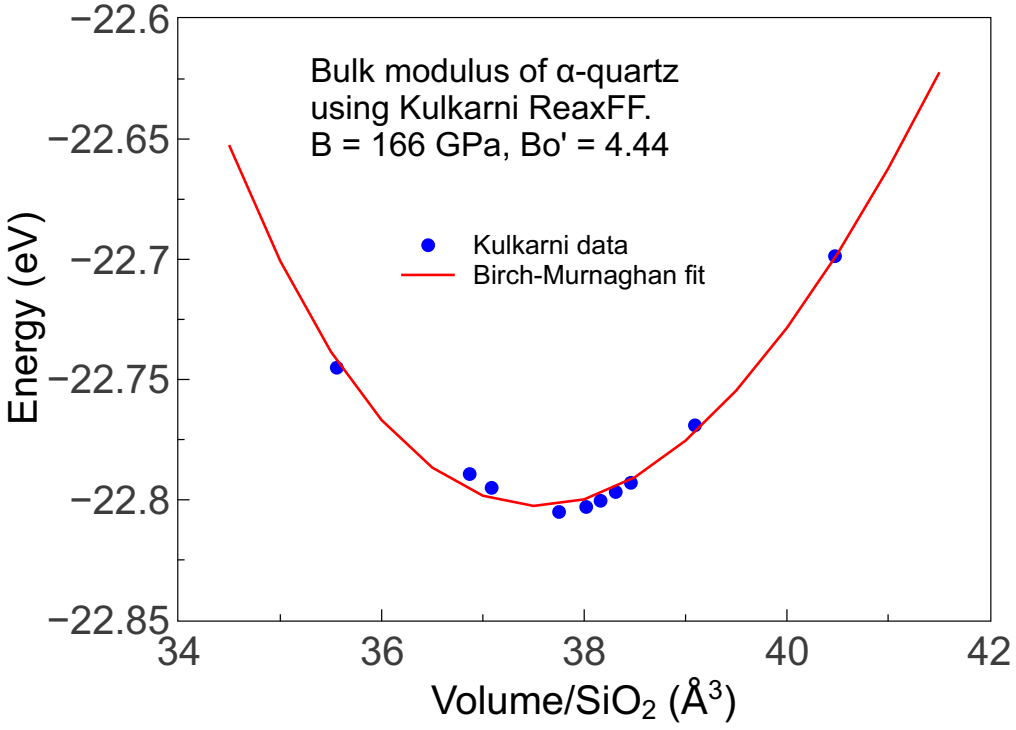

Figure 6.10: Equation of state of α-quartz obtained with Kulkarni model at T = 0 K.

to be almost the same, though it should not be the case. There are other circumstantial evidences that indicate ReaxFF model has limitations in describing different coordination state of an atom. For example, stishovite is a silica polymorph where Si is octahedrally coordinated to oxygen, i.e., its coordination number is 6. ReaxFF model cannot produce cohesive energy which is close to the actual value for stishovite. In reality, stishovite has a cohesive energy which is slightly higher than that of α-quartz, which is -19.23 eV. However, Kulkarni model produces cohesive energy for stishovite which is +4.65 eV higher than that obtained for α-quartz with the same model [94]. We also investigated energy changes with changes in some bond-order parameters which are supposed to ensure bond-order property of a chemical system, e.g., p_{be1}, but found that the parameters failed to truly describe the property. This indicates a fundamental limitation in the model.

Unstability of a system during dynamics is not unheard of. Järvi et al. [118] report collapse

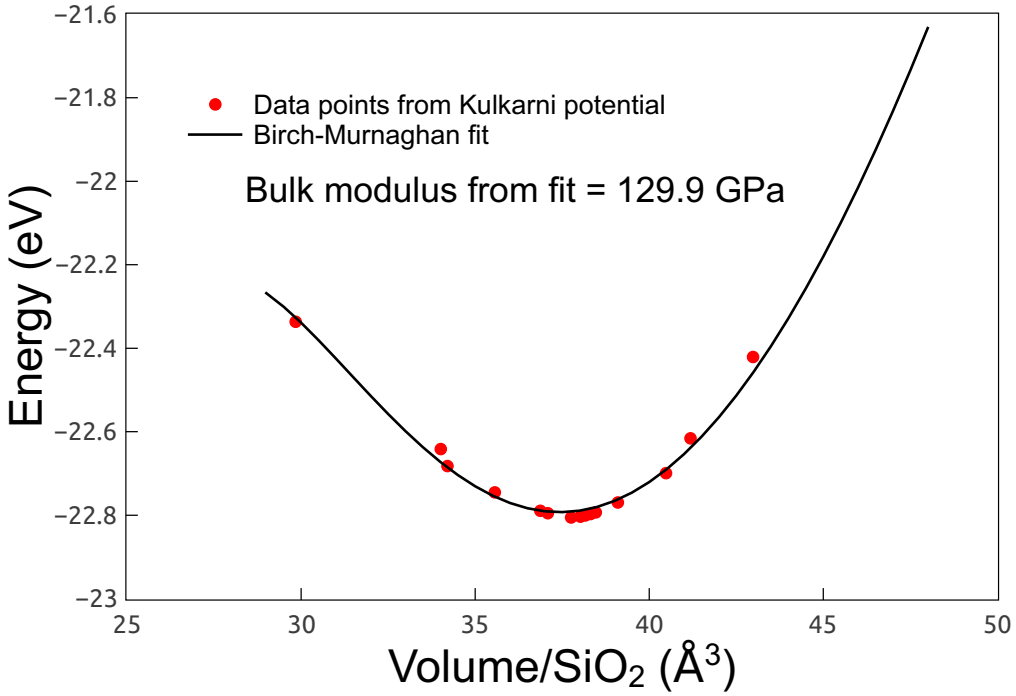

Figure 6.11: Equation of state of amorphous silica obtained with Kulkarni model at T = 0 K.

of bcc gold during NPT simulations. The van Beest-Kramer-van Santen (BSK) paper on silica force field [119] also reported that the fit which gave least error during the fit did not reproduce α-quartz during NPT dynamics.

6.9 Discussion

The difficulty in obtaining ReaxFF models that could stabilize fayalite or silica may lie in several factors. First, there could be some fundamental limitations in the mathematical formulation of the model. Second, since the silica polymorphs have small energy difference in their cohesive energy (Fig. 6.18), during the fit the model can find its minimum state in some neighboring state rather than in the targeted phase.

There are certain issues associated with the procedures that are actually followed during the fit. van Duin et al. [36] uses a fitting procedure where the internal coordinates of the targeted crystal

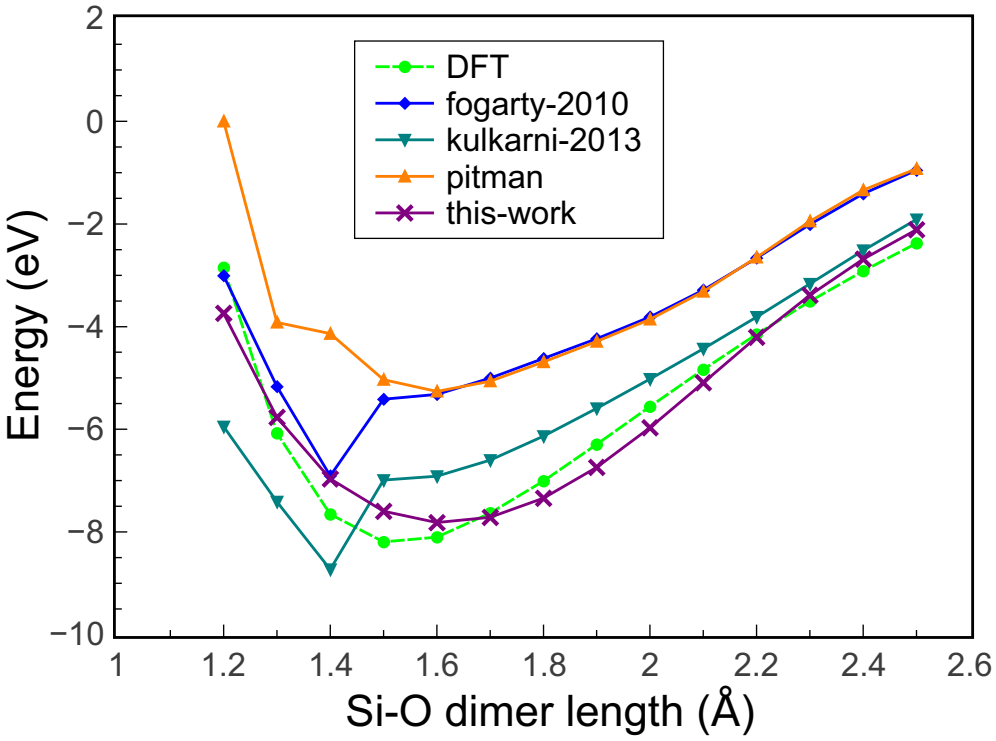

Figure 6.12: Si–O dimer energy obtained with current fit.

structures are allowed to relax during the fit. In other words, the internal coordinates themselves become target during the fit, or become part of the training set. However, we argued the validity of this approach, and carried out our fit using single point energy calculations, where the internal coordinates were not allowed to relax during the fit. There is another issue associated with the fitting procedure. In building the training set, we targeted energies of unrelaxed structures, which could be an issue since the unrelaxed structures are more widely separated in energy than the relaxed structures. Future work on ReaxFF potential fit should address these issues.

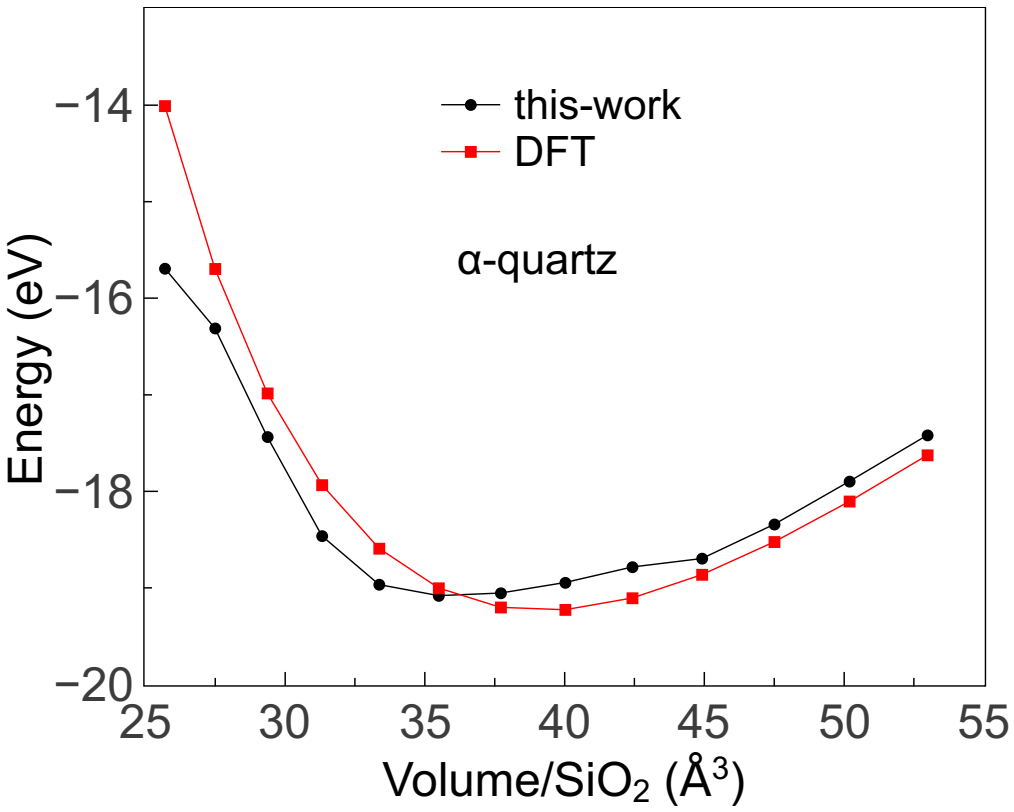

Figure 6.13: α-quartz energy vs volume obtained with current fit.

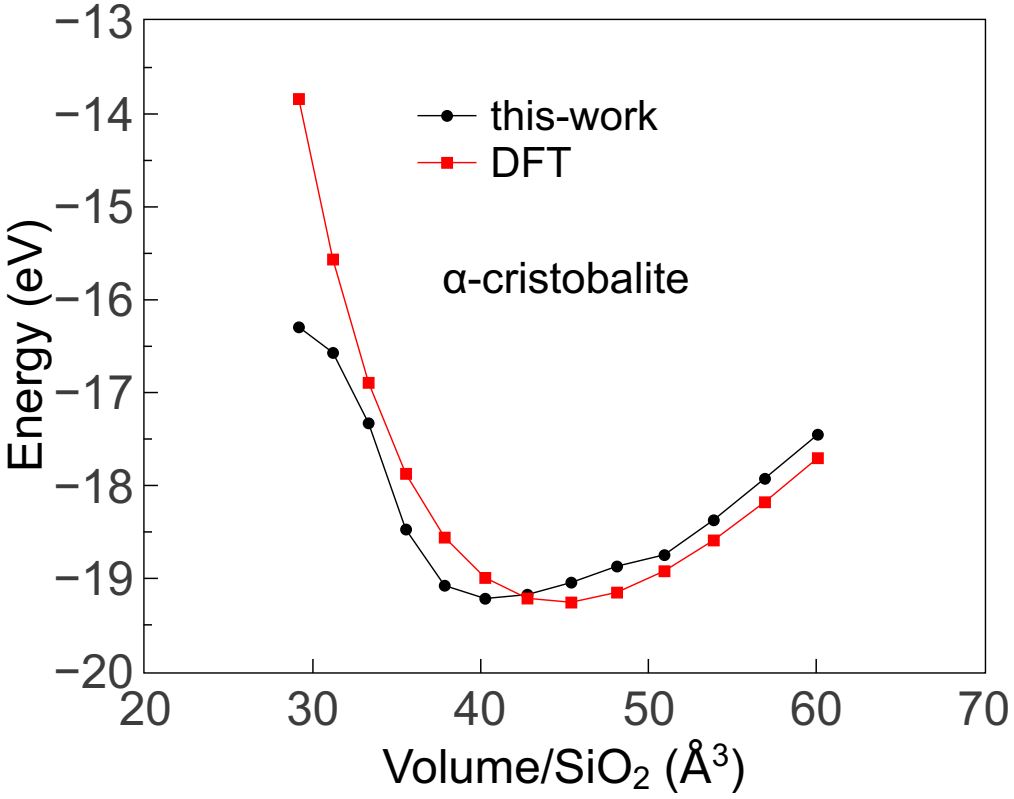

Figure 6.14: α-cristobalite energy vs volume obtained with current fit.

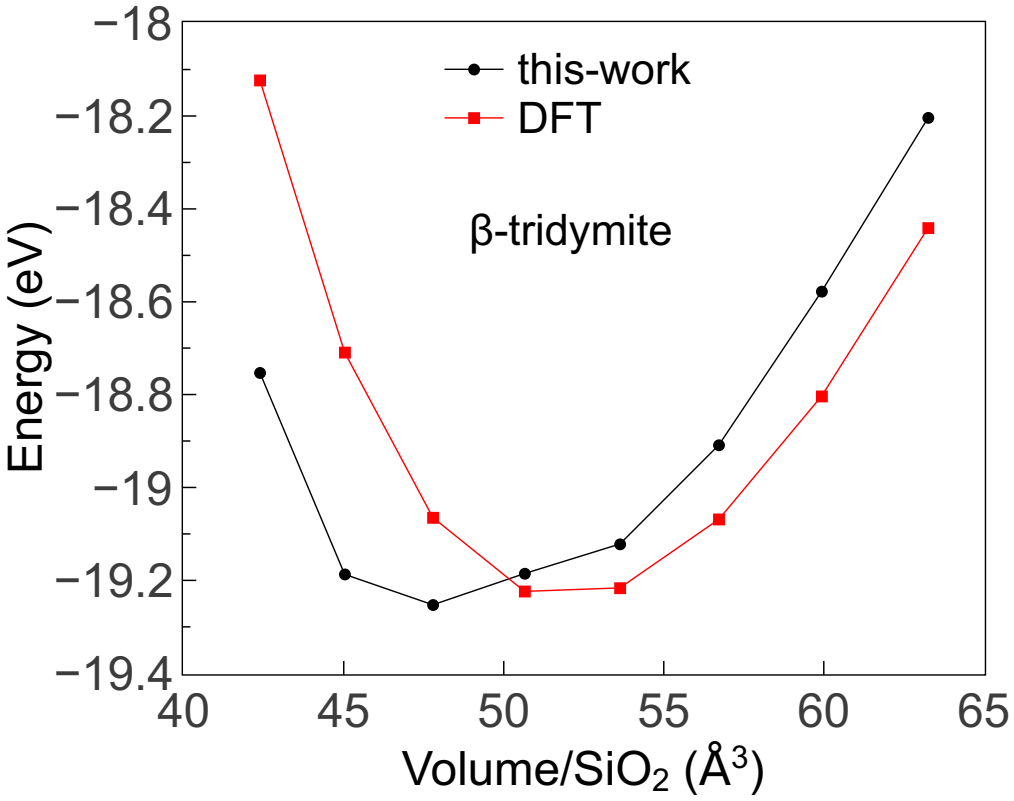

Figure 6.15: β-tridymite energy vs volume obtained with current fit.

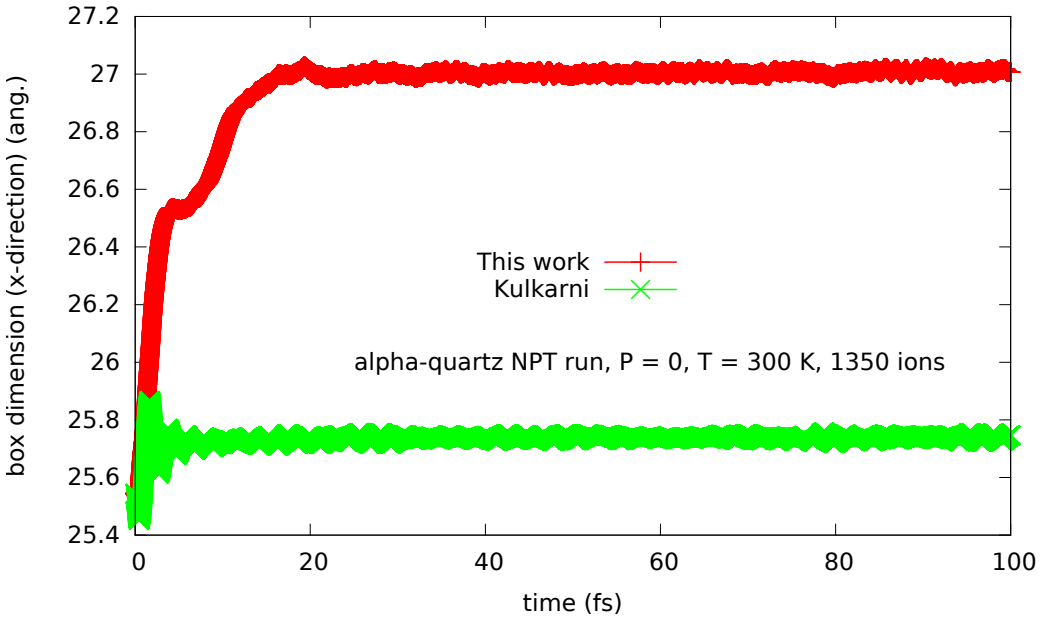

Figure 6.16: Lattice constants of α-quartz increases by more than 5% during NPT run with the current fit. Kulkarni can stablize quartz structure reasonably well.

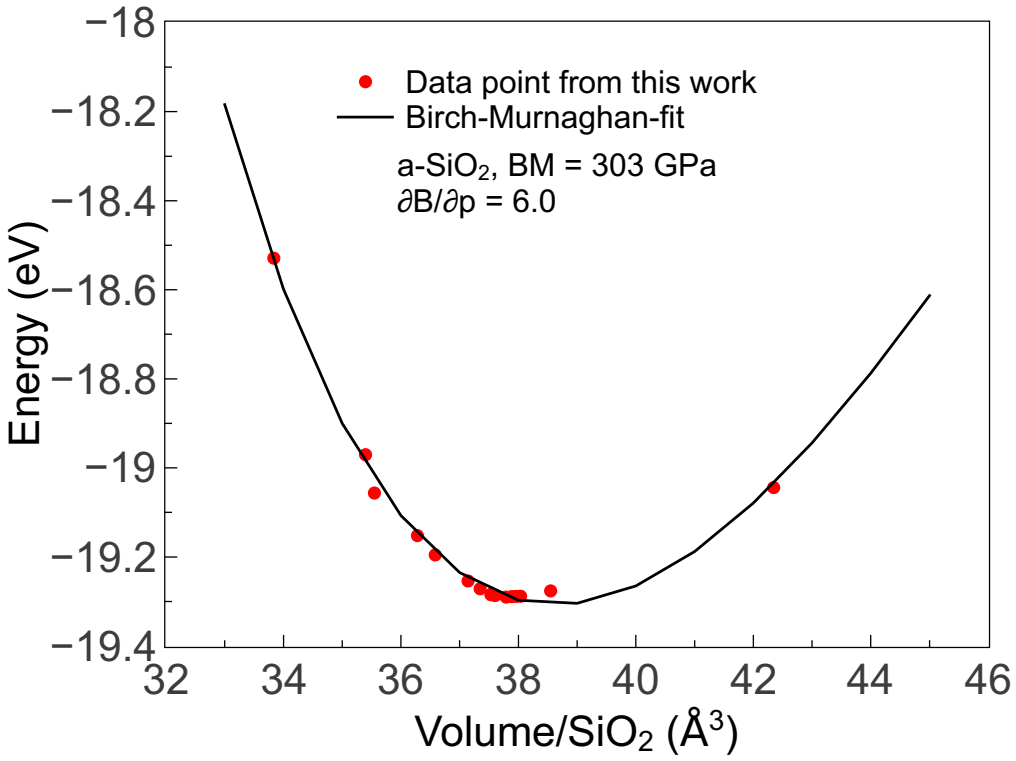

Figure 6.17: Bulk modulus of a-SiO_2 obtained with current fit.

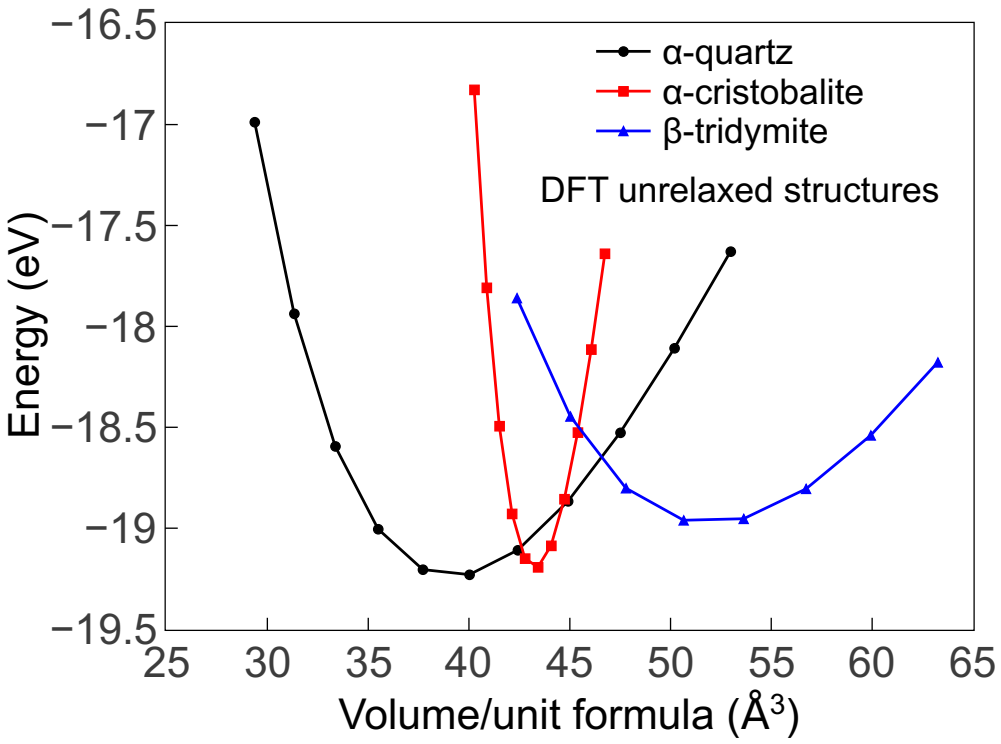

Figure 6.18: Bulk modulus of a-SiO_2 obtained with current fit.

APPENDIX A: MATHEMATICAL FORMULATION OF ReaxFF MODEL

ReaxFF overall system energy contains contributions from different physical interactions, and the complete function is given by the following [120]:

$$E_{system} = E_{bond} + E_{lp} + E_{over} + E_{under} + E_{val} + E_{pen} + E_{coa} + E_{vdWaals} + E_{Coulomb} + E_{triple} + E_{tors} + E_{conj} + E_{H-bond} + E_{C2}, \tag{A.1}$$

where,

E_{bond} = Bond order energy,

E_{lp} = Lone pair energy,

E_{over} = Overcoordination energy,

E_{under} = Undercoordination energy,

E_{val} = Valence angle energy,

E_{pen} = Penatly energy,

E_{coa} = Conjugation energy,

$E_{vdWaals}$ = van der Waals energy,

$E_{Coulomb}$ = Coulumb energy,

E_{tors} = Torsion energy,

E_{conj} = Four-body conjugation energy,

E_{H-bond} = Hydrogen bond energy,

E_{triple} = Triple bond energy.

For the system we considered, we do not need to consider some of the terms in Eq.A.1, e.g., hydrogen bond energy term or triple bond energy term, and the functional form of ReaxFF energy becomes simpler.

$$E_{system} = E_{bond} + E_{lp} + E_{over} + E_{under} + E_{val} + E_{pen} + E_{vdWaals} + E_{Coulomb} + E_{tors} \tag{A.2}$$

The energy terms contain parameters that are fitted for the material system being considered. The

terms in Eq. A.2 contains 56 parameters, as will be seen in the following expressions for the various energy terms.

The bond order energy is given by the following set of equations, where the parameters are D_e^{σ}, p_{be1}, etc.

$$E_{bond} = -\mathbf{D_e^{\sigma}} \cdot BO_{ij}^{\sigma} \cdot \exp\left[\mathbf{p_{be1}}\left(1 - (BO_{ij}^{\sigma})^{\mathbf{Pbe2}}\right)\right] - \mathbf{D_e^{\pi}} \cdot BO_{ij}^{\pi} - \mathbf{D_e^{\pi\pi}} \cdot BO_{ij}^{\pi\pi} \tag{A.3}$$

$$BO_{ij}^{\sigma} = {BO'}_{ij}^{\sigma} \cdot f_1(\Delta_i', \Delta_j') \cdot f_4(\Delta_i', {BO'}_{ij}) \cdot f_5(\Delta_j', \Delta_j')$$

$$BO_{ij}^{\pi} = {BO'}_{ij}^{\pi} \cdot f_1(\Delta_i', \Delta_j') \cdot f_1(\Delta_i', \Delta_j') \cdot f_4(\Delta_i', {BO'}_{ij}) \cdot f_5(\Delta_j', \Delta_j')$$

$$BO_{ij}^{\pi\pi} = {BO'}_{ij}^{\pi\pi} \cdot f_1(\Delta_i', \Delta_j') \cdot f_1(\Delta_i', \Delta_j') \cdot f_4(\Delta_i', {BO'}_{ij}) \cdot f_5(\Delta_j', \Delta_j')$$

The Lone pair energy is calculated from the following four equations, written here in the reverse order they are actually calculated. The parameters are p_{lp1},p_{lp2}.

$$E_{lp} = \frac{p_{lp2}.\Delta_i^{lp}}{1 + \exp\left(-75.\Delta_i^{lp}\right)} \tag{A.4}$$

$$\Delta_i^{lp} = n_{lp,opt} - n_{lp,i} \tag{A.5}$$

$$n_{lp,i} = \left(\frac{\Delta_i^e}{2}\right) + \exp\left[-p_{lp1}.\left(2 + \Delta_i^e - 2.\mathrm{int}\left\{\frac{\Delta_i^e}{2}\right\}\right)^2\right] \tag{A.6}$$

$$\Delta_i^e = -Val_i^e + \sum_{j=1}^{neighbors(i)} BO_{ij} \tag{A.7}$$

Overcoordination energy is given by

$$E_{over} = \frac{\sum_{j=1}^{nbond} p_{ovun1} \cdot D_e^{\sigma}.BO_{ij}}{\Delta_i^{lpcorr} + Val_i} \cdot \Delta_i^{lpcorr}.\left[\frac{1}{1 + \exp\left(p_{ovun2} \cdot \Delta_i^{lpcorr}\right)}\right] \tag{A.8}$$

Undercoordination energy is given by

$$E_{under} = -p_{ovun5}.\frac{1-\exp\Big(p_{ovun6}.\Delta_i^{lpcorr}\Big)}{1+\exp\Big(-p_{ovun2}\cdot\Delta_i^{lpcorr}\Big)}.\frac{1}{1+p_{ovun7}.\exp\left[p_{ovun8}.\Big\{\sum_{j=1}^{neighb(j)}(\Delta_j-\Delta_j^{lp}).(BO_{ij}^{\pi}+BO_{ij}^{\pi\pi})\Big\}\right]} \tag{A.9}$$

As can be seen, the mathematical expressions for various energy terms are quite complicated and the terms contain multiple parameters. These parameters are fit during the development of ReaxFF potential. One can obtain the expressions for other energy terms in Eq. A.2 in the supplemental information provided with [120].

APPENDIX B: SILICA POLYMORPHS

Silica polymorphs are minerals having the chemical composition SiO_2 but different crystal structures, symmetry and physical properties. The silica minerals include quartz, tridymite, cristobalite, coesite, stishovite, and several others. All silica minerals are tectosilicates having structures consisting entirely of SiO_4 tetrahedra (Fig. 2.1) that share all of their oxygen atoms with adjacent tetrahedra. Quartz is the most stable phase, the other phases are found in higher pressure or temperatures (Fig. B.1).

The quartz, cristobalite, tridymite and coesite are low pressure phases where the SiO_4 tetrahedra are connected by corner-sharing oxygens. As such, the Si has fourfold coordination with oxygen. Stishovite in contrast is a polymorph where the silicon is octahedrally coordinated.

As mentioned in Chapter 2, the silica tetrahedron is a very stable structure, and in the silica polymorphs, the Si–O distance remains essentially the same, and varies from 1.58 Å to 1.63 Å [122]. The O-Si-O angle also remains the same and equals about 109° [122]. The polymorphs differ in the way silica tetrahedra are arranged inside them. This lead to differences in the Si-O-Si angles.

Different crystal properties of the silica polymorphs are tabulated in Table B.1. Also their structures are shown in Fig. B.2 and Fig. B.3.

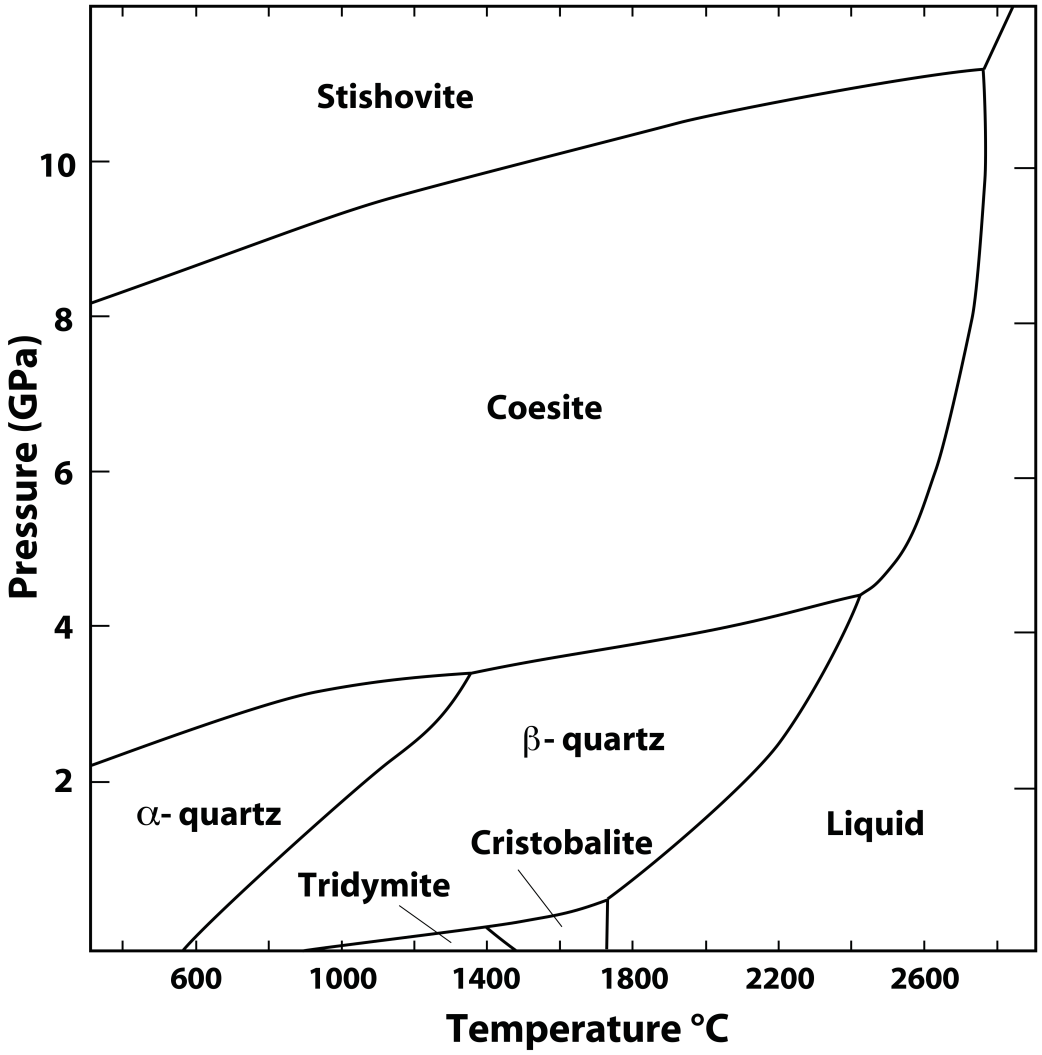

Figure B.1: Phase diagram of silica polymorphs. After Swamy et al. [121].

Table B.1: Structural properties of silica polymorphs from experiments.

Polymorph	Symmetry	Lattice constants (Å) [123]	Internal coordinates [123]	Si-O-Si angle [122]
α-quartz	hexagonal ($P3_121$)	a = 4.9160 c = 5.4054	u = 0.4697 x = 0.4135 y = 0.2669 z = 0.1191	143.7°
α-cristobalite	tetragonal ($P4_12_12$)	a = 4.9570 c = 6.8903	u = 0.3047 x = 0.2381 y = 0.1109 z = 0.1826	146.8°
β-tridymite	hexagonal ($P6_3/mmc$)	a = 5.03 c = 8.22	u = 0.44	180°
Coesite	hexagonal (C 2/c)	a = 7.135 b = 12.372 c = 7.173	cf. [124]	137-180° cf. [124]

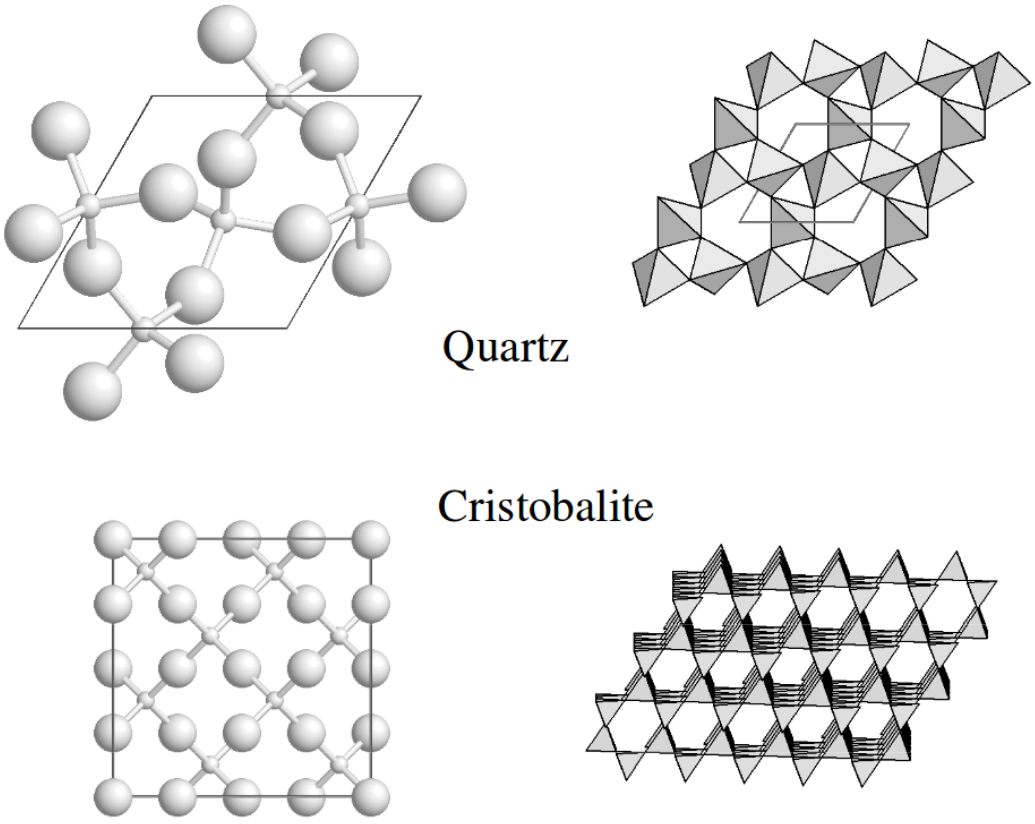

Figure B.2: Structure of quartz and cristobalite.

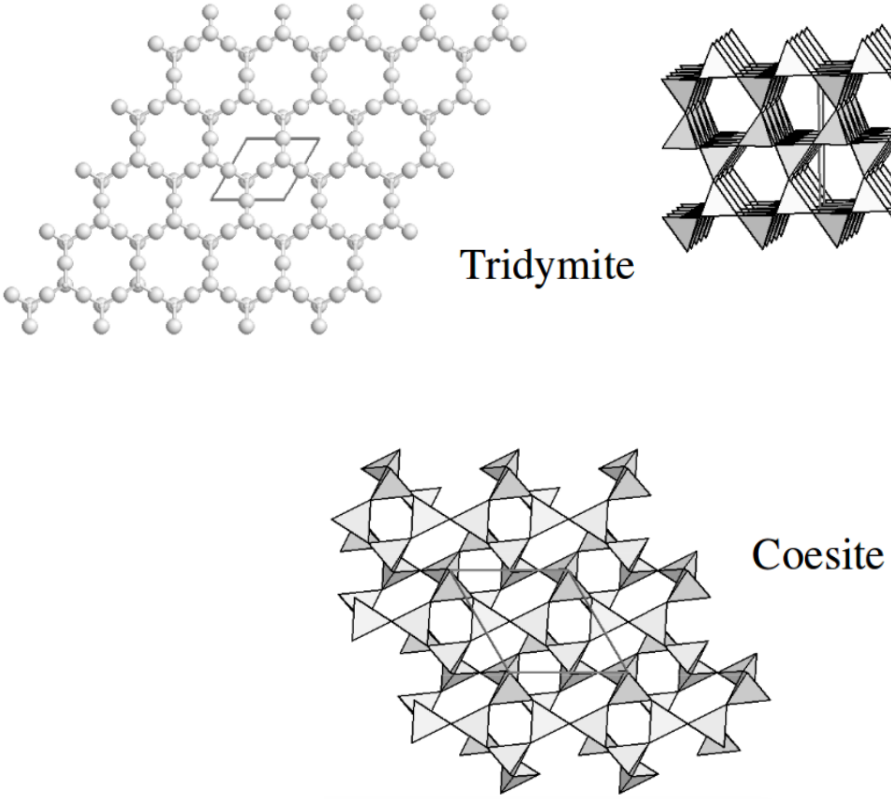

Figure B.3: Structure of tridymite and coesite.

LIST OF REFERENCES

[1] B. Hapke. Space weathering from Mercury to the asteroid belt. *J. Geophys. Res.*, 106: 10039, 2001. doi: 10.1029/2000JE001338.

[2] S. J. Weidenschilling. Formation of planetesimals and accretion of the terrestrial planets. *Space Science Reviews*, 92(1/2):295–310, 2000. doi: 10.1023/a:1005259615299.

[3] A. D. Kulkarni, D. G. Truhlar, S. G. Srinivasan, A. C. T. van Duin, P. Norman, and T. E. Schwartzentruber. Oxygen interactions with silica surfaces: Coupled cluster and density functional investigation and the development of a new ReaxFF potential. *J. Phys. Chem. C*, 117(1):258–269, 2013. doi: 10.1021/jp3086649.

[4] A. Chokshi, A. G. G. M. Tielens, and D. Hollenbach. Dust coagulation. *ApJ*, 407:806, 1993. doi: 10.1086/172562.

[5] C. Dominik and A. G. G. M. Tielens. The physics of dust coagulation and the structure of dust aggregates in space. *ApJ*, 480(2):647–673, 1997. doi: 10.1086/303996.

[6] K. Wada, H. Tanaka, T. Suyama, H. Kimura, and T. Yamamoto. Numerical simulation of dust aggregate collisions. i. compression and disruption of two-dimensional aggregates. *ApJ*, 661(1):320, 2007. doi: 10.1086/514332.

[7] J. J. Lissauer. Theories of Planet Formation: Future Prospects. In S. Udry, W. Benz, and R. von Steiger, editors, *Planetary Systems and Planets in Systems*, page 249, 2006.

[8] V. S. Safronov. *Evolution of the protoplanetary cloud and formation of the earth and planets*. Keter Publishing House, Jerusalem, Israel, 1972. Published first in Russia in 1969.

[9] T. Gold. The lunar surface. *Mon. Not. R. Astron. Soc.*, 115:585, 1955. doi: 10.1093/mnras/115.6.585.

[10] J.B. Adams and R.L. Jones. Spectral reflectivity of lunar samples. *Science*, 167:737–739, 1970. doi: 10.1126/science.167.3918.737.

[11] C. R. Chapman. Space weathering of asteroid surfaces. *Annu. Rev. Earth Planet. Sci.*, 32: 539–567, 2004. doi: 10.1146/annurev.earth.32.101802.120453.

[12] L. P Keller and D. S McKay. Discovery of vapor deposits in the lunar regolith. *Science*, 261:1305–1307, 1993. doi: 10.1126/science.261.5126.1305.

[13] L. P Keller and D. S. McKay. The nature and origin of rims on lunar soil grains. *Geochim. Cosmochim. Acta*, 61:2331–2341, 1997. doi: 10.1016/S0016-7037(97)00085-9.

[14] R. Christoffersen, D. S. McKay, and L. P. Keller. Microstructure, chemistry, and origin of grain rims on ilmenite from the lunar soil finest fraction. *Meteorit. Planet. Sci.*, 31:835–848, 1996. doi: 10.1111/j.1945-5100.1996.tb02117.x.

[15] T. Noguchi, M. Kimura, T. Hashimoto, M. Konno, T. Nakamura, M. E. Zolensky, R. Okazaki, M. Tanaka, A. Tsuchiyama, A. Nakato, T. Ogami, H. Ishida, R. Sagae, S. Tsujimoto, T. Matsumoto, J. Matsuno, A. Fujimura, M. Abe, T. Mukai, M. Ueno, T. Okada, K. Shirai, and Y. Ishibashi. Space weathered rims found on the surfaces of the Itokawa dust particles. *Meteorit. Planet. Sci.*, 49:188–214, 2014. doi: 10.1111/maps.12111.

[16] M. S. Thompson, R. Christoffersen, T. J. Zega, and L. P. Keller. Microchemical and structural evidence for space weathering in soils from asteroid Itokawa. *Earth, Planets Space*, 66, 2014. doi: 10.1186/1880-5981-66-89.

[17] M. Yamada, S. Sasaki, H. Nagahara, A. Fujiwara, S. Hasegawa, H. Yano, T. Hiroi, H. Ohashi, and H. Otake. Simulation of space weathering of planet-forming materials: Nanosecond pulse laser irradiation and proton implantation on olivine and pyroxene samples. *Earth, Planets Space*, 51:1255–1265, 1999. doi: 10.1186/BF03351599.

[18] S. Sasaki, K. Nakamura, Y. Hamabe, E. Kurahashi, and T. Hiroi. Production of iron nanoparticles by laser irradiation in a simulation of lunar-like space weathering. *Nature*, 410:555–557, 2001. doi: 10.1038/35069013.

[19] Sin iti Sirono. Conditions for collisional growth of a grain aggregate. *Icarus*, 167(2):431–452, 2004. doi: 10.1016/j.icarus.2003.09.018.

[20] R. van Boekel, M. Min, Ch. Leinert, L.B.F.M. Waters, A. Richichi, O. Chesneau, C. Dominik, W. Jaffe, A. Dutrey, U. Graser, Th. Henning, J. de Jong, R. Köhler, A. de Koter, B. Lopez, F. Malbet, S. Morel, F. Paresce, G. Perrin, Th. Preibisch, F. Przygodda, M. Schöller, and M. Wittkowski. The building blocks of planets within the 'terrestrial' region of protoplanetary disks. *Nature*, 432(7016):479–482, 2004. doi: 10.1038/nature03088.

[21] J.E. Chambers and G.W. Wetherill. Making the terrestrial planets: N-body integrations of planetary embryos in three dimensions. *Icarus*, 136(2):304–327, 1998. doi: 10.1006/icar.1998.6007.

[22] K. L. Johnson, K. Kendall, and A. D. Roberts. Surface energy and the contact of elastic solids. *Proc. R. Soc. A*, 324(1558):301–313, 1971. doi: 10.1098/rspa.1971.0141.

[23] K. Wada, H. Tonaka, T. Suyama, H. Kimura, and T. Yamamoto. Numerical simulation of dust aggregate collisions. II. compression and disruption of three-dimensional aggregates in head-on collisions. *ApJ*, 677:1296, 2008. doi: 10.1086/529511.

[24] T. Suyama, K. Wada, and H. Tanaka. Numerical simulation of density evolution of dust aggregates in protoplanetary disks. i. head-on collisions. *Astrophys. J.*, 684(2):1310–1322, 2008. doi: 10.1086/590143.

[25] T. Poppe, Jürgen Blum, and T. Henning. Analogous experiments on the stickiness of micron-sized preplanetary dust. *Astrophys. J.*, 533(1):454–471, 2000. doi: 10.1086/308626.

[26] S. Krijt, C. Gttler, D. Heielmann, C. Dominik, and A. G. G. M. Tielens. Energy dissipation in head-on collisions of spheres. *J. Phys. D: Appl. Phys.*, 46(43):435303, 2013. doi: 10.1088/0022-3727/46/43/435303.

[27] A. Zsom, C. W. Ormel, C. Gttler, J. Blum, and C. P. Dullemond. The outcome of protoplanetary dust growth: pebbles, boulders, or planetesimals? ii. introducing the bouncing barrier. *Astronomy and Astrophysics*, 513:A57, 2010. doi: 10.1051/0004-6361/200912976.

[28] A. Pedone, G. Malavasi, M. C. Menziani, A. N. Cormack, and U. Segre. A new self-consistent empirical interatomic potential model for oxides, silicates, and silica-based glasses. *J. Phys. Chem. B*, 110:11780–11795, 2006. doi: 10.1021/jp0611018.

[29] T. Henning. Cosmic silicates. *Annu. Rev. Astron. Astrophys.*, 48(1):21–46, 2010. doi: 10.1146/annurev-astro-081309-130815.

[30] J. D. Birle, G. V. Gibbs, P. B. Moore, and J. V. Smith. Crystal structures of natural olivines. *Am. Mineral.*, 53:807–824, 1968.

[31] R. M. Hazen. Effects of temperature and pressure on the crystal structure of forsterite. *Am. Mineral.*, 61:1280–1293, 1976.

[32] S. Sueno, M. Cameron, and C. T. Prewitt. Orthoferrosilite: High-temperature crystal chemistry. *Am. Mineral.*, 61:38–53, 1976.

[33] E. R. Hernández. Molecular dynamics: from basic techniques to applications (A Molecular Dynamics Primer). *AIP Conference Proceedings*, 1077(1):95–123, 2008. doi: 10.1063/1.3040265.

[34] S. Nosé. A unified formulation of the constant temperature molecular dynamics methods. *J. Chem. Phys.*, 81(1):511–519, 1984. doi: 10.1063/1.447334.

[35] W. G. Hoover. Canonical dynamics: Equilibrium phase-space distributions. *Phys. Rev. A*, 31(3):1695–1697, 1985. doi: 10.1103/physreva.31.1695.

[36] A. C. T. van Duin, S. Dasgupta, F. Lorant, and W. A. Goddard. ReaxFF: a reactive force field for hydrocarbons. *J. Phys. Chem. A*, 105(41):9396–9409, 2001. doi: 10.1021/jp004368u.

[37] W. J. Mortier, S. K. Ghosh, and S. Shankar. Electronegativity-equalization method for the calculation of atomic charges in molecules. *J. Am. Chem. Soc.*, 108(15):4315–4320, 1986. doi: 10.1021/ja00275a013.

[38] G. O. A. Janssens, B. G. Baekelandt, H. Toufar, W. J. Mortier, and R. A. Schoonheydt. Comparison of cluster and infinite crystal calculations on zeolites with the electronegativity equalization method (EEM). *J. Phys. Chem.*, 99(10):3251–3258, 1995. doi: 10.1021/j100010a041.

[39] T. Liang, Y. K. Shin, Y.-T. Cheng, D. E. Yilmaz, K. G. Vishnu, O. Verners, C. Zou, S. R. Phillpot, S. B. Sinnott, and A. C. T. van Duin. Reactive potentials for advanced atomistic simulations. *Annu. Rev. Mater. Res.*, 43(1):109–129, 2013. doi: 10.1146/annurev-matsci-071312-121610.

[40] P. Hohenberg and W. Kohn. Inhomogeneous electron gas. *Physical Review*, 136(3B):B864–B871, 1964. doi: 10.1103/physrev.136.b864.

[41] W. Kohn and L. J. Sham. Self-consistent equations including exchange and correlation effects. *Physical Review*, 140(4A):A1133–A1138, 1965. doi: 10.1103/physrev.140.a1133.

[42] J. D. Gale and A. L. Rohl. The General Utility Lattice Program (GULP). *Mol. Sim.*, 29: 291–341, 2003. doi: 10.1080/0892702031000104887.

[43] P. P. Ewald. Die berechnung optischer und elektrostatischer gitterpotentiale. *Annalen der Physik*, 369(3):253–287, 1921. doi: 10.1002/andp.19213690304.

[44] D. Frenkel and B. Smit. *Understanding Molecular Simulation: From Algorithms to Applications*. Academic Press, 2001.

[45] J. R. Smyth and T. C. McCormick. Crystallographic data for minerals. In T. J. Ahrens, editor, *Mineral Physics & Crystallography: A Handbook of Physical Constants*, pages 1–17. American Geophysical Union, Washington, D.C., 1995. doi: 10.1029/RF002.

[46] J. D. Bass. Elasticity of Minerals, Glasses, and Melts. In T. J. Ahrens, editor, *Mineral Physics & Crystallography: A Handbook of Physical Constants*, pages 45–63. American Geophysical Union, Washington, D.C., 1995. doi: 10.1029/RF002.

[47] R. Shannon, MA Subramanian, S Hosoya, and GR Rossman. Dielectric constants of tephroite, fayalite and olivine and the oxide additivity rule. *Phys. Chem. Miner.*, 18:1–6, 1991. doi: 10.1007/BF00199037.

[48] G. R. Olhoeft. Electrical properties of rocks. In Y. S. Touloukian, W. R. Judd, and R. F. Roy, editors, *CINDAS Data Series on Material Properties, Volume II-2, Physical Properties of Rocks and Minerals*, pages 257–329. Hemisphere Publishing Corporation, New York, 1989.

[49] A. Tilocca, N. H de Leeuw, and A. N. Cormack. Shell-model molecular dynamics calculations of modified silicate glasses. *Phys. Rev. B*, 73:104209, 2006. doi: 10.1103/PhysRevB.73.104209.

[50] W. Cassidy and B. Hapke. Effects of darkening processes on surfaces of airless bodies. *Icarus*, 25:371–383, 1975. doi: 10.1016/0019-1035(75)90002-0.

[51] R. Christoffersen and L. P Keller. Space radiation processing of sulfides and silicates in primitive solar systems materials: Comparative insights from in situ TEM ion irradiation experiments. *Meteorit. Planet. Sci.*, 46(7):950–969, 2011. doi: 10.1111/j.1945-5100.2011.01203.x.

[52] L. M. Wang, M. L. Miller, and R. C. Ewing. HRTEM study of displacement cascade damage in krypton-ion-irradiated silicate – olivine. *Ultramicroscopy*, 51:339–347, 1993. doi: 10.1016/0304-3991(93)90159-U.

[53] L. M. Wang, W. L. Gong, , and R. C. Ewing. Amorphization and dynamic recovery of A_2BO_4 structure types during 1.5 MeV krypton ion-beam irradiation. In *Symposium A – Materials Synthesis and Processing Using Ion Beams*, volume 316 of *MRS Online Proceedings Library*, 1993. doi: 10.1557/PROC-316-247.

[54] S. X. Wang, L. M. Wang, R. C. Ewing, and R. H. Doremus. Ion beam-induced amorphization in MgO–Al_2O_3–SiO_2. I. Experimental and theoretical basis. *J. Non-Cryst. Solids*, 238: 198–213, 1998. doi: 10.1016/S0022-3093(98)00694-2.

[55] P. Carrez, K. Demyk, P. Cordier, L. Gengembre, J. Grimblot, L. D'Hendecourt, A. P Jones, and H. Leroux. Low-energy helium ion irradiation-induced amorphization and chemical changes in olivine: Insights for silicate dust evolution in the interstellar medium. *Meteorit. Planet. Sci.*, 37:1599–1614, 2002. doi: 10.1111/j.1945-5100.2002.tb00814.x.

[56] S. Sasaki and E. Kurahashi. Space weathering on Mercury. *Adv. Space Res.*, 33:2152–2155, 2004. doi: 10.1016/S0273-1177(03)00442-3.

[57] L. R. Corrales and W. J. Weber. State of theory and computer simulations of radiation effects in ceramics. *Curr. Opin. Solid State Mater. Sci.*, 7(1):35 – 40, 2003. ISSN 1359-0286. doi: 10.1016/S1359-0286(03)00016-0.

[58] R. E. Stoller. Primary radiation damage formation. In R. J. M. Konings, T. R. Allen, R. E. Stoller, and S. Yamanaka, editors, *Compr. Nucl. Mater.*, volume 1, pages 293–332. Elsevier Ltd., Amsterdam, 2012. doi: 10.1016/B978-0-08-056033-5.00027-6.

[59] D. S. Aidhy, P. C. Millett, D. Wolf, S. R. Phillpot, and H. Huang. Kinetically driven point-defect clustering in irradiated MgO by molecular-dynamics simulation. *Scripta Mater.*, 60: 691–694, 2009. doi: 10.1016/j.scriptamat.2008.12.052.

[60] D. S. Aidhy, P. C. Millett, T. Desai, D. Wolf, and S. R. Phillpot. Kinetically evolving irradiation-induced point defect clusters in UO_2 by molecular dynamics simulation. *Phys. Rev. B*, 80:104107, 2009. doi: 10.1103/PhysRevB.80.104107.

[61] D. S. Aidhy, D. Wolf, and A. E.-Azab. Comparison of point-defect clustering in irradiated CeO_2 and UO_2: A unified view from molecular dynamics simulations and experiments. *Scripta Mater.*, 65:867–870, 2011. doi: 10.1016/j.scriptamat.2011.07.051.

[62] E. Zarkadoula, R. Devanathan, W. J. Weber, M. A. Seaton, I. T. Todorov, K. Nordlund, M. T. Dove, and K. Trachenko. High-energy radiation damage in zirconia: Modeling results. *J. Appl. Phys.*, 115:083507, 2014. doi: 10.1063/1.4866989.

[63] C. Yang, E. Zarkadoula, M. T. Dove, I. T. Todorov, T. Geisler, V. V. Brazhkin, and K. Trachenko. Solid-state diffusion in amorphous zirconolite. *J. Appl. Phys.*, 116:184901, 2014. doi: 10.1063/1.4901326.

[64] K. O. Trachenko, M. T. Dove, and E. K. H. Salje. Atomistic modelling of radiation damage in zircon. *J. Phys.: Cond. Matt.*, 13(9):1947–1959, 2001. doi: 10.1088/0953-8984/13/9/317.

[65] S. I. Golubov. Radiation damage theory. In R. J. M. Konings, T. R. Allen, R. E. Stoller, and S. Yamanaka, editors, *Compr. Nucl. Mater.*, volume 1, pages 357–391. Elsevier Ltd., Amsterdam, 2012. doi: 10.1016/B978-0-08-056033-5.00029-X.

[66] T. D. de la Rubia, H. M. Zbib, T. A. Khraishi, B. D. Wirth, M. Victoria, and M. J. Caturla.

Multiscale modelling of plastic flow localization in irradiated materials. *Nature*, 406(6798): 871–874, 2000. doi: 10.1038/35022544.

[67] K. P. Zolnikov, A. V. Korchuganov, and D. S. Kryzhevich. Molecular dynamics simulation of primary radiation damage in fe–cr alloy. *Journal of Physics: Conference Series*, 774: 012130, 2016. doi: 10.1088/1742-6596/774/1/012130.

[68] A. K. Verma and B. B. Karki. Ab initio investigations of native and protonic point defects in Mg_2SiO_4 polymorphs under high pressure. *Earth Planet. Sci. Lett.*, 285:140–149, 2009. doi: 10.1016/j.epsl.2009.06.009.

[69] S. Plimpton. Fast parallel algorithms for short-range molecular dynamics. *J. Comput. Phys.*, 117(1):1–19, 1995. doi: 10.1006/jcph.1995.1039.

[70] W. D. Carlson, J. S. Swinnea, and D. E. Miser. Stability of orthoenstatite at high temperature and low pressure. *Am. Mineral.*, 73:1255–1263, 1988.

[71] D. Wolf, P. Keblinski, S. R. Phillpot, and J. Eggebrecht. Exact method for the simulation of Coulombic systems by spherically truncated, pairwise r^{-1} summation. *J. Chem. Phys.*, 110:8254–8282, 1999. doi: 10.1063/1.478738.

[72] P. Demontis, S. Spanu, and G. B. Suffritti. Application of the Wolf method for the evaluation of Coulombic interactions to complex condensed matter systems: Aluminosilicates and water. *J. Chem. Phys.*, 114:7980–7988, 2001. doi: 10.1063/1.1364638.

[73] D. K. Buening and P. R. Buseck. Fe-Mg lattice diffusion in olivine. *J. Geophys. Res.*, 78: 6852–6862, 1973. doi: 10.1029/JB078i029p06852.

[74] J. R. Farver. Oxygen self-diffusion in diopside with application to cooling rate determinations. *Earth Planet. Sci. Lett.*, 92:386–396, 1989. doi: 10.1016/0012-821X(89)90062-9.

[75] A. C. Lasaga. Defect calculations in silicates: olivine. *Am. Mineral.*, 65:1237–1248, 1980.

[76] K. P. R. Reddy, S. M. Oh, L. D. Major, and A. R. Cooper. Oxygen diffusion in forsterite. *J. Geophys. Res.: Solid Earth*, 85:322–326, 1980. doi: 10.1029/JB085iB01p00322.

[77] C. S. Schwandt, R. T. Cygan, and H. R. Westrich. Magnesium self-diffusion in orthoenstatite. *Contrib. Mineral. Petrol.*, 130:390–396, 1998. doi: 10.1007/s004100050373.

[78] J. Ingrin, L. Pacaud, and O. Jaoul. Anisotropy of oxygen diffusion in diopside. *Earth Planet. Sci. Lett.*, 192:347–361, 2001. doi: 10.1016/S0012-821X(01)00460-5.

[79] A. M. Walker, S. M. Woodley, B. Slater, and K. Wright. A computational study of magnesium point defects and diffusion in forsterite. *Phys. Earth Planet. Inter.*, 172:20 – 27, 2009. doi: 10.1016/j.pepi.2008.04.001.

[80] F. J. M. Rietmeijer. The irradiation-induced olivine to amorphous pyroxene transformation preserved in an interplanetary dust particle. *Astrophys. J.*, 705:791–797, 2009. doi: 10.1088/0004-637X/705/1/791.

[81] J. Blum and M. Münch. Experimental investigations on aggregate-aggregate collisions in the early solar nebula. *Icarus*, 106(1):151–167, 1993. doi: 10.1006/icar.1993.1163.

[82] J. Blum. Experiments on sticking, restructuring, and fragmentation of preplanetary dust aggregates. *Icarus*, 143(1):138–146, 2000. doi: 10.1006/icar.1999.6234.

[83] G. Wurm, G. Paraskov, and O. Krauss. Growth of planetesimals by impacts at $\sim$25 m/s. *Icarus*, 178(1):253–263, 2005. doi: 10.1016/j.icarus.2005.04.002.

[84] A. D. Whizin, Jürgen Blum, and J. E. Colwell. The physics of protoplanetesimal dust agglomerates. VIII. microgravity collisions between porous SiO2aggregates and loosely bound agglomerates. *ApJ*, 836(1):94, 2017. doi: 10.3847/1538-4357/836/1/94.

[85] J. Blum, G. Wurm, T. Poppe, and L.-O. Heim. Aspects of laboratory dust aggregation with relevance to the formation of planetesimals. *EM&P*, 80(1/3):285–309, 1998. doi: 10.1023/a:1006386417473.

[86] A. C. T. van Duin, A. Strachan, S. Stewman, Q. Zhang, X. Xu, and W. A. Goddard. ReaxFF$_{SiO_2}$ reactive force field for silicon and silicon oxide systems. *J. Phys. Chem. A*, 107(19):3803–3811, 2003. doi: 10.1021/jp0276303.

[87] J. C. Fogarty, H. M. Aktulga, A. Y. Grama, A. C. T. van Duin, and S. A. Pandit. A reactive molecular dynamics simulation of the silica-water interface. *J. Chem. Phys.*, 132(17): 174704, 2010. doi: 10.1063/1.3407433.

[88] B. P. Feuston and S. H. Garofalini. Empirical three-body potential for vitreous silica. *J. Chem. Phys.*, 89(9):5818–5824, 1988. doi: 10.1063/1.455531.

[89] C. Dominik and A. G. G. M. Tielens. Resistance to sliding on atomic scales in the adhesive contact of two elastic spheres. *Phil. Mag. A*, 73(5):1279–1302, 1996. doi: 10.1080/01418619608245132.

[90] A. Awasthi, S. C. Hendy, P. Zoontjens, S. A. Brown, and F. Natali. Molecular dynamics simulations of reflection and adhesion behavior in lennard-jones cluster deposition. *Phys. Rev. B*, 76(11), 2007. doi: 10.1103/PhysRevB.76.115437.

[91] A. H. Quadery, S. Pacheco, A. Au, N. Rizzacasa, J. Nichols, T. Le, C. Glasscock, and P. K. Schelling. Atomic-scale simulation of space weathering in olivine and orthopyroxene. *JGR: Planets*, 120(4):643–661, 2015. doi: 10.1002/2014je004683.

[92] H. Kimura, K. Wada, H. Senshu, and H. Kobayashi. Cohesion of amorphous silica spheres: Toward a better understanding of the coagulation growth of silicate dust aggregates. *ApJ*, 812(1):67, 2015. doi: 10.1088/0004-637x/812/1/67.

[93] A. Roder, W. Kob, and K. Binder. Structure and dynamics of amorphous silica surfaces. *J. Chem. Phys.*, 114(17):7602–7614, 2001. doi: 10.1063/1.1360257.

[94] A. F.-Lanord, P. Soukiassian, C. Glattli, and E. Wimmer. Ab *initio* parameterization of a charge optimized many-body forcefield for $sisio_2$: Validation and thermal transport in nanostructures. *J. Chem. Phys.*, 144(10):104705, 2016. doi: 10.1063/1.4943396.

[95] T. P. M. Goumans, A. Wander, W. A. Brown, and C. R. A. Catlow. Structure and stability of the (001) α-quartz surface. *Phys. Chem. Chem. Phys.*, 9(17):2146–2152, 2007. doi: 10.1039/b701176h.

[96] S. Leroch and M. Wendland. Simulation of forces between humid amorphous silica surfaces: A comparison of empirical atomistic force fields. *J. Phys. Chem. C*, 116(50):26247–26261, 2012. doi: 10.1021/jp302428b.

[97] L.T. Zhuravlev. The surface chemistry of amorphous silica. zhuravlev model. *Colloids Surf., A*, 173(1-3):1–38, 2000. doi: 10.1016/s0927-7757(00)00556-2.

[98] A. C.-Vives. Amorphous SiO_2 surface models: energetics of the dehydroxylation process, strain, ab initio atomistic thermodynamics and IR spectroscopic signatures. *Phys. Chem. Chem. Phys.*, 18(10):7475–7482, 2016. doi: 10.1039/c6cp00602g.

[99] A. C. Boley, M. A. Morris, and E. B. Ford. Overcoming the meter barrier and the formation of systems with tightly packed inner planets (STIPs). *ApJ*, 792(2):L27, 2014. doi: 10.1088/2041-8205/792/2/l27.

[100] F. J. Ciesla. Chondrule collisions in shock waves. *Meteorit. Planet. Sci.*, 41(9):1347–1359, 2006. doi: 10.1111/j.1945-5100.2006.tb00526.x.

[101] I. V. Schweigert, K. E. J. Lehtinen, M. J. Carrier, and M. R. Zachariah. Structure and

properties of silica nanoclusters at high temperatures. *Phys. Rev. B*, 65(23), 2002. doi: 10.1103/physrevb.65.235410.

[102] Saman Alavi and Donald L. Thompson. Molecular dynamics simulations of the melting of aluminum nanoparticles†. *The Journal of Physical Chemistry A*, 110(4):1518–1523, 2006. doi: 10.1021/jp053318s.

[103] E. Calderon, M. Gauthier, F. Decremps, G. Hamel, G. Syfosse, and A. Polian. Complete determination of the elastic moduli of α-quartz under hydrostatic pressure up to 1 GPa: an ultrasonic study. *J. Phys.: Cond. Matt.*, 19(43):436228, 2007. doi: 10.1088/0953-8984/19/43/436228.

[104] W. Pabst and E. Gregorová. Elastic properties of silica polymorphs–a review. *Ceram.-Silik.*, 57(3):167, 2013.

[105] Y. Zhang, A. Otani, and E. J. Maginn. Reliable viscosity calculation from equilibrium molecular dynamics simulations: A time decomposition method. *J. Chem. Theory Comput.*, 11(8):3537–3546, 2015. doi: 10.1021/acs.jctc.5b00351.

[106] J. Horbach and W. Kob. Static and dynamic properties of a viscous silica melt. *Phys. Rev. B*, 60(5):3169–3181, 1999. doi: 10.1103/physrevb.60.3169.

[107] F. J. Ciesla, D. S. Lauretta, and L. L. Hood. The frequency of compound chondrules and implications for chondrule formation. *Meteorit. Planet. Sci.*, 39(4):531–544, 2004. doi: 10.1111/j.1945-5100.2004.tb00917.x.

[108] Alexander Hubbard. Compound chondrules fused cold. *Icarus*, 254:56–61, 2015. doi: 10.1016/j.icarus.2015.02.030.

[109] M. Aryanpour, A. C. T. van Duin, and J. D. Kubicki. Development of a reactive force

field for iron-oxyhydroxide systems. *J. Phys. Chem. A*, 114(21):6298–6307, 2010. doi: 10.1021/jp101332k.

[110] J. P. Perdew, K. Burke, and M. Ernzerhof. Generalized gradient approximation made simple. *Phys. Rev. Lett.*, 77(18):3865–3868, 1996. doi: 10.1103/physrevlett.77.3865.

[111] B. Lafuente, R. T. Downs, H. Yang, and N. Stone. 1. the power of databases: The RRUFF project. In *Highlights in Mineralogical Crystallography*, pages 1–30. DE GRUYTER, 2016. doi: 10.1515/9783110417104-003.

[112] T. Björkman. CIF2cell: Generating geometries for electronic structure programs. *Computer Physics Communications*, 182(5):1183–1186, 2011. doi: 10.1016/j.cpc.2011.01.013.

[113] A. C. T. van Duin, J. M. A. Baas, and B. van de Graaf. Delft molecular mechanics: a new approach to hydrocarbon force fields. inclusion of a geometry-dependent charge calculation. *J. Chem. Soc., Faraday Trans.*, 90(19):2881, 1994. doi: 10.1039/ft9949002881.

[114] L. Vočadlo, K. S. Knight, G. D. Price, and I. G. Wood. Thermal expansion and crystal structure of FeSi between 4 and 1173 k determined by time-of-flight neutron powder diffraction. *Phys. Chem. Miner.*, 29(2):132–139, 2002. doi: 10.1007/s002690100202.

[115] E. G. Moroni, W. Wolf, J. Hafner, and R. Podloucky. Cohesive, structural, and electronic properties of fe-si compounds. *Phys. Rev. B*, 59(20):12860–12871, 1999. doi: 10.1103/physrevb.59.12860.

[116] Michael C. Pitman and Adri C. T. van Duin. Dynamics of confined reactive water in smectite clay–zeolite composites. *J. Am. Chem. Soc.*, 134(6):3042–3053, 2012. doi: 10.1021/ja208894m.

[117] L. Levien, C. T. Prewitt, and D. Weidner. Structure and elastic properties of quartz at pressure. *Am. Mineral.*, 65:920–930, 1980.

[118] T. T. Järvi, A. Kuronen, M. Hakala, K. Nordlund, A. C. T. van Duin, W. A. Goddard, and T. Jacob. Development of a ReaxFF description for gold. *Eur. Phys. J. B*, 66(1):75–79, 2008. doi: 10.1140/epjb/e2008-00378-3.

[119] B. W. H. van Beest, G. J. Kramer, and R. A. van Santen. Force fields for silicas and aluminophosphates based onab initiocalculations. *Phys. Rev. Lett.*, 64(16):1955–1958, 1990. doi: 10.1103/physrevlett.64.1955.

[120] J. E. Mueller, A. C. T. van Duin, and W. A. Goddard. Development and validation of ReaxFF reactive force field for hydrocarbon chemistry catalyzed by nickel. *J. Phys. Chem. C*, 114 (11):4939–4949, 2010. doi: 10.1021/jp9035056.

[121] V. Swamy, S. K. Saxena, B. Sundman, and J. Zhang. A thermodynamic assessment of silica phase diagram. *J. Geophys. Res.: Solid Earth*, 99(B6):11787–11794, 1994. doi: 10.1029/93jb02968.

[122] E. P. Meagher, J. A. Tossell, and G. V. Gibbs. A CNDO/2 molecular orbital study of the silica polymorphs quartz, cristobalite, and coesite. *Phys. Chem. Miner.*, 4(1):11–21, 1979. doi: 10.1007/bf00308356.

[123] N. R. Keskar and J. R. Chelikowsky. Structural properties of nine silica polymorphs. *Phys. Rev. B*, 46:1–13, 1992. doi: 10.1103/PhysRevB.46.1.

[124] G. V. Gibbs, , C. T. Prewitt, and K. J. Baldwin. A study of the structural chemistry of coesite. *Z. Krist.*, 145(B6):108–123, 1977.